OKINAWA INSTITUTE OF SCIENCE AND TECHNOLOGY
GRADUATE UNIVERSITY

Thesis submitted for the degree

Doctor of Philosophy

Development of an SPH variant of implicit LES for studying wave energy transport

by

Kalale Chola

Supervisor: **T. Shintake**
Co-Supervisor: **S. Mitarai**

May, 2018

Declaration of Original and Sole Authorship

I, Kalale Chola, declare that this thesis entitled *Development of an SPH variant of implicit LES for studying wave energy transport* and the data presented in it are original and my own work.

I confirm that:

- No part of this work has previously been submitted for a degree at this or any other university.
- References to the work of others have been clearly acknowledged. Quotations from the work of others have been clearly indicated, and attributed to them.
- In cases where others have contributed to part of this work, such contribution has been clearly acknowledged and distinguished from my own work.

Date: May, 2018
Signature:

Abstract

Development of an SPH variant of implicit LES for studying wave energy transport

The smoothed particle hydrodynamics (SPH) method is an efficient numerical technique for simulating complex problems such as free flows. Since such flows are characterized by high Reynolds number, turbulence modeling is a necessity. In the literature, some models from Eulerian based numerical schemes have been adopted but comprehensive analyses of their effectiveness have not been provided.

In this thesis, a version of SPH that implicitly models turbulence has been developed. First, using a convolution filter, a filtering integral transform (FIT) is proposed and applied to the underlying, disordered field $\{\rho, p, \rho\mathbf{u}\}$ to construct a smooth field $\{\langle\rho_h\rangle, \langle p_h\rangle, \langle\rho_h\rangle\widetilde{\mathbf{u}}_h\}$. Using the FIT, filtered equations consistent with explicit Large Eddy Simulation (LES) are derived. Second, using a deconvolution filter, a de-filtering integral transform (DIT) is proposed as an inverse transform to the FIT. By applying the DIT to the filtered equations a high order version of SPH, to be called SPH-i is formulated. In SPH-i, unlike SPH, the disordered field is evolved dynamically. Third, unlike standard SPH two inverse filters are required; a convolution filter and a deconvolution filter. A rigorous method for constructing these filters in 2D is presented. Fourth, to address the problem of numerical oscillations in the pressure field, common in standard SPH, has been addressed by introducing a differential equation for the pressure field that includes smoothing terms.

The proposed SPH-i model was applied to a number of free surface flow problems and the results are promising.

Acknowledgment

First and foremost I would like to thank my supervisor, Professor Tsumoru Shintake for giving me the opportunity to pursue this research under his guidance. I learned a lot from his wide knowledge of science and his integral view on research, consequently leaving a long lasting impression on me.

I would also like to express my sincere gratitude to the other members of my thesis committee members including Professor Nic Shannon and Professor Satoshi Mitarai for their support and constructive comments throughout the course of my dissertation work.

I owe my sincere gratitude to Dr. Mathieu Taillefumier for his invaluable support towards the numerical implementation of the numerical solver. Having initially developed the code in Fortran, he helped me translate the code into C to parallelize it.

Many thanks to my wife and our two wonderful daughters Rosemary and Grace for their patience, love and support. Words alone cannot describe the unconditional love, support and encouragement from my parents who have been instrumental in guiding me throughout my life.

Abbreviations

ADM	approximate deconvolution method
CFD	computational fluid dynamics
CFL	Cuorant-Friedrichs-Lewy condition
CNSE	compressible Navier-Stokes equations
DIT	de-filtering integral transform
DNS	direct numerical simulation
FDE	finite difference equation
GPU	graphical processing unit
FIT	filtering integral transform
INSE	incompressible Navier-Stokes Equations
ISPH	incompressible smoothed particle hydrodynamics
LANS$-\alpha$	Lagrangian averaged Navier-Stokes equations
LES	large eddy simulation
MPS	moving particle semi-implicit
PDE	partial differential equation
PDF	probability density function
PPE	pressure Poisson equation
SGS	sub-grid stress tensor
SPS	sub-particle stress
SPH	smoothed particle hydrodynamics
TDR	turbulent dissipation rate
TKE	turbulent kinetic energy
WCSPH	weakly compressible smoothed particle hydrodynamics
WEC	wave energy converter

Glossary

FIT	A set of filtering rules for regularizing the "disordered" flow field by convolution to obtain a smooth field.
DIT	A set of de-filtering rules for de-regularizing the smooth flow field by deconvolution to recover the "disordered" field.
Turbulence dissipation rate	is the rate at which turbulent kinetic energy is transformed into thermal internal energy of a system.
Thermal diffusivity	is a measure of the rate at which heat is transfered from the hot to the cold side of an object.

Nomenclature

General Rules

- Only the symbols frequently used in the thesis are listed
- The meaning of each symbol is given when introduced
- Sometimes the same symbol is used to mean different things. In such cases the physical meaning of the symbol is apparent.
- Vectors are represented using boldface
- Rank-2 tensors are represented by block letters with two lines below or above the symbol
- Symbols between angle brackets (e.g. $\langle \rho_h \rangle$) indicate local approximation/average of the field ρ by filtering with a convolution filter whose cut-off length is h

Symbols

c	Speed of sound
$\boldsymbol{g}$	Acceleration due to gravity
k	Thermal conductivity
α	Thermal diffusivity
ν	Kinematic viscosity
μ	Dynamic viscosity

β	Volumetric thermal expansivity
κ_s	Adiabatic compressibility
K_S	Adiabatic incompressibility modulus
K_T	Isothermal incompressibility modulus
C_V	Isochoric heat capacity
C_P	Isobaric heat capacity
γ	Adiabatic index
$\mathbf{r}$	Position vector
$\mathbf{u}$	Velocity field
U	Internal energy
u	Internal energy density
E	Total energy of the system
p, P	Thermodynamic pressure
T	Absolute temperature
ρ	Mass density or simply density
h	Smoothing length
w_h, w	Convolution filter
φ_h, φ	Deconvolution filter
$\mathcal{N}(i)$	Set of nearest neighbors to particle i
Δt	Time step
$\Delta\mathbf{r}$	initial particle spacing
Re	Reynolds number ($= UL/\nu$)
Ma	Mach number (U/c)
$\underline{\underline{\tau}}$	Stress tensor
$\underline{\underline{\sigma}}$	Deviatoric or viscous tensor
$\underline{\underline{\Omega}}$	Rotation rate or vorticity tensor
$\underline{\underline{S}}$	Strain rate tensor
$\mathcal{P}$	Thermo-mechanical power
$\boldsymbol{\omega}$	Vorticity vector
$\langle f, g \rangle$	Inner product
$\langle f_h \rangle$	Local average by convolution filter w_h
$\lvert f \rangle$	Ket (column) vector in Dirac notation
$\langle f \rvert$	Bra (row) vector
$d^\nu \mathbf{r}$	Lebesgue measure e.g in 2D, $d^2\mathbf{r} = dxdy$
$\widetilde{\varepsilon}_h \overset{\mathrm{D}}{\sim}$ $\mathrm{m^2 s^{-3}}$	locally averaged turbulent dissipation rate
$\widetilde{k}_h \overset{\mathrm{D}}{\sim}$ $\mathrm{m^2 s^{-2}}$	locally averaged turbulent kinetic energy

Contents

List of Figures

List of Tables

Chapter 1

Introduction

Free-surface flows have industrial importance in hydraulic engineering. Some examples of free-surface flows include wave breaking in shallow water, sloshing in tanks, dam-break problems and wave impact on structures. These phenomena are highly complex such that formulating analytical models is an enormous task. Nevertheless, in special cases where there is no free-surface deformation explicit solutions do exist. The earliest such solution was described by Franz Josef Gestner in 1802 [2]. The Airy or Stokes wave theory gives a linearized description of the propagation of water waves [3]. Linear wave theory is, however, restricted to small amplitude waves with non breaking free-surfaces and can thus not be used to analyze breaking waves. The nonlinear nature of breaking waves demands for numerical solutions that may be obtained either through grid based methods or mesh-free methods. The demand for the design of computer simulators (based on these methods) that are capable of accurately capturing violent flows such as wave breaking is still very high [4]. Lately this field of research has witnessed marked growth due to the introduction of robust computational tools such as Graphical Processing Unit, GPU that significantly speed up computational power. With these notable developments, coupled with the ever increasing demand for realistic simulations of the evolution of ocean waves, turbulence, ocean currents, tides, tsunamis etc., the fluid dynamics fraternity has been motivated to work on the design of specialized techniques to simulate ocean wave dynamics for energy extraction purposes. It is worth mentioning that although there has been a marked growth in Computational Fluid Dynamics, CFD, simulation of free-surface flows with breaking surfaces remains a very challenging problem for fluid mechanics [5]. Therefore simulation of breaking waves will be one of the core elements of my proposed thesis work.

In modeling free-surface flow problems with large deformation, SPH is a natural choice because fluid particles can move freely ultimately overcoming the challenges encountered when using a mesh. Free-surfaces and multi-phase can also be conveniently handled. To model incompressible free-surface flows, a pseudo-incompressible constraint is imposed by way of the Mach number such that a fluid is weakly compressible. This standard approach is called weakly compressible SPH [6]. Compared to well established mesh based methods including finite element method, finite volume method and finite difference method, SPH is a relatively new CFD method. In particular a number of challenges still remain open. Some of these difficulties include pressure oscillations, enforcing complex solid boundary conditions, stability and accuracy.

The problem of pressure oscillations has been addressed in a number of ways including

the use of well-tuned artificial viscosity [7]. Liu et.al. [8], [9] proposed a higher order model called finite particle method that has been reported to give smooth pressure fields due to the improved density estimate. Another approach involves the re-initialization of the density field applied every 20-40 time steps. Since density and pressure are related through an equation of state, minimizing the accumulation of errors in the density fields results in a pressure field that is smooth. This approach uses either a Shepherd filter or more generally the moving least square method [10],[11].

This thesis first aims at proposing a version of smoothed particle hydrodynamics (SPH) that is consistent with explicit large eddy simulation (LES) to address the problem of turbulence modeling. We further note that SPH is a zeroth order deconvolution method. A new method to be called SPH-i as an nth order deconvolution method that is consistent with implicit LES is proposed. The main attraction of SPH-i is that unlike SPH, no turbulence modeling is required.

1.1 Background and Motivation

Sampling problem consider a discrete fluid shown in figure 1.1 as approximating a continuous fluid in the continuum limit. Assume that the density of all support particles • are given as

$$\text{support particle } \bullet \qquad \{\rho(\mathbf{r}_j) |\ j = 1, 2, 3, ..., N.\} \tag{1.1}$$

Using this information, compute the density of the target particle • whose support is defined as

$$\text{target particle } \bullet \qquad \Omega_h(\mathbf{r}) := \{\mathbf{r}, \mathbf{r}_j \in \mathbb{R}^n |\ ||\mathbf{r} - \mathbf{r}_j \leq 2h||\} \quad \rho(\mathbf{r}) = ? \tag{1.2}$$

Since this is a very difficult problem, it will be split into three separate problems each with its own chapter; chapters 3, 4 and 5 will address this problem in greater detail. The solution to this problem forms the basis upon which a new version of smoothed particle hydrodynamics, SPH will be formulated.

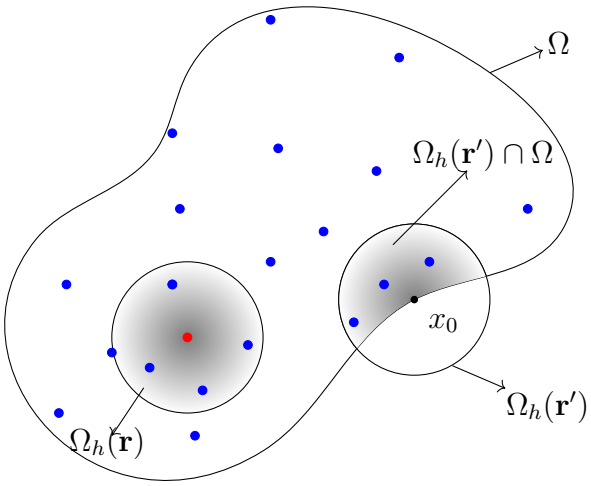

Figure 1.1: Sampling problem: given the density $\rho(\mathbf{r}')$ of all support particles •, find the density of the target particle • whose density is unknown.

Pressure oscillations in SPH The second problem addressed in this work is the one attributed to high frequency noise in the pressure field in SPH. A solution to this problem, adopted from Riemann solvers, has been proposed as $\delta-$SPH [7]. In this approach, "artificial" diffusion terms are added to the continuity equation to smooth out fluctuations in the density field. Since standard SPH uses an equation of state $p(\rho) = c^2(\rho - \rho_0)$, a smooth density field implies a smooth pressure field. The introduction of diffusion terms in the continuity equation, however, may introduce unphysical changes to the flow.

As an alternative, an equation for pressure, admissible for liquids and gases, is proposed in this work. The advantage of this approach is that pressure smoothing terms of the form $\nabla^2 p, \nabla^2 \rho$ naturally appear in the equation for pressure as a consequence of mass and energy conservation.

1.2 Thesis structure

The thesis is organized as follows. First, the problem of oscillations in the pressure field in SPH is addressed. From thermodynamic principles, an equation for pressure that intrinsically contains smoothing terms is derived. This equation will be used in preference to the simpler equation of state for pressure that is commonly used in standard SPH.

In chapter 2 the second and central component of this work, the filtering and de-filtering rules are introduced. A proper choice of the filtering and de-filtering rules is proposed. From these rules, convolution and deconvolution operators are derived. Using these operators, a compatible pair of convolution and deconvolution filters is constructed. By applying the proposed filtering rules to the pressure equation, mass, and momentum conservation laws, a version of SPH consistent with the filtered equations of large eddy simulation, LES is derived in chapter 4. Application of the de-filtering rules to the filtered equation leads to a

version of SPH to be called SPH-i (the i mean turbulent phenomena is implicitly captured, no turbulence modeling is required) and is presented in chapter 5.

The third component of this thesis includes a discussion on a linear boundary force model (chapter 6) and the thermo-mechanical power delivered to a fluid body (chapter 7). In chapter 8 the proposed SPH-i model is applied to a number of benchmark free surface flow problems for validation. These include; (i) hydrostatic equilibrium (ii) dam break (iii) dam break with wet bed (iv) periodic waves on a plane slope

The main conclusions are drawn in the final chapter and propositions for future work are made.

Chapter 2

Proposed Equation for Pressure

The first part of this research work is devoted to tackle the problem of spurious numerical noise on the pressure field that drastically affects weakly compressible SPH (WCSPH) models. Several procedures for handling this problem have been proposed in the literature. In [7] the authors suggested to re-initialize the density field every 20-40 time steps with a moving least square (MLS) integral interpolation. While this procedure was reported to generally give good results, long term stability of the pressure field is not guaranteed. The reason for this is that the total volume of the fluid body is no longer conserved as the hydrostatic component has been improperly filtered [12]. Since density and pressure are related through a simple equation of state in WCSPH, density re-initialization ensures that the pressure field remains relatively smooth. The third and particularly interesting approach is to introduce artificial diffusion terms in the continuity equation as proposed in [13]. As this approach introduces diffusion terms in an artificial way, another approach with physically sound basis is proposed in this chapter.

2.1 Background

The main task in fluid dynamics is to find the velocity field describing the flow in a given domain. To do this, one uses the fundamental equations of fluid flow, which include the familiar laws of mechanics: mass conservation and momentum conservation. If the flow leads to compression of the fluid, we must also consider thermodynamics by including energy conservation. This set of equations will be collectively referred to as the compressible Navier-Stokes equations, CNSEs.

To derive the incompressible Navier-Stokes (INS) equations, we assume that fluid compressibility is zero. In this case, pressure disturbances are transmitted instantaneously. The thermodynamic state becomes fixed, thereby decoupling the mass and momentum equations from the energy equation. While the INS represents a great simplification of the CNSE, numerical solution of the INS still remains challenging. The instantaneous propagation of pressure fluctuations results in an elliptic-type system that requires an implicit formulation and nonlocal communication [14]. In INS the pressure is obtained by solving a system matrix equation (describing the pressure Poisson equation, PPE) on an entire computational domain; small perturbations in boundary or free surface areas can instantaneously propagate across the entire domain and can lead to big oscillations and instabilities in the numerical solution.

This means that the numerical solution of the INS is sensitive to numerical oscillations and easier to induce numerical instabilities [6].

Since elliptic systems cannot be solved explicitly, the problem of solving the PPE can be avoided by relaxing the incompressibility constraint. This is achieved by using empirical evidence that fluids in general have low compressibility meaning that fluids are weakly compressible. Weakly compressible smoothed particle hydrodynamics (WCSPH) accomplishes this by introducing an equation of state for pressure based on a further assumption that the flow is barotropic, i.e pressure is a function of density only [15, 16]. By supplying this equation of state for the CNSE, the mass and momentum equations are effectively decoupled from the energy equation.

In the simulation of problems with highly irregular geometries and highly nonlinear flows, SPH is slowly becoming a method of choice. However, the WCSPH has a number of reported drawbacks. In order to keep density fluctuations low, a large sound speed has to be used leading to a strict constraint on the time step due to the Courant-Friedrichs-Lewy (CFL) stability condition. Second, artificial compressibility can also cause problems with sound wave reflection at domain boundaries. Owing to these problems Incompressible smoothed particle hydrodynamics (ISPH) has been proposed [17]. Since ISPH employs a zero compressibility constraint, the CFL condition depends on fluid speed rather than sound speed. Furthermore, some authors claim that the pressure field in the ISPH has smaller oscillations compared to WCSPH. However, these results remain inconclusive and controversial, [18][Chapter 6].

The theory development in this section proceeds by first examining the continuous flow assumption. Based on this assumption we then study the thermodynamics of fluid particles on locally compact spaces. Thermodynamic principles are then used to derive an explicit evolution equation for pressure to accommodate liquids and gases with very few assumptions.

2.2 Motivation

The method of smoothed particle hydrodynamics, SPH is well known to be affected by high frequency numerical noise on the pressure field when applied to liquids. This may be problematic in applications where smooth pressure fields are essential such as coupled SPH/structural solvers. To mitigate this problem, Molten and Colagrossi [13] introduced a version of SPH called $\delta-$SPH. Their procedure is based on the introduction of a density diffusion term $\delta hc\nabla^2\rho$ in the continuity equation; h is the filter width, c is the speed of sound and the tunable parameter $\delta \in [0, 1]$. This term must vanish in the continuum limit where $h \to 0$. Just like the artificial viscosity term used in standard SPH to smooth out discontinuities, the diffusion term is a purely numerical effect and can thus be referred to as "artificial diffusion ". It is, however, possible that the artificial diffusion term may introduce unphysical changes of the flow [13], [12]. Recently Sun et.al. [19] have proposed further improvements to enhance the $\delta-$SPH model.

The goal of this section is to address the problem of high frequency noise in the pressure field from an alternative but physical perspective.

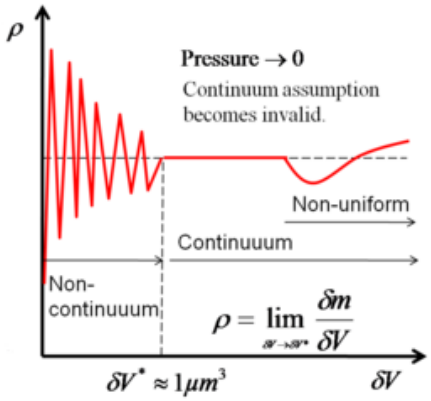

Figure 2.1: Continuum hypothesis

2.2.1 Continuum hypothesis

Figure 2.1 depicts the continuum hypothesis. By the postulates of the continuum hypothesis fluids comprise of fluid particles. Each fluid particle consists of molecules which are in thermal equilibrium. At any point in space and time, each fluid particle will consist of different molecules but the total number of molecules remains constant at certain length scales. If the volume of a fluid particle is δV, mass δm and density ρ, there exists a lower limit on the volume of the particle such that

$$\lim_{\delta V \to \delta V^*} \frac{\delta m}{\delta V} = \rho \tag{2.1}$$

The acceptable lower limit for gases and liquids is $\delta V^* = 1\mu m^3$. The volume of a fluid particle has to meet this criteria. Below this value i.e the microscopic scale, due to molecular fluctuations, fluid density and all other fluid variables are not smooth, they are violently non-uniform. Here, hydrodynamic differential equations cannot be written down under the usual rules of calculus. One essential mathematical ingredient is distribution theory which is useful in the theoretical development of the conservations laws for molecular dynamics systems. Note, however, that at the mesoscopic and macro scales, the fluid medium is accepted as a continuum.

The continuum consists an infinite number of fluid particles. Lagrangian particle methods approximate the continuum with a finite number of particles.

2.3 Lagrangian description of fluid flow

Our objective is to mathematically describe the motion of a fluid parcel during a given time interval. This kind of description is essentially based on studying the trajectory of each parcel in the fluid domain. This is called Lagrangian description of fluid flow. Fluid motion can then be associated to the geometrical transformation from the configuration this fluid domain presents at a reference time instant into the configuration it presents at a later time. This way we can naturally obtain the time history of the evolution of each parcel in the fluid domain.

2.3.1 Useful terms for flow description

Definition 2.3.1 (time duration of the computation)**.** *Let $\mathcal{I}$ be an open time duration over which we would like to study the dynamics of the hydrodynamic system. Then the time duration with $N+1$ time steps is defined as the union*

$$\mathcal{I} = \bigcup_{n=0}^{N} [t_n, t_{n+1}] \tag{2.2}$$

where the step size is given as $(\Delta t)_n = t_{n+1} - t_n$.

Definition 2.3.2 (fluid particle)**.** *Let $\Omega \subseteq \mathbb{R}^n$ be a fluid domain. We define a fluid parcel $\mathcal{W} \subset \Omega$ as the volume moving with the fluid within Ω.*

Definition 2.3.3 (reference configuration & time instant)**.** *The reference configuration is a fluid domain Ω_0 fixed at the reference time $t_0 \in \mathcal{I} \subseteq \mathbb{R}^+$*

Definition 2.3.4 (fluid motion & flow map)**.** *The fluid motion is the family $\{\varphi_t\}_{t\in\mathcal{I}}$ of continuous maps $\varphi_t : \overline{\Omega}_0 \to \mathbb{R}^n$ i.e. $\mathbf{r} \mapsto \varphi(\mathbf{r}, t)$ whose map φ_t, for all $t \in \mathcal{I}$, advances each fluid particle from its position $\mathbf{r}_0 \in \Omega_0$ in the reference configuration to its position at time t. The flow map can then be defined precisely as the function $\varphi : \overline{\Omega}_0 \times \mathcal{I} \to \mathbb{R}^n$ such that $\varphi(\mathbf{r}_0, t) = \varphi_t(\mathbf{r}_0)$. Notice that $\varphi(\mathbf{r}_0, t_0) = \varphi_{t_0}(\mathbf{r}_0) \equiv \mathbf{r}_0$. [1]. If $\mathcal{W}$ is a fluid parcel in Ω, then $\varphi_t(\mathcal{W}) = \mathcal{W}_t$ is the volume $\mathcal{W}$ moving with the fluid, see figure (2.2)*

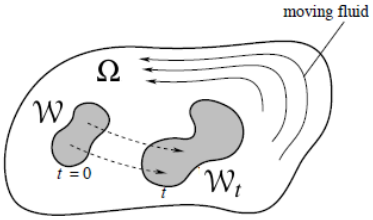

Figure 2.2: $\mathcal{W}_t$ is the image of $\mathcal{W}$ as fluid particles in $\mathcal{W}$ flow for time t. As the sub-domain $\mathcal{W}$ is carried by the fluid flow, it deforms to $\mathcal{W}_t$ at time t in the domain Ω.

After mathematically modeling the notion of " fluid motion" as a family of maps, we need to study the properties these maps are supposed to possess (besides continuity).

a) **Property one.** The intuitive idea that two different bodies cannot simultaneously occupy the same portion of space can be expressed as a property for our definition of fluid motion: " for each $t \in \mathcal{I}$, $\varphi_t|_{\Omega_0}$ is *smooth and has a smooth inverse on* $\Omega_t := \varphi_t(\Omega_0)$".

b) **Property two.** Another intuitive property guarantees the continuity of $\varphi(\mathbf{r}_0, t) : \mathcal{I} \to \mathbb{R}^n$, for each $\mathbf{r}_0 \in \Omega_0$. This means that *"no particle can disappear and reappear at another position"* i.e. the trajectory of a particle is (at least) continuous.

[1] The subscript $_t$ should not be confused with a time derivative !

This description of fluid motion using the flow map and the fluid particles' trajectories with respect to the reference configuration is the so called Lagrangian description and the points in Ω_0 are known as material coordinates.

Once we know the particle's trajectories we would like to measure how fluid quantities change along a particle's trajectory i.e. we want to compute derivatives along particle trajectories. Consider a smooth function $f : \Omega \times \mathcal{I} \to \mathbb{R}$ and the particle trajectory $\mathbf{r} : \mathcal{I} \to \mathbb{R}^n$. The time derivative of f along the trajectory $\mathbf{r}(t)$ at time t is obtained via the chain rule

$$\begin{aligned} \frac{d}{dt} f(\mathbf{r}(t), t) &= \frac{\partial}{\partial t} f(\mathbf{r}(t), t) + \frac{d\mathbf{r}(\mathbf{t})}{dt} \cdot \frac{\partial}{\partial \mathbf{r}} f(\mathbf{r}(t), t) \\ \frac{d}{dt} f(\mathbf{r}(t), t) &= \left(\frac{\partial}{\partial t} + \mathbf{u} \cdot \nabla \right) f(\mathbf{r}(t), t) \end{aligned} \tag{2.3}$$

Definition 2.3.5 (material or Lagrangian derivative)**.** *The material derivative operator is defined as* $\frac{d}{dt} := \frac{\partial}{\partial t} + \mathbf{u} \cdot \nabla$. *Then the derivative of* ρ *along a particle's trajectory* $\mathbf{r}(t)$ *is given by* $\frac{d}{dt}\rho(\mathbf{r}(t))$

2.3.2 Concept of continuous flow

For a fluid flow to be continuous, we require that the velocity $\mathbf{u}(\mathbf{r}(t), t) \equiv \mathbf{u}(\mathbf{r})$ be finite and a continuous function of $\mathbf{r}(t)$ i.e. $\nabla \cdot \mathbf{u}(\mathbf{r}(t))$ and $\partial_t \mathbf{u}(\mathbf{r}(t))$ are finite but not necessarily continuous.

Since $\nabla \cdot \mathbf{u}(\mathbf{r}(t))$ and $\partial_t \mathbf{u}(\mathbf{r}(t))$ are finite, there is no infinite acceleration, which is physically consistent.

2.3.3 Consequences of continuous flow

[1] A material volume remains material. No segment of fluid can be joined or broken apart.

[2] Material surface remains material. The interface between two materials always exists.

[3] Material line remains material. The interface of two material surfaces always exists.

[4] Material neighbors remain neighbors. A mathematical proof of this is given below. We must prove that given two particles, the distance between them at time t is small, and the distance between them at time $t + \delta t$ is still small.

Proof. Consider two particles with initial position $\mathbf{r}(t)$ and $\mathbf{r}(t) + \delta\mathbf{r}(t)$, initial time t and the fluid velocity $\mathbf{u}(\mathbf{r}(t))$.

$$\begin{aligned} \delta\mathbf{r}(t + \delta t) &= [\mathbf{r}(t) + \delta\mathbf{r}(t)] + \mathbf{u}(\mathbf{r}(t) + \delta\mathbf{r}(t))\delta t - [\mathbf{r}(t) + \mathbf{u}(\mathbf{r}(t)\delta t)] \\ &= \delta\mathbf{r}(t) + [\mathbf{u}(\mathbf{r}(t) + \delta\mathbf{r}(t)) - \mathbf{u}(\mathbf{r}(t)]\delta t \\ &= \delta\mathbf{r}(t) + \nabla\mathbf{u}(\mathbf{r}(t)) \cdot \delta\mathbf{r}(t)\delta t \\ \implies \delta\mathbf{r}(t + \delta t) &= \left[\underline{1} + \nabla\mathbf{u}(\mathbf{r}(t))\delta t\right] \cdot \delta\mathbf{r}(t) \end{aligned}$$

Therefore $\delta\mathbf{r}(t + \delta t) \propto \delta\mathbf{r}(t)$ as $\nabla\mathbf{u} < \infty$ due to the continuous flow assumption. Thus, if $\delta\mathbf{r}(t) \to 0$ then $\delta\mathbf{r}(t + \delta t) \to 0$. This means that two particles can never

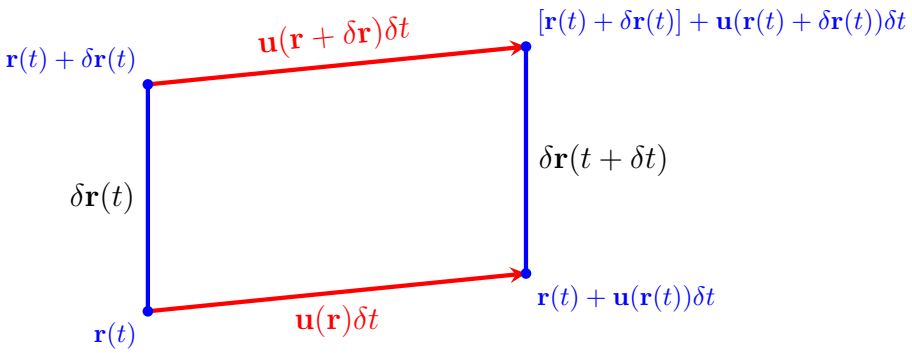

Figure 2.3: Material neighbors remain neighbors provided that the flow is continuous.

be an infinite distance apart . Thus the flow is continuous and two particles that are neighbors will remain neighbors. □

Definition 2.3.6 (fluid domain)**.** *Let $\Omega \subseteq \mathbb{R}^n$ be an open set bounded by a smooth surface $\partial\Omega$. If Ω is supposed to be "filled with a fluid" such that the mass-density*

$$\rho(\mathbf{r}) > 0, \qquad {}^{\forall}\mathbf{r} \in \Omega \tag{2.4}$$

then we call Ω a fluid domain.

Definition 2.3.7 (real-valued function)**.** *A scalar-valued function of multi-variables is defined as $f(\mathbf{r}) : \Omega \subset \mathbb{R}^n \to \mathbb{R}$. The domain of the scalar valued function f is Ω. The range of f is contained in $\mathbb{R}$, i.e. real space. Furthermore, as a set, the graph of the scalar valued function is given as*

$$\text{graph } f = \{(\mathbf{r}, f(\mathbf{r})) \in \mathbb{R}^{n+1} | \mathbf{r} \in \Omega\} \tag{2.5}$$

Definition 2.3.8 (smoothness and compactness)**.** *A real-valued function is said to be* smooth *if it is* infinitely differentiable*. Let w be a smooth and compact function over the test space. We then write $w \in C_c^{\infty}(\Omega(\mathbf{r}))$.*

Definition 2.3.9 (Test or target particle)**.** *This is a material element whose physical attributes are to be measured or probed.*

Definition 2.3.10 (Test space)**.** *Let $\Omega \subset \mathbb{R}^n$ be a given body. For a test element located at $\mathbf{r}$, we denote its test space as $\Omega_h(\mathbf{r})$ bounded by a test surface $\partial\Omega(\mathbf{r})$. The test space is thus the domain of influence of the test element.*

$$\Omega_h(\mathbf{r}) = \left\{\mathbf{r}, \mathbf{r}' \in \mathbb{R}^n \middle| \, ||\mathbf{r} - \mathbf{r}'|| \leq \kappa h, \; w_h(\mathbf{r} - \mathbf{r}') \geq 0, \; \kappa \in \mathbb{R}^+\right\} \tag{2.6}$$

2.4 Pressure Equation

The underlying principle is that incompressible flows can be simulated by using methods that add a finite but small amount of compressibility. The motivation behind this is that any fluid has a finite incompressibility/bulk modulus. Therefore, these methods are often called

pseudo-incompressible or artificially compressible methods. With highly parallel computation, explicit algorithms can exploit these resources.

In this work a new form of pseudo-incompressibility is derived from thermodynamical principles. Artificial compressibility, as noted by Chorin [15] rely on an artificial equation of state. It can be shown that this artificial equation of state is equivalent to imposing an additional constraint to the original compressible Navier-Stokes, CNSE system. This additional constraint is necessary to eliminate the energy equation from the CNSE reducing the number of equations and unknowns [20].

To study the fluid dynamics we solve the Navier-Stokes equations

(1) mass conservation

$$\frac{d\rho}{dt} = -\rho \nabla \cdot \mathbf{u} \tag{2.7}$$

(2) momentum conservation

$$\rho \frac{d\mathbf{u}}{dt} = -\nabla p + \nabla \cdot \underline{\underline{\sigma}} + \rho \mathbf{b} = 0 \tag{2.8}$$

(3) energy conservation

$$\frac{1}{V}\frac{dU}{dt} = -P \nabla \cdot \mathbf{u} + \nabla \cdot (k \nabla T) + \Phi \tag{2.9}$$

where $\mathbf{u}$ is the fluid velocity, ρ is fluid mass-density, $V = m/\rho$ is the volume of a material element, P is the pressure, $\underline{\underline{\sigma}}$ is viscous stress tensor, $\Phi = \underline{\underline{\sigma}} : \nabla \mathbf{u}$ is the viscous dissipation, k is the thermal conductivity and $\mu = \nu\rho$ is the dynamic viscosity.

$$\underline{\underline{\sigma}} = \mu \left(\nabla \mathbf{u} + \nabla \mathbf{u}^{\mathrm{T}} \right) - \frac{2}{3} \mu (\nabla \cdot \mathbf{u}) \underline{\underline{1}} \tag{2.10}$$

These PDEs are valid over a continuum where the fluid variables are assumed to be smooth and continuous. The motion of a compressible fluid is directly affected by its thermodynamic state which is itself a consequence of the motion. Any change in the state of the fluid is independent of the actual physical process by which the change is achieved. Consider the motion of a fluid particle moving along its trajectory as shown in figure 2.4. We define a state space $\sum$ as an open, simply connected subset $\sum \subset (0, \infty) \times (0, \infty)$. The elements of $\sum$ are called states which are pressure P, internal energy U and volume V. We define a path Γ for our model to be an oriented, continuous, piecewise C^1 curve in the state space. This is then parameterized by writing

$$\Gamma = \left\{ \left(T(\mathbf{r}(\mathbf{t}), \mathbf{t}), V(\mathbf{r}(\mathbf{t}), \mathbf{t}) \right) \Big| t \in \mathfrak{I}, \mathbf{r} \in \Omega_h \subset \Omega \subset \mathbb{R}^n \right\} \tag{2.11}$$

The first law of thermodynamics for this fluid element is given by

$$\delta Q = dU + \delta W \tag{2.12}$$

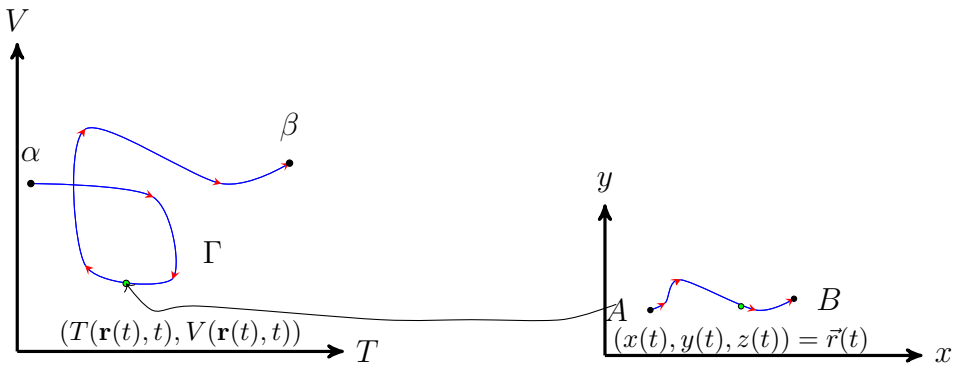

(a) State space $\sum$ **(b)** Test space $\Omega_h(\mathbf{r})$.

Figure 2.4: Physical space and state space associated with a fluid particle evolving within its test space. The start and end times of the fluid particle along its trajectory are $t = a$ and $t = b$ respectively.

where δQ is the heating 1-form from which we obtain the net heat gained by the fluid element along Γ as $\mathbb{Q}(\Gamma) = \int_\Gamma \delta Q$. Similarly, for the working 1-form δW, the work done by the fluid element along Γ is defined as $\mathbb{W}(\Gamma) = \int_\Gamma \delta W = \int_V P dV$. The first law (2.12) is only useful if we can determine a functional relationship between the fluid element's internal energy, volume and pressure $P = P(U, V)$. Assuming an equation of state or alternatively an evolution equation for pressure can be found, the first law becomes

$$\delta Q = dU + P(U, V)dV \tag{2.13}$$

According to Pfaff's theorem (2.13) has an integrating factor $1/T(U, V)$ (postulated in the zeroth law of thermodynamics) that transforms it into an an exact differential form

$$\frac{\delta Q}{T(U, V)} = \frac{1}{T(U, V)} dU + \frac{P(U, V)}{T(U, V)} dV = dS(U, V) \tag{2.14}$$

which implies existence of two new state functions which are the temperature $T(U, V)$ and an associated integral called the entropy $S(U, V)$. The final result is Gibb's equation

$$dU = TdS - PdV \tag{2.15}$$

Since our idea is to decouple the energy equation (2.9) from the continuity (2.7) and momentum (2.8) equations, we need to determine $dP(U, V)$. Starting with the differential form for U

$$dU = \left(\frac{\partial U}{\partial S}\right)_V dS + \left(\frac{\partial U}{\partial V}\right)_S dV \tag{2.16}$$

From (2.15) and (2.16) we have

$$T = \left(\frac{\partial U}{\partial S}\right)_V, \qquad P = -\left(\frac{\partial U}{\partial V}\right)_S \tag{2.17}$$

However, dU is an exact differential and second derivatives of partials are the same no matter the order of differentiation. We then obtain an important relation for the system parameters.

$$\left(\frac{\partial T}{\partial V}\right)_S = -\left(\frac{\partial P}{\partial S}\right)_V \tag{2.18}$$

which is one of Maxwell's relations. Since we have $U = U(S, V)$, we then infer that $T = (S, V)$ and $P = P(S, V)$. Using these important relationships we proceed to compute the differential forms for the pressure.

$$dP = \left(\frac{\partial P}{\partial S}\right)_V dS + \left(\frac{\partial P}{\partial V}\right)_S dV \tag{2.19}$$

In order to obtain the material derivative of pressure, we first use Gibb's equation (2.15) to eliminate dS from (2.19). This direct substitution yields

$$dP = \frac{1}{T}\left(\frac{\partial P}{\partial S}\right)_V dU + \left\{\left(\frac{\partial P}{\partial V}\right)_S + \frac{P}{T}\left(\frac{\partial P}{\partial S}\right)_V\right\} dV \tag{2.20}$$

Here we now introduce thermodynamic capacities given by the following relations.

$$K_S = -V\left(\frac{\partial P}{\partial V}\right)_S,\ K_T = -V\left(\frac{\partial P}{\partial V}\right)_T,\ \beta = \frac{1}{V}\left(\frac{\partial V}{\partial T}\right)_P \tag{2.21}$$

where K_S is the adiabatic incompressibility modulus, K_T is the isothermal incompressibility modulus and β is the volumetric thermal expansivity. Since $K_{S,T} < 0$ contradicts mechanical stability, all materials have $K_{S,T} > 0$. There is no general principle that could limit β. However, fluids and most materials expand upon heating so that $\beta > 0$. To determine the coefficient of dU in (2.20), we first determine the isochoric change in pressure with temperature. Using the Jacobian transform

$$\begin{aligned}
\frac{\partial(S,T)}{\partial(P,T)} &= \frac{\partial(S,T)}{\partial(V,T)} \cdot \frac{\partial(V,T)}{\partial(P,T)} \\
\implies \left(\frac{\partial S}{\partial P}\right)_T &= \left(\frac{\partial S}{\partial V}\right)_T \left(\frac{\partial V}{\partial P}\right)_T \\
\implies \left(\frac{\partial V}{\partial T}\right)_P &= -\left(\frac{\partial P}{\partial T}\right)_V \left(\frac{\partial V}{\partial P}\right)_T \\
\therefore \left(\frac{\partial P}{\partial T}\right)_V &= \beta K_T
\end{aligned} \tag{2.22}$$

A similar application of the Jacobian yields

$$\begin{aligned}
\frac{\partial(P,V)}{\partial(S,V)} &= \frac{\partial(P,V)}{\partial(T,V)} \cdot \frac{\partial(T,V)}{\partial(S,V)} \\
\therefore \left(\frac{\partial P}{\partial S}\right)_V &= \left(\frac{\partial P}{\partial T}\right)_V \Big/ \left(\frac{\partial S}{\partial T}\right)_V = \frac{\beta T K_T}{C_V}
\end{aligned} \tag{2.23}$$

where C_V is the heat capacity at constant volume. If we now use the results (2.22) and (2.23), the pressure differential form (2.20) can then be simplified.

$$dP = \frac{\beta K_T}{C_V} dU + \left(\frac{\beta K_T}{C_V} P - \frac{K_S}{V} \right) dV \tag{2.24}$$

Furthermore, using the continuity (2.7) and the energy (2.9) equations, this result becomes

$$\frac{dP}{dt} = -K_S \nabla \cdot \mathbf{u} + \frac{\beta K_T V}{C_V} \Phi + \frac{\beta K_T V}{C_V} \nabla \cdot (k \nabla T) \tag{2.25}$$

$$\frac{1}{K_S} \frac{dP}{dt} = -\nabla \cdot \mathbf{u} + \frac{\beta V}{C_P} \Phi + \frac{\beta V}{C_P} \nabla \cdot (k \nabla T) \tag{2.26}$$

using the thermodynamic relation $\gamma = C_P/C_V = K_S/K_T$. The next step is to eliminate the temperature in the above equation. To achieve this, we introduce pressure as a thermodynamic state function of temperature and volume of a fluid element. The associated differential form becomes

$$\begin{aligned} dP &= \left(\frac{\partial P}{\partial T} \right)_V dT + \left(\frac{\partial P}{\partial V} \right)_T dV \\ \therefore dP &= \beta K_T dT - \frac{K_T}{V} dV \end{aligned} \tag{2.27}$$

Now consider a test element located at $\mathbf{r}$ and has a domain of influence $\Omega_h(\mathbf{r})$. Let there be a support material element located at $\mathbf{r}' \in \Omega_h(\mathbf{r})$. From the continuous flow assumption, these two particles will remain neighbors throughout the evolution of the system. Therefore, we can study the variation of the support element's pressure $P(\mathbf{r}', t)$ in the neighborhood of the test element at a specified time t. Using Taylor series expansion the pressure of the support fluid element can be expanded as

$$\begin{aligned} P(\mathbf{r}', t) &= P(\mathbf{r}, t) + (\mathbf{r}' - \mathbf{r}) \cdot \frac{\partial}{\partial \mathbf{r}} P(\mathbf{r}, t) + \mathcal{O}(||\mathbf{r}' - \mathbf{r}||^2) \\ dP(\mathbf{r}, t) &= \delta \mathbf{r} \cdot \nabla P(\mathbf{r}, t) + \mathcal{O}(||\delta \mathbf{r}||^2), \ ||\delta \mathbf{r}|| < h \end{aligned} \tag{2.28}$$

where $\delta \mathbf{r} := \mathbf{r}' - \mathbf{r}$ is the relative position and $dP(\mathbf{r}, t) := P(\mathbf{r}', t) - P(\mathbf{r}, t)$ is the relative pressure between the two neighboring fluid elements at time t. Similar expressions for the temperature and volume of the test element can be obtained. Combining (2.27) and (2.28) yields

$$\delta \mathbf{r}(t) \cdot \left(-\beta K_T \nabla T + \frac{K_T}{V} \nabla V + \nabla P \right) = 0 \tag{2.29}$$

Since no two fluid particles occupy the same position at any time t, we have that the element $\delta \mathbf{r}(t)$ can never be zero at any specified time t. For (2.29) to vanish, we have that

$$\nabla T = -\frac{1}{\beta \rho} \nabla \rho + \frac{\gamma}{\beta K_S} \nabla P \tag{2.30}$$

Physically, within the fluid bulk temperature gradients ∇T and density gradients $\nabla \rho$ are very small for most fluid flows of interest under standard conditions of temperature and pressure.

However, according to (2.30), pressure gradients are still large because the incompressibility modulus K_S is very large for most fluids and solids. Simplifying (2.26) and (2.30) gives

$$\frac{1}{K_S}\frac{dP}{dt} = -\nabla\cdot\mathbf{u} + \frac{\beta}{\rho c_p}\nabla\cdot\left(\frac{\gamma k}{\beta K_S}\nabla P\right) - \frac{\beta}{\rho c_p}\nabla\cdot\left(\frac{k}{\beta\rho}\nabla\rho\right) + \frac{\beta}{\rho c_p}\Phi \tag{2.31}$$

where the specific heat capacity is defined as the heat capacity per unit mass i.e. $c_p = C_P/m$ and the adiabatic index $\gamma = C_P/C_V = K_S/K_T$. Note that since $\gamma > 1$ for all substances, $K_S > K_T > 0$ and $C_P > C_V > 0$ are valid for all materials.

Similar pressure equations for ideal gases, based on a different set of assumptions was developed by Zang et.al. [21] and recently by Claussen [14]. A significant assumption in his work is that density (volume) fluctuations are identically zero $dV = 0$. Such a constraint is avoided in this formulation.

When combined with the continuity (2.7) and momentum (2.8) equations, (2.31) forms a complete system for the solution of weakly compressible flows. With this approach, physically, the propagation of pressure waves within the fluid is damped via an entropy generating mechanism.

2.4.1 Coefficients of Differential Susceptibility

Equation (2.31) is the general form of the proposed pressure equation. However, we can introduce several simplifying assumptions on the experimentally measurable thermodynamic variables β, γ, k, and c_p to obtain a simplified version of (2.31). These quantities, in general, are not constants but functions of the thermodynamic state. By nature, they are coefficients of differential susceptibility: they tell us how, when we hold-all-variables-but-one fixed and differentially "perturb the system," the solitary unconstrained variable responds. These coefficients all arise from perturbation processes that are by nature calorimetric. In this work, however, the assumption is that they are temperature independent and thus taken to be constant. Under this assumption, (2.31) results in a simplified version which is shown as

$$\frac{1}{K_S(P)}\frac{dP}{dt} = -\nabla\cdot\mathbf{u} + \gamma\alpha\nabla\cdot\left(\frac{1}{K_S(P)}\nabla P\right) - \alpha\nabla\cdot\left(\frac{1}{\rho}\nabla\rho\right) + \frac{\alpha\beta}{k}\Phi \tag{2.32}$$

assuming that the incompressibility modulus $K_S = K_S(P)$ varies with pressure. Here $\alpha = k/(\rho c_p)$ is the thermal diffusivity.

2.4.2 Isentropic Flow

In this section we have derived an evolution equation for pressure for a generic fluid flow. But there are idealized situations in which this equation can be further simplified. The condition of zero viscosity or thermal diffusivity results in the conservation of entropy $dS = 0$ and we say the flow is isentropic. This is an idealized thermodynamic process that is adiabatic and in which work transfers are frictionless. The simplifying feature of isentropic flow is that exchanges between the internal energy and other forms of energy are reversible, and the internal energy and temperature play passive roles; merely changing in response to the compression of a material element.

The incompressibility modulus is, in general, dependent on both temperature and pressure, i.e. $K_S = K_S(P,T)$, $K_T = K_T(P,T)$. In this work we assume that temperature dependence is negligible, and that the incompressibility modulus varies linearly with pressure.

$$K_S = K_S|_{p=0} + \left.\frac{dK_S}{dP}\right|_{P=0} \cdot P = K_{0,S} + \gamma P \tag{2.33}$$

where $K_{S,0}$ is the adiabatic incompressibility modulus under standard conditions. The parameter γ must be determined empirically. For isentropic flows, since the thermal diffusivity is zero, the last three terms of (2.32) vanish. In that case, the pressure equation reduces to a simple differential form where pressure is barotropic

$$dP(\rho) = (K_{S,0} + \gamma P)\frac{d\rho}{\rho}, \quad P|_{\rho=\rho_0} = 0, \quad K_{S,0} = \rho\left.\frac{\partial P}{\partial \rho}\right|_{S,\rho=\rho_0} \tag{2.34}$$

which is an exact differential. A simple integration of the above gives the following equation of state originally derived by Monaghan [16].

$$P(\rho) = \frac{1}{\gamma}K_{S,0}\left[\left(\frac{\rho}{\rho_0}\right)^{\gamma} - 1\right] \tag{2.35}$$

This has become the default equation of state in SPH and has been successfully applied to many continuum fluid and solid mechanics problems the first of which were performed by Monaghan [16, 22]. With a further observation that for weakly compressible flows, density fluctuations are small (dictated by the Mach number). If we set the density to $\rho := \rho_0 + \delta\rho$, using the Taylor series expansion of (2.35) yields another alternative equation of state proposed by Muller et.al [23].

$$P(\rho) = K_{S,0}\left(\frac{\rho}{\rho_0} - 1\right) \tag{2.36}$$

The adiabatic incompressibility modulus is related to the adiabatic sound speed c_s within the fluid by $K_{S,0} = \rho_0 c_{s,0}^2$.

For the special case of ideal gas we have that the adiabatic incompressibility modulus is $K_S = \gamma P$ meaning that $K_{S,0} \equiv 0$. For this idealized case, by solving (2.34) one obtains the famous equation of state $P(\rho) = A\rho^{\gamma}$. Then the final system becomes

$$\frac{d\rho}{dt} = -\rho\nabla\cdot\mathbf{u} \tag{2.37}$$

$$\rho\frac{d\mathbf{u}}{dt} = -\nabla P + \nabla\cdot\underline{\underline{\sigma}} + \rho\mathbf{b} \tag{2.38}$$

$$\kappa_s\frac{dP}{dt} = -\nabla\cdot\mathbf{u} + \gamma\alpha\nabla\cdot(\kappa_s\nabla P) - \alpha\nabla\cdot(v\nabla\rho) + \frac{\alpha\beta}{k}\Phi \tag{2.39}$$

where the compressibility is the inverse of the incompressibility modulus and is given by $\kappa_s := 1/K_S = 1/(K_{S,0} + \gamma P)$ varying linearly with pressure. For an ideal gas $K_{S,0} = 0$ whereas for liquids it is defined through the standard adiabatic speed of sound $K_{S,0} = \rho_0 c_{s,0}^2$. The sound speed in the pressure equation affects the time step due to the Courant-Friedrchs-Lewy, CFL constraint. The speed of sound for most fluid flows of interest is generally very

high. For instance, the speed of sound in water is 1500ms^{-1}. This leads to a prohibitively large incompressibility modulus $K_{S,0} = \rho_0 c_{s,0}^2 = 2.25 \times 10^9$Pa requiring very small time integration to resolve information transfer by acoustic waves. Instead, we enforce artificial incompressibility[22][16] via the Mach number

$$\text{Ma}^2 := \frac{\rho U^2}{K_s} = \frac{U^2}{c_s^2} \approx \left|\frac{\delta\rho}{\rho}\right| \tag{2.40}$$

Monaghan[16] proposes lowering the incompressibility modulus to enforce artificial incompressibility. With a Mach Number of $\text{Ma} = 0.1$, density fluctuations are on the order of 1%. This means that the speed of is 10 times the maximum velocity of the problem under investigation. For dam break problems we have $c_s = 10\sqrt{2gh_0}$ and for periodic waves on a slope $c_s = 10\sqrt{gh_0}$ where h_0 is the local depth. For all problems studied in this thesis, this approach is adopted. In the discussion that follows the following integral transforms will be used. Their detailed derivation will be dealt with in later sections.

$$\langle P_h(\mathbf{r})\rangle := \int_{\Omega_h(\mathbf{r})} P(\mathbf{r}')w_h(\mathbf{r}-\mathbf{r}')d\Omega(\mathbf{r}') \tag{2.41}$$

$$\begin{aligned} L_h(\kappa^s, P) &:= \nabla\cdot(\kappa^s\nabla P) \\ &= \int_{\Omega_h(\mathbf{r})} \left[\kappa^s(\mathbf{r})\Big(\langle P_h(\mathbf{r})\rangle - \langle P_h(\mathbf{r}')\rangle\Big) + \langle\kappa_h^s(\mathbf{r}')\rangle\Big(P(\mathbf{r}) - P(\mathbf{r}')\Big)\right] \\ &\quad\times \frac{(\mathbf{r}-\mathbf{r}')\cdot\nabla\varphi_h}{||\mathbf{r}-\mathbf{r}'||^2} d\Omega(\mathbf{r}') \end{aligned} \tag{2.42}$$

2.5 Causality

We next discuss the numerical implications of our explicit model. Numerical methods, in general, have their own condition for causality called the CFL stability criterion. The proposition is that numerical causality coincides with physical causality as the grid spacing approaches zero. We now discuss the implications of this proposition on the numerical analysis of the pressure equation (2.32).

The stability criterion on the diffusion term in the pressure equation can be calculated independently of the equations of motion since its stability is dependent on the thermal timescale rather than the dynamic timescale. Thus, the pressure equation now reads

$$\frac{dP}{dt} = \gamma\alpha\nabla^2 P \tag{2.43}$$

for the simple case of constant adiabatic compressibility. For this analysis we have ignored the thermal dissipation term and further assumed that density gradients are negligible.

We will now consider a numerical fluctuation around a homogeneous state corresponding to the fluid equilibrium, i.e. $\rho(\mathbf{r}) = \bar{\rho}$, $P(\mathbf{r}) = \bar{P}$. If the system is now perturbed from equilibrium, we have

$$\begin{aligned} \mathbf{r} &= \bar{\mathbf{r}} + \delta\mathbf{r} \\ \rho(\mathbf{r}) &= \bar{\rho} + \delta\rho(\mathbf{r}) \\ P(\mathbf{r}) &= \bar{P} + \delta P(\mathbf{r}) \end{aligned} \tag{2.44}$$

Then the first order perturbation equation using (2.44) is

$$\frac{d}{dt}\delta P(\mathbf{r}) = 2\gamma\alpha \int_{\Omega_h(\mathbf{r})} \left(\delta P(\mathbf{r}) - \delta\langle P_h(\mathbf{r}')\rangle\right) \frac{(\mathbf{r}-\mathbf{r}')\cdot\nabla\varphi_h}{||\mathbf{r}-\mathbf{r}'||^2} d\Omega(\mathbf{r}') \tag{2.45}$$

If we assume that the perturbation can be written in the form

$$\delta P = Q(t)e^{\mathbf{i}\mathbf{k}\cdot\mathbf{r}} \tag{2.46}$$

then equation (2.45) takes the form

$$\frac{d}{dt}Q(t) = 2\gamma\alpha I(h,k)Q(t) \tag{2.47}$$

where we have used the definition $I := I(h,k)$ which depends on the choice of convolution/deconvolution kernel used.

$$I(h,k) = \int_{\Omega_h(\mathbf{r})} \left(1 - e^{-\mathbf{i}\mathbf{k}\cdot(\mathbf{r}-\mathbf{r}')}\right) \frac{(\mathbf{r}-\mathbf{r}')\cdot\nabla\varphi_h}{||\mathbf{r}-\mathbf{r}'||^2} d\Omega(\mathbf{r}') \tag{2.48}$$

When the leapfrog method is applied to the absolute stability model (2.47) we have

$$Q_{n+1} = Q_{n-1} + 2\Delta t\lambda Q_n\ , \quad \lambda := 2\gamma\alpha I(h,k) > 0 \tag{2.49}$$

The corresponding characteristic polynomial is given by $M_w(r) = r^2 - 2wr - 1$ with $w := \lambda\Delta t$. Since w is real and positive, the leapfrog method has two distinct roots $r_\pm = w \pm \sqrt{1+w^2}$. Using the binomial expansion we have $r_+ = 1 + w + w^2/2 - w^3/8 + \cdots$, $|w| < 1$; i.e. for small $|w|$, one step of the mode r_+ of the leapfrog method agrees with the terms of order $\leq w^2$ in the exact solution and the remainder is bounded by a multiple of w^3. We formally have the time constraint as

$$\Delta t \leq \frac{1}{2}\frac{1}{\gamma\alpha I(h,k)} \tag{2.50}$$

For a Gaussian filter we have $I = 2/h^2$. And the stability condition becomes,

$$\Delta t \leq \frac{1}{4}\frac{h^2}{\gamma\alpha} \tag{2.51}$$

We then conjecture that for some parameter $0 < C_\alpha \leq 1$, the generalized stability condition is

$$\Delta t \leq C_\alpha \frac{h^2}{\gamma\alpha} \tag{2.52}$$

A numerical method is said to be stable if the errors in the method do not increase as the solution advances in time. Furthermore, a numerical method is consistent if truncation errors go to zero as $h,\ \Delta t \to 0$. Similarly, convergence is important and requires that the solution of the finite difference equation (FDE) converges to the exact solution in the limit $h,\ \Delta t \to 0$. According to the Lax equivalence theorem, if a finite difference method is consistent (FDE approaches the underlying PDE as grid spacing shrinks to zero) and stable (errors do not grow) then convergence is guaranteed. In short, consistence and stability imply convergence.

2.6 Conclusion

An alternative approach for enforcing pseudo-incompressibility that accommodates liquids and gases in general has been proposed. A connection to standard equations of state commonly used in SPH has been made. The mathematical structure of the derived equation for pressure reveals that there are diffusion terms that should consequently smooth out any spurious numerical noise in the pressure field and should thus accomplish the same objective as that of the $\delta-$SPH concept. Whether the proposed model of the pressure equation preserves the hydrostatic condition will be investigated in the later sections.

Furthermore, a causality analysis was carried out and the associated constraint on the time step was derived.

Chapter 3

Elements of Filtering and De-filtering

The main goal of this chapter is define filtering and de-filtering rules for compressible flows. With proper choice of these rules, convolution (filtering) and deconvolution (de-filtering) operators on $\mathbb{R}^2$ are derived. Then the corresponding convolution and deconvolution filter pairs are constructed.

3.1 Problem statement

Standard SPH as well as LES are based on the convolution integral. Field variables are localized on compact spaces to construct macroscopic variables that are smooth over these local continua. This procedure is called local averaging: a deterministic process since no statical mechanics ideas are taken into account.

We start with continuum form of the CNSEs for a fluid.

$$\frac{d}{dt}\rho = -\rho\nabla\cdot\mathbf{u} \tag{3.1}$$

$$\kappa_s(p)\frac{d}{dt}p = -\nabla\cdot\mathbf{u}+\gamma\alpha\nabla\cdot(\kappa_s(p)\nabla p)-\alpha\nabla\cdot\left(\rho^{-1}\nabla\rho\right) \tag{3.2}$$

$$\rho\frac{d}{dt}\mathbf{u} = -\nabla p+\nabla\cdot\underline{\underline{\sigma}}+\rho\mathbf{b} \tag{3.3}$$

$$\frac{d\mathbf{r}}{dt} = \mathbf{u} \tag{3.4}$$

The convolution or filtering problem can be stated formally as: Given the continuum field$\{\rho(\mathbf{r}),\ p(\mathbf{r}),\ \mathbf{u}(\mathbf{r})\}$ defined on a domain Ω, compute local approximations $\{\langle\rho_h(\mathbf{r})\rangle,\ \langle p_h(\mathbf{r})\rangle,\ \widetilde{\mathbf{u}}_h(\mathbf{r})\}$ which faithfully represent the behavior of the continuum field on scales above some, user defined, filter length (here denoted h) and which truncates scales smaller than $\mathcal{O}(h)$.

Similarly, the deconvolution or de-filtering problem can be stated as: Given the local approximations $\{\langle\rho_h(\mathbf{r})\rangle,\ \langle p_h(\mathbf{r})\rangle,\ \widetilde{\mathbf{u}}_h(\mathbf{r})\}$ find an accurate reconstruction of the continuum field $\{\rho(\mathbf{r}),\ p(\mathbf{r}),\ \mathbf{u}(\mathbf{r})\}$. When the filter is smoothing,

$$\widetilde{l}_h : L^2(\Omega_h)\to L^2(\Omega_h) \quad \text{by } \rho(\mathbf{r})\to\langle\rho_h(\mathbf{r})\rangle \tag{3.5}$$

$\widetilde{l}_h$ is compact and the deconvolution is ill-posed. While stable exact deconvolution is not possible, we shall instead utilize an approximate deconvolution approach.

The main goal of this paper is to develop the filtering integral transform (FIT) and the de-filtering integral transform (DIT) that form a transform pair with compatible operators that perform filtering and de-filtering processes.

We further emphasize that SPH is a zeroth order approximate deconvolution model meaning that fluctuations are negligibly small so that the following approximations are assumed to hold; $\langle \rho_h \rangle \approx \rho$, $\langle p_h \rangle \approx p$ and $\mathbf{u}_h \approx \widetilde{\mathbf{u}}_h$. The reason for this assumption is to achieve closure. To this end, we propose an n^{th} order approximate deconvolution model called de-filtered SPH or SPH$-i$ for short. Unlike SPH, SPH$-i$ has no closure problem hence it is a complete model.

The final task in this paper is to (i) apply the FIT to CNSEs (3.1), (3.2), and (3.3) to derive continuous SPH that is an integral form of LES i.e. the filtered equations. (ii) apply approximate deconvolution to the filtered equations to obtain a particle method SPH$-i$ and (iii) construct compatible convolution and deconvolution filters.

In the following sections, we first introduce the essential elements of vector spaces with non-denumerable basis states using Dirac notation. Where necessary, rigorous mathematical derivations are given.

3.2 Local Averaging (physical motivation)

In order to derive the filtered conservation laws for a discrete fluid, we need locally averaged variables. Using ideas of distribution theory, physical attributes of fluid particles constituting the discrete fluid such as mass density, momentum density, and velocity are replaced by local mean variables obtained by averaging the point variables over small local regions (test spaces) containing many fluid particles but are still small compared with the scale of macroscopic variation from point to point within the system, Jackson [24].

In science and engineering, in order to measure the amount of a physical quantity such as temperature at a single point, one needs a probe which can extract data only from that single point of interest in space. Since this is not possible practically, there is no way we can correlate the experimental data with theoretical predictions. Therefore, a true macroscopic quantity is by necessity an average over some spatial region surrounding the continuum point where it is nominally defined, Admal et.al.[25].

Consider a function $T(\mathbf{r})$ as representing a value of the physical variable at a particular point $\mathbf{r}$ in space. Is this a realistic thing to do? What can we measure?

Suppose $T(\mathbf{r})$ represents temperature at a point $\mathbf{r}$ in a room Ω. The temperature can be measured with a thermometer by placing the bulb at the point $\mathbf{r}$. Unlike the point, the bulb has nonzero size, so what the thermometer actually measures is the mean temperature over a small region of space $\Omega_h(\mathbf{r}) := \{\mathbf{r}, \mathbf{r}' \in \mathbb{R}^n | w_h(\mathbf{r} - \mathbf{r}') \geq 0, ||\mathbf{r} - \mathbf{r}'|| \leq \kappa h \, , \kappa \in \mathbb{R}^+\}$. So really, the thermometer measures

$$\langle T_h(\mathbf{r}) \rangle \quad = \quad \int_{\Omega_h(\mathbf{r})} T(\mathbf{r}') w_h(\mathbf{r} - \mathbf{r}') d^n \mathbf{r}' \tag{3.6}$$

where $w_h := w_h(\mathbf{r} - \mathbf{r}')$ depends on the *nature* of the thermometer and *where* you place it. w_h will tend to be "concentrated" near the location of the thermometer bulb and nearly zero once you are sufficiently far away from the bulb. To say this is an average requires that $^{\forall}\mathbf{r}, \mathbf{r}' \in \Omega_h(\mathbf{r}) \subset \mathbb{R}^n$;

(1) semi-positive definiteness

$$w_h \geq 0 \tag{3.7}$$

(2) normalization

$$\int_{\Omega_h(\mathbf{r})} w_h(\mathbf{r}-\mathbf{r}')d^n\mathbf{r}' = 1 \tag{3.8}$$

So it would be more meaningful to discuss things like the local average $\langle T_h(\mathbf{r})\rangle$ rather than things like the value of T at a point, $\mathbf{r} \mapsto T(\mathbf{r})$.

Remark 3.2.1 (key points)**.** *The key points thus far*

- *How do we understand T?*
  only by $\langle T_h\rangle := \langle T, w_h\rangle$.
- *If so, then what does the derivative* ∇T *mean?*
  must understand $\langle \nabla T, w_h\rangle$

3.3 Preliminaries

This section introduces essential elements of the Dirac notation that will be useful in developing the filtering and de-filtering transform pair.

3.3.1 Useful terms for flow description

Definition 3.3.1 (fluid parcel)**.** *Let* $\Omega \subseteq \mathbb{R}^n$ *be a fluid domain. We define a fluid parcel* $\mathcal{W} \subset \Omega$ *as the volume moving with the fluid within* Ω*.*

Definition 3.3.2 (material or Lagrangian derivative)**.** *The material derivative operator is defined as* $\frac{d}{dt} := \frac{\partial}{\partial t} + \mathbf{u}\cdot\nabla$*. Then the derivative of* ρ *along a particle's trajectory* $\mathbf{r}(t)$ *is given by* $\frac{d}{dt}\rho(\mathbf{r}(t))$

Definition 3.3.3 (fluid domain)**.** *Let* $\Omega \subseteq \mathbb{R}^n$ *be an open set bounded by a smooth surface* $\partial\Omega$*. If* Ω *is supposed to be "filled with a fluid" such that the mass-density*

$$\rho(\mathbf{r}) > 0, \qquad {}^{\forall}\mathbf{r} \in \Omega \tag{3.9}$$

then we call Ω *a fluid domain.*

Definition 3.3.4 (Test Element)**.** *This is a material element whose physical attributes are to be measured or probed.*

Definition 3.3.5 (Test Space)**.** *Let* $\Omega \subset \mathbb{R}^n$ *be a given body. For a test element located at* $\mathbf{r}$*, we denote its test space as* $\Omega_h(\mathbf{r})$ *bounded by a test surface* $\partial\Omega(\mathbf{r})$*. The test space is thus the domain of influence of the test element.*

$$\Omega_h(\mathbf{r}) \equiv \text{Supp}(w_h) = \left\{\mathbf{r}, \mathbf{r}' \in \mathbb{R}^n | w_h(\mathbf{r}-\mathbf{r}') \geq 0, ||\mathbf{r}-\mathbf{r}'|| \leq \kappa h \ , \kappa \in \mathbb{R}^+\right\} \tag{3.10}$$

3.3.2 Invertibility of operators

A linear operator $\hat{C}_h$ has a left inverse $\hat{L}_h$ if $\hat{L}_h\hat{C}_h = \hat{1}$ and a right inverse $\hat{R}_h$ if $\hat{C}_h\hat{R}_h = \hat{1}$. Furthermore, if both exist, we have that

$$\hat{L}_h \;=\; \hat{L}_h\hat{1} = \left(\hat{L}_h\hat{C}_h\right)\hat{R}_h = \hat{1}\hat{R}_h = \hat{R}_h \tag{3.11}$$

which is very useful for infinite dimensional vector spaces. Therefore, if an operator has both a left and a right inverse, then the left inverse is the same as the right inverse and we say that the operator is invertible.

A left inverse exists if the action of the operator on some input vector does not result in irreparable damage so that whatever remains still contains enough information that some linear operator $\hat{L}_h$ can restore our original input vector and give back the identity operator. This condition of irreparable damage i.e. not losing information is asking whether the operator $\hat{C}_h$ is injective. There exists a left inverse if and only if $\hat{C}_h$ is injective.

For the right inverse to exist, the situation is dual to that of the left inverse; a right inverse exists if $\hat{C}_h$ is surjective.

In particular, if $\hat{C}_h$ is an operator in a finite dimensional space V i.e. $dimV < \infty$ then the following is true.

$$\hat{C}_h\text{is injective} \iff \hat{C}_h\text{is surjective} \iff \hat{C}_h\text{is invertible} \tag{3.12}$$

$\hat{C}_h$ is surjective if and only if $\hat{C}_h$ is injective because failure to be injective and failure to be surjective are both equivalent to loss of information. This can be seen from the dimension formula for a finite vector space

$$\text{dim}V = \text{dim}\left(\text{null}\hat{C}_h\right) + \text{dim}\left(\text{range}\hat{C}_h\right) \tag{3.13}$$

It is clear that if $\text{dim}\left(\text{null}\hat{C}_h\right) = 0$, then $dim\left(\text{range}\hat{C}_h\right)$ is the whole vector space. Furthermore, if $\text{dim}\left(\text{null}\hat{C}_h\right) \neq 0$, then $\text{dim}\left(\text{range}\hat{C}_h\right)$ is not the whole vector space.

The equivalence (3.13) breaks down if the vector space is infinite dimensional. For infinite dimensional vector spaces injectivity and surjectivity are not equivalent since each can fail independently.

$$\hat{C}_h\text{is invertible} \iff \hat{C}_h\text{is injective and surjective} \tag{3.14}$$

In the discussions that follow, we are going to assume that the convolution operator $\hat{C}_h$ is invertible and arbitrary.

3.3.3 Resolution of Identity

Position states for describing the continuum mechanics of material elements or fluid particles moving in an n-dimensional space $\mathbf{r}, \mathbf{r}' \in \Omega_h(\mathbf{r}) \subset \mathbb{R}^n$ are defined as follows

$$\text{position basis state}: \quad |\mathbf{r}\rangle \equiv |x, y, z\rangle, \quad {}^{\forall}x, y, z \in \mathbb{R} \tag{3.15}$$

where the label $\mathbf{r} = \mathbf{r}(t)$ in the ket is the position of a material element or its trajectory. Since particle trajectories are continuous and we position states $|\mathbf{r}\rangle$ for all $\mathbf{r}$ to form a basis, we are dealing with a non-denumerable or infinite basis. Therefore the ket is a vector in infinite dimensional vector space of states of the theory. The $|\ \rangle$ enclosing the label of the position eigenstates plays a crucial role: it helps us to see that that object lives in an infinite dimensional vector space. Basis states with different values of $\mathbf{r}$ are different vectors in the state space. The inner product must be defined, so we take

$$\langle \mathbf{r}|\mathbf{r}'\rangle = \delta(\mathbf{r}-\mathbf{r}') \equiv \delta(x-x')\delta(y-y')\delta(z-z'), \quad {}^{\forall}x, y, z \in \mathbb{R} \tag{3.16}$$

It then follows that position states with different positions are orthogonal to each other. The norm of position states is infinite: $\langle \mathbf{r}|\mathbf{r}\rangle = \delta(0) = \infty$, so these are not allowed states of particles. This also implies that no two fluid particles can occupy the same position at the same time.

We visualize the state $|\mathbf{r}\rangle$ as the state of a fluid particle perfectly localized at position $\mathbf{r}$, but this is just an idealization.

Normalizable states can be easily constructed by using superposition of position states using the completeness relation or resolution of identity

$$\int_{\Omega_h(\mathbf{r})} |\mathbf{r}'\rangle\langle\mathbf{r}'| d\Omega(\mathbf{r}') = \hat{1} \tag{3.17}$$

which is consistent with the inner product (3.16). At this point we introduce a new state vector describing the mass density of a fluid particle

$$\text{mass density state:} \quad |\rho\rangle, \quad \rho > 0 \text{ on } \Omega = \mathbb{R}^n \tag{3.18}$$

To project operators into function space we simply take an overlap of the coordinate basis state $\langle\mathbf{r}|$ with the state $|\rho\rangle$ yielding the value of the real-valued function ρ at position $\mathbf{r}$; namely

$$\rho(\mathbf{r}) = \langle\mathbf{r}|\rho\rangle \in \mathbb{R} \tag{3.19}$$

3.4 Filtering and De-filtering Integral Transform Pair

In this section we present Filtering Integral Transform (FIT) and De-filtering Integral Transform (DIT) that will later be used to filter and de-filter the CNSEs. We first introduce convolution and deconvolution operators on infinite dimensional spaces as abstract operators. In section 3.5 we will rigorously construct these operators.

3.4.1 Concept of density-weighted averaging

In the study of turbulence, stochastic methods are used in the description of fluctuations of velocity and scalar fields in terms of their statistical distributions. While our formulations of particle method models do not take into account any statical mechanical efforts and are hence deterministic, this short section is used for the purpose of giving the physical foundations of density-weighted averaging.

Given the velocity field $\mathbf{u} = (u, v, w)^{\mathrm{T}}$, the distribution function $F_u(U)$ of the x-component u is defined by the probability pr of finding a value $u < U$ such that

$$F_u(U) := \mathrm{pr}(u < U) \tag{3.20}$$

where U is called the sample space variable associated with the random stochastic variable u whose sample space consists of all possible realizations of u. The probability of finding a value of u in the interval $U_- < u < U_+$ is defined as

$$\mathrm{pr}(U_- < u < U_+) = F_u(U_+) - F_u(U_-) \tag{3.21}$$

Then the probability density function (pdf) of u is now defined as

$$P_u(U) = P(U) = \frac{d}{dU} F_u(U) \tag{3.22}$$

It thus follows that $P_u(U)dU$ is the probability of finding u in the interval $U < u < U + dU$. Summing up over the entire space leads to

$$\int_{-\infty}^{\infty} P_u(U)dU = 1 \tag{3.23}$$

meaning that the probability of finding u in the range $-\infty < u < \infty$ is certain. This also serves as the normalization condition for the pdf. In general the pdf also depends on position and time.

To introduce density-weighted averages (also called Favre averages), knowledge of the correlation between density ρ and any other variable of interest is essential. Given the joint pdf $P(\rho, u)$, the Favre pdf of u can be derived as follows.

$$\bar{\rho}\widetilde{P}(u) = \int_{\rho_{min}}^{\rho_{max}} \rho P(\rho, u)d\rho = \int_{\rho_{min}}^{\rho_{max}} \rho P(\rho|u)P(u)d\rho = \langle \rho, u \rangle P(u) \tag{3.24}$$

If we now multiply both sides of (3.24) by u and integrating over the entire space yields

$$\bar{\rho} \int_{-\infty}^{\infty} u\widetilde{P}(u)du \int_{-\infty}^{\infty} u\langle \rho, u \rangle P(u)du \tag{3.25}$$

which is equivalent to

$$\bar{\rho}\widetilde{u} = \overline{\rho u} \tag{3.26}$$

3.4.2 Filtering Integral Transform (FIT)

The convolution or filtering problem can be stated formally as follows: Given the continuum field$\{\rho(\mathbf{r}), p(\mathbf{r}), \mathbf{u}(\mathbf{r})\}$ defined on a domain Ω, compute local approximations $\{\langle \rho_h(\mathbf{r}) \rangle$, $\langle p_h(\mathbf{r}) \rangle$, $\widetilde{\mathbf{u}}_h(\mathbf{r})\}$ which faithfully represent the behavior of the continuum field on scales above some, user defined, filter length (here denoted h) and which truncates scales smaller than $\mathcal{O}(h)$.

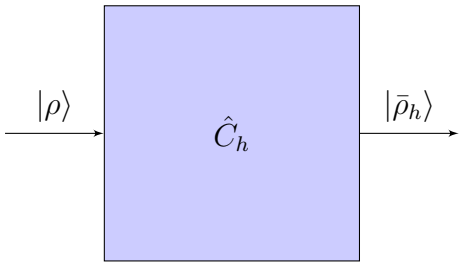

Figure 3.1: Convolution process. The output state $|\bar{\rho}_h\rangle$ acquires the smoothness property of the convolution operator as well as scale-dependence.

Assuming that the convolution operator $\hat{C}_h : L^2(\Omega_h) \to L^2(\Omega_h)$ is invertible. Then, in operator form we have

$$|\bar{\rho}_h\rangle = \hat{C}_h|\rho\rangle \tag{3.27}$$

The above result can be pictured in function space by multiplying from the left by the bra vector $\langle\mathbf{r}|$ and inserting the identity operator as follows

$$\begin{aligned}
\langle\mathbf{r}|\bar{\rho}_h\rangle &= \langle\mathbf{r}|\hat{C}_h\hat{1}|\rho\rangle \\
&= \langle\mathbf{r}|\hat{C}_h \int_{\Omega_h(\mathbf{r})} |\mathbf{r}'\rangle\langle\mathbf{r}'|d\Omega(\mathbf{r}')|\rho\rangle \\
&= \int_{\Omega_h(\mathbf{r})} \langle\mathbf{r}|\hat{C}_h|\mathbf{r}'\rangle\langle\mathbf{r}'|\rho\rangle d\Omega(\mathbf{r}') \\
\langle\rho_h(\mathbf{r})\rangle &= \int_{\Omega_h(\mathbf{r})} \rho(\mathbf{r}')w_h(\mathbf{r}-\mathbf{r}')d\Omega(\mathbf{r}')
\end{aligned} \tag{3.28}$$

where $\langle r|\bar{\rho}_h\rangle = \langle\rho_h(\mathbf{r})\rangle$ is the smoothed or filtered mass density. The convolution filter is defined as the "matrix element" of the convolution operator $\hat{C}_h$, i.e. $w_h(\mathbf{r}-\mathbf{r}') := \langle\mathbf{r}|\hat{C}_h|\mathbf{r}'\rangle$.

Similar results can be obtained for the momentum density and pressure. With brevity, we present these in the following proposition.

Proposition 3.4.1 (FIT for fluids)**.** *Let $\Omega_h(\mathbf{r})$ be a locally compact space within the fluid domain Ω. Then the filtered mass density, momentum density and pressure are given by the FIT; for each $w_h \in C_c^\infty(\Omega_h)$*

$$\langle\rho_h(\mathbf{r})\rangle = \int_{\Omega_h(\mathbf{r})} \rho(\mathbf{r}')w_h(\mathbf{r}-\mathbf{r}')d\Omega(\mathbf{r}') \tag{3.29}$$

$$\langle\rho_h(\mathbf{r})\rangle\widetilde{\mathbf{u}}_h(\mathbf{r}) = \int_{\Omega_h(\mathbf{r})} \rho(\mathbf{r}')\mathbf{u}(\mathbf{r}')w_h(\mathbf{r}-\mathbf{r}')d\Omega(\mathbf{r}') \tag{3.30}$$

$$\langle p_h(\mathbf{r})\rangle = \int_{\Omega_h(\mathbf{r})} p(\mathbf{r}')w_h(\mathbf{r}-\mathbf{r}')d\Omega(\mathbf{r}') \tag{3.31}$$

The smoothed field $\{\langle\rho_h(\mathbf{r})\rangle, \langle p_h(\mathbf{r})\rangle, \widetilde{\mathbf{u}}_h(\mathbf{r})\}$ represent the interaction of fluid particles located at $\mathbf{r}, \mathbf{r}' \in \Omega_h(\mathbf{r})$.

The FIT is a locally weighted averaging process with the convolution filter w_h weighting some parts of the underlying disordered field $\{\rho, \rho\mathbf{u}, p\}$ more than others. Since the FIT is a type of averaging, it is a "smoothing" process.

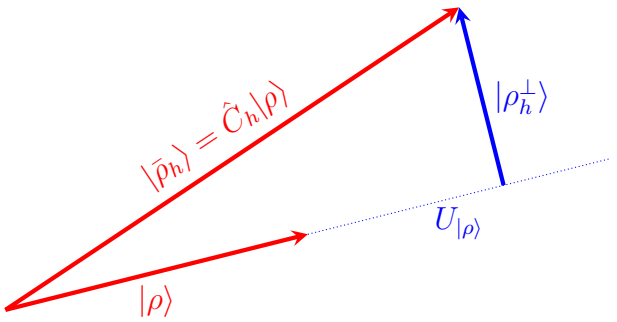

Figure 3.2: The mass density state $|\rho\rangle$ and the subspace $U_{|\rho\rangle}$ generated by it. The effect of the convolution operator is to shift the mass density state $|\rho\rangle$ into a new vector subspace spanned by the deformed state $|\bar{\rho}_h\rangle$. The norm of the orthogonal complement $|\rho^{\perp}\rangle$ is the error in resolving identity using a convolution operator.

3.4.3 Effect of the convolution operator: geometrical analysis

In the SPH method it is well known that the most important element of the method is the convolution kernel. Here, a criteria for measuring the effect of this convolution kernel through a geometrical analysis is presented. Figure 3.2 demonstrates the effect of the convolution operator. Consider the vector subspace $U_{|\rho\rangle}$ generated or spanned by the state $|\rho\rangle$. When the convolution operator $\hat{C}_h$ acts on the undeformed state $|\rho\rangle$ the output is a deformed state $|\bar{\rho}_h\rangle$ that is shifted in a different direction due to the fact that $|\rho\rangle$ is not an eigenstate of the convolution operator. If we define an orthogonal projector to the vector subspace $U_{|\rho\rangle}$

$$\hat{P}_{U_{|\rho\rangle}} := \frac{|\rho\rangle\langle\rho|}{\langle\rho|\rho\rangle} \tag{3.32}$$

Then an orthogonal projection of the state $|\bar{\rho}_h\rangle$ onto $U_{|\rho\rangle}$ yields

$$\hat{P}_{U_{|\rho\rangle}}|\bar{\rho}_h\rangle = \frac{\langle\rho|\bar{\rho}_h\rangle}{\langle\rho|\rho\rangle}|\rho\rangle \tag{3.33}$$

which is the component of the deformed state $|\bar{\rho}_h\rangle$ along the undeformed state $|\rho\rangle$. The orthogonal complement state $|\rho_h^{\perp}\rangle$ spans the subspace $U_{|\rho\rangle}^{\perp}$ and is given by

$$|\rho_h^{\perp}\rangle = |\bar{\rho}_h\rangle - \frac{\langle\rho|\bar{\rho}_h\rangle}{\langle\rho|\rho\rangle}|\rho\rangle \tag{3.34}$$

We then claim that the error or uncertainty in approximating identity using the convolution operator is given by the norm of the perpendicular state.

$$\Delta\hat{C}_h(\rho)^2 = \langle\rho_h^{\perp}|\rho_h^{\perp}\rangle = \langle\bar{\rho}_h|\bar{\rho}_h\rangle - \frac{|\langle\rho|\bar{\rho}_h\rangle|^2}{\langle\rho|\rho\rangle} \tag{3.35}$$

Thus a good convolution operator (kernel) is one that minimizes the error $\Delta\hat{C}_h(\rho)$. It is important to also note that in the continuum limit this error is zero as the convolution operator becomes identical to the identity operator. However, for any practical convolution operator

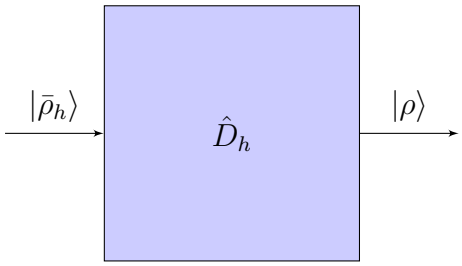

Figure 3.3: Deconvolution process. The output state $|\rho\rangle$ is reconstructed to recover the high frequency components lost during the filtering process.

(kernel) this error is non-zero. Therefore this gives us a measure of how well a convolution operator approximates identity, or equivalently, how well a convolution kernel approximates the Dirac-delta function.

In function space (3.35) is expressed as

$$\Delta\hat{C}_h(\rho)^2 = \int_\Omega |\langle\rho_h(\mathbf{r}')\rangle|^2 d\Omega(\mathbf{r}') - \frac{|\int_\Omega \rho(\mathbf{r}')\langle\rho_h(\mathbf{r}')\rangle d\Omega(\mathbf{r}')|^2}{\int_\Omega |\rho(\mathbf{r}')|^2 d\Omega(\mathbf{r}')} \tag{3.36}$$

For spherically symmetric convolution kernels, a Taylor expansion of $\rho(\mathbf{r}')$ about $\mathbf{r}'$ shows that the error is of second order $\Delta\hat{C}_h(\rho) \equiv \mathcal{O}(h^2)$. Clearly, minimizing this error is thus fundamental for better approximation of the resolution of identity using a convolution operator (kernel).

3.4.4 De-Filtering Integral Transform (DIT)

The deconvolution or de-filtering problem can be formally stated as: Given the local approximations $\{\langle\rho_h(\mathbf{r})\rangle, \langle p_h(\mathbf{r})\rangle, \widetilde{\mathbf{u}}_h(\mathbf{r})\}$ find an accurate reconstruction of the continuum field $\{\rho(\mathbf{r}), p(\mathbf{r}), \mathbf{u}(\mathbf{r})\}$.

Assuming that the convolution operator $\hat{C}_h : L^2(\Omega_h) \to L^2(\Omega_h)$ is invertible, then there exists a deconvolution operator $\hat{D}_h : L^2(\Omega_h) \to L^2(\Omega_h)$. Following the derivation above, we start with operator space representation

$$|\rho\rangle = \hat{D}_h|\bar{\rho}_h\rangle \tag{3.37}$$

By taking an overlap with the bra vector $\langle\mathbf{r}|$ and inserting a complete set of states as below, we obtain the de-filtering integral transform in function space.

$$\begin{aligned}
\langle\mathbf{r}|\rho\rangle &= \langle\mathbf{r}|\hat{D}_h\hat{1}|\bar{\rho}_h\rangle \\
&= \langle\mathbf{r}|\hat{D}_h \int_{\Omega_h(\mathbf{r})} |\mathbf{r}'\rangle\langle\mathbf{r}'|d\Omega(\mathbf{r}')|\bar{\rho}_h\rangle \\
&= \int_{\Omega_h(\mathbf{r})} \langle\mathbf{r}|\hat{D}_h|\mathbf{r}'\rangle\langle\mathbf{r}'|\bar{\rho}_h\rangle d\Omega(\mathbf{r}') \\
\rho(\mathbf{r}) &= \int_{\Omega_h(\mathbf{r})} \langle\rho_h(\mathbf{r}')\rangle\varphi_h(\mathbf{r}-\mathbf{r}')d\Omega(\mathbf{r}')
\end{aligned} \tag{3.38}$$

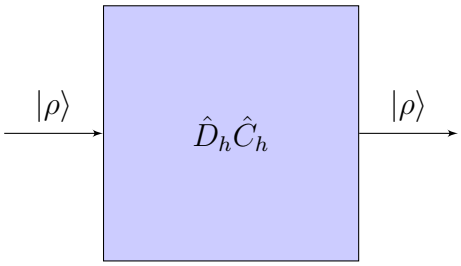

Figure 3.4: Mathematically accurate and consistent completeness property. We exploit the existence of invertible operators to resolve identity.

where $\langle \mathbf{r}|\rho\rangle := \rho(\mathbf{r})$ is the de-filtered particle mass density, assuming perfect reconstruction of the high frequency components. The deconvolution filter is defined as the "matrix element" of the deconvolution operator $\hat{D}_h$, i.e. $\varphi_h(\mathbf{r}-\mathbf{r}') := \langle \mathbf{r}|\hat{D}_h|\mathbf{r}'\rangle$.

Similar results can be obtained for the de-filtered momentum density and pressure. Accordingly, the DIT that forms an exact integral transform pair with the above FIT is given by the following

Proposition 3.4.2 (DIT for fluids)**.** *Consider a fluid particle located at* $\mathbf{r}$ *and has a test space* $\Omega_h(\mathbf{r})$ *within the fluid domain* Ω*. Given the locally averaged mass density, momentum density and pressure on* $\Omega_h(\mathbf{r})$*, we can reconstruct the continuum field by de-filtering the filtered mass density, momentum density and pressure in proposition 3.4.1. Mathematically, for each* $w_h \in C_c^\infty(\Omega_h)$*, there exists a* $\varphi_h \in C_c^\infty(\Omega_h)$ *such that*

$$\rho(\mathbf{r}) = \int_{\Omega_h(\mathbf{r})} \langle \rho_h(\mathbf{r}')\rangle \varphi_h(\mathbf{r}-\mathbf{r}')d\Omega(\mathbf{r}') \tag{3.39}$$

$$\rho(\mathbf{r})\mathbf{u}(\mathbf{r}) = \int_{\Omega_h(\mathbf{r})} \langle \rho_h(\mathbf{r}')\rangle \widetilde{\mathbf{u}}_h(\mathbf{r}')\varphi_h(\mathbf{r}-\mathbf{r}')d\Omega(\mathbf{r}') \tag{3.40}$$

$$p(\mathbf{r}) = \int_{\Omega_h(\mathbf{r})} \langle p_h(\mathbf{r}')\rangle \varphi_h(\mathbf{r}-\mathbf{r}')d\Omega(\mathbf{r}') \tag{3.41}$$

Next, we derive the statement of completeness for the de-filtered mass density to be a true reconstruction of the continuum mass density.

3.4.5 Completeness of filtering and de-filtering processes: integral form

A deconvolution operator $\hat{D}_h$ exists if the action of the convolution operator $\hat{C}_h$ on $|\rho\rangle$ i.e. $\hat{C}_h|\rho\rangle = |\bar{\rho}_h\rangle$ does not result in irreparable damage so that $|\bar{\rho}_h\rangle$ still contains enough mechanical information that the linear operator $\hat{D}_h$ can restore the original input vector $|\rho\rangle$ to give back identity i.e. $\hat{D}_h|\bar{\rho}_h\rangle = |\rho\rangle$. Figure 3.4 denotes completeness without any approximations. Expressed mathematically in operator space,

$$|\rho\rangle = \hat{D}_h\hat{C}_h|\rho\rangle \tag{3.42}$$

Furthermore, by taking an overlap with the bra vector $\langle \mathbf{r}|$ and inserting complete sets of states we obtain a statement of completeness of filtering and de-filtering processes. Then for all

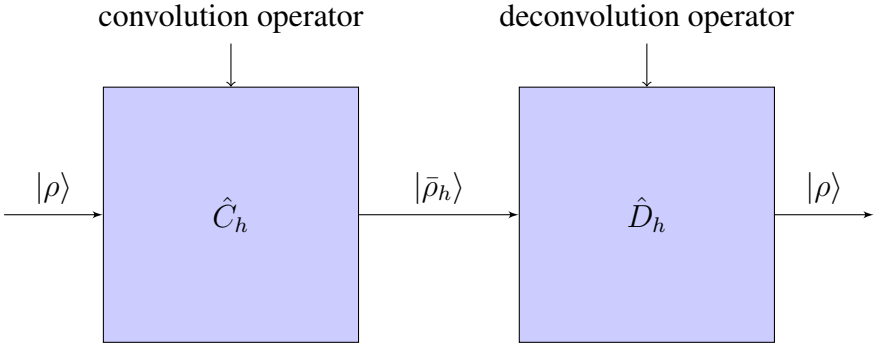

Figure 3.5: In this series representation perfect reconstruction is realized by filtering and then de-filtering.

$\mathbf{r}, \mathbf{r}', \mathbf{r}'' \in \Omega_h(\mathbf{r})$ we have

$$\begin{aligned}
\langle \mathbf{r}|\rho\rangle &= \langle \mathbf{r}|\hat{D}_h \hat{1} \hat{C}_h \hat{1}|\rho\rangle \\
&= \langle \mathbf{r}|\hat{D}_h \int_{\Omega_h(\mathbf{r})} |\mathbf{r}'\rangle\langle \mathbf{r}'|d\Omega(\mathbf{r}')\hat{C}_h \int_{\Omega_h(\mathbf{r}')} |\mathbf{r}''\rangle\langle \mathbf{r}''|d\Omega(\mathbf{r}'')|\rho\rangle \\
&= \int_{\Omega_h(\mathbf{r})} \int_{\Omega_h(\mathbf{r}')} \langle \mathbf{r}|\hat{D}_h|\mathbf{r}'\rangle\langle \mathbf{r}'|\hat{C}_h|\mathbf{r}''\rangle\langle \mathbf{r}''|\rho\rangle d\Omega(\mathbf{r}')d\Omega(\mathbf{r}'') \\
\rho(\mathbf{r}) &= \int_{\Omega_h(\mathbf{r})} \rho(\mathbf{r}'') \left(\int_{\Omega_h(\mathbf{r}')} \varphi_h(\mathbf{r}-\mathbf{r}')w_h(\mathbf{r}''-\mathbf{r}')d\Omega(\mathbf{r}') \right) d\Omega(\mathbf{r}'')
\end{aligned} \tag{3.43}$$

For perfect reconstruction of the underlying continuum field by de-filtering the filtered field, we have the following statement of completeness; for a given convolution filter $w_h \in C_c^\infty(\Omega_h)$ there exists a deconvolution filter $\varphi_h \in C_c^\infty(\Omega_h)$ such that

$$\int_{\Omega_h(\mathbf{r}')} \varphi_h(\mathbf{r}-\mathbf{r}')w_h(\mathbf{r}''-\mathbf{r}')d\Omega(\mathbf{r}') = \delta(\mathbf{r}-\mathbf{r}'') \tag{3.44}$$

Equation (3.44) represents a fundamental result of the theory which will be used in the construction of explicit, compatible convolution-deconvolution filter pairs.

Furthermore, the block diagram 3.4 can be cascaded in order to determine the effect of each operator on the input vector. This is depicted in figure 3.5.

Next, we prove that the above FIT and DIT indeed form an integral transform pair through which (perfect) reconstruction of the continuum field is achievable.

Proof. Let $\Omega_h(\mathbf{r})$ be a locally compact test space centered at the continuum point $\mathbf{r}$. Consider the continuum point $\mathbf{r}'$ with a test space $\Omega_h(\mathbf{r}')$ for all $\mathbf{r}' \in \Omega_h(\mathbf{r})$. We first compute the filtered mass density about $\mathbf{r}'$ using the FIT; for all $w_h \in C_c^\infty(\Omega_h)$ we have

$$\langle \rho_h(\mathbf{r}')\rangle = \int_{\Omega_h(\mathbf{r}')} \rho(\mathbf{r}'')w_h(\mathbf{r}'-\mathbf{r}'')d\Omega(\mathbf{r}'') \tag{3.45}$$

Then multiplying (3.45) by the deconvolution filter and integrating over the test space $\Omega_h(\mathbf{r})$

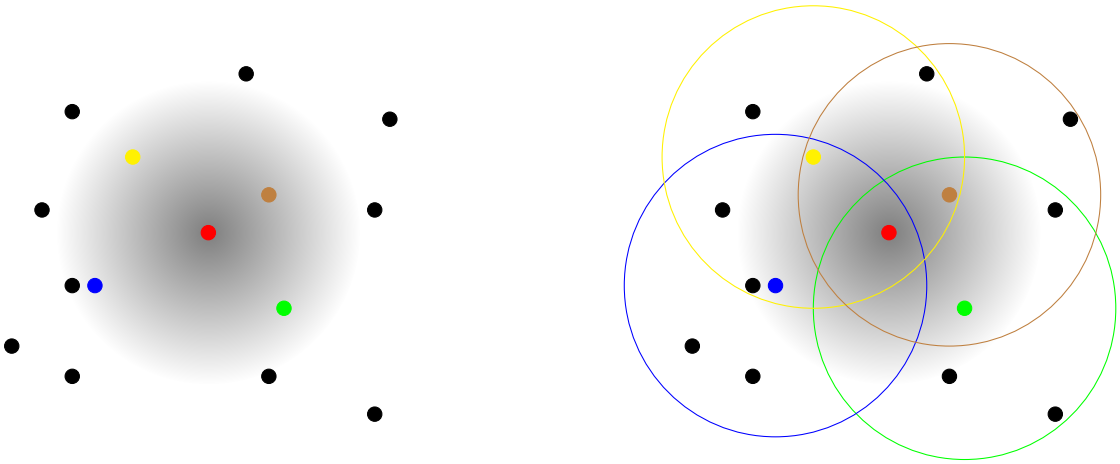

Figure 3.6: Discrete interpretation of Completeness. Left hand side: discrete FIT is a gathering process. Right hand side: discrete DIT is a scattering process. Here • is the target particle and has support particles {•, •, •, •}. All black particles • are outside the support of the target particle. The respective domain of influence of each support particle is shown by a circle of corresponding color to that particle.

yields

$$\begin{aligned}
&\int_{\Omega_h(\mathbf{r})} \langle \rho_h(\mathbf{r}') \rangle \varphi_h(\mathbf{r} - \mathbf{r}') d\Omega(\mathbf{r}') \\
&= \int_{\Omega_h(\mathbf{r})} \int_{\Omega_h(\mathbf{r}')} \rho(\mathbf{r}'') w_h(\mathbf{r}'' - \mathbf{r}') \varphi_h(\mathbf{r} - \mathbf{r}') d\Omega(\mathbf{r}'') d\Omega(\mathbf{r}') \\
&= \int_{\Omega_h(\mathbf{r})} \rho(\mathbf{r}'') \left\{ \int_{\Omega_h(\mathbf{r}')} w_h(\mathbf{r}'' - \mathbf{r}') \varphi_h(\mathbf{r} - \mathbf{r}') d\Omega(\mathbf{r}') \right\} d\Omega(\mathbf{r}'') \\
&= \int_{\Omega_h(\mathbf{r})} \rho(\mathbf{r}'') \delta(\mathbf{r} - \mathbf{r}'') d\Omega(\mathbf{r}'') \quad \text{by (3.44)} \\
&= \rho(\mathbf{r}) \qquad (3.46)
\end{aligned}$$

hence confirming the claim that the FIT of proposition 3.4.1 forms an integral transform pair with the DIT given by proposition 3.4.2.. □

We now consider the following sampling problem: Assuming that the density $\rho(\mathbf{r}_j) := \rho_j$ of each support particle is known, how do we use this information to determine the density ρ_i of the i^{th} target particle?

FIT is a "gather" process The left hand side of figure 3.6 shows the test or target particle • with support particles {•, •, •, •}. By the proof above, we first determine the local density approximation for each support particle $\langle \rho_j^h \rangle$ for all $\mathbf{r}_k \in \Omega_h(\mathbf{r}_j)$ by the FIT;

$$\langle \rho^h(\mathbf{r}_j) \rangle = \sum_{k \in \mathcal{N}(j)} \rho(\mathbf{r}_k) w_h(\mathbf{r}_j - \mathbf{r}_k) d\Omega(\mathbf{r}_k) \qquad (3.47)$$

The support particle j *gathers* contributions from all its nearest neighbors $k \in \mathcal{N}(j)$. This is a gathering process carried out on all support particles within the domain of influence $\Omega_h(\mathbf{r}_j)$ of the j^{th} support particle with $\mathbf{r}_j \in \Omega_h(\mathbf{r}_i)$.

DIT is a "scatter" process Finally, to determine the actual density of the i^{th} target particle •, we use the DIT as shown on the right hand side of figure 3.6.

$$\rho(\mathbf{r}_i) = \sum_{j \in \mathcal{N}(i)} \langle \rho^h(\mathbf{r}_j) \rangle \varphi^h(\mathbf{r}_i - \mathbf{r}_j) d\Omega(\mathbf{r}_j) \tag{3.48}$$

The target particle i collects contributions from all support particles $j \in \mathcal{N}(i)$ which the space $\Omega_h(\mathbf{r}_j)$ *scatters* onto $\Omega_h(\mathbf{r}_i) \ni \mathbf{r}_j$. Therefore, the DIT is a scattering process as shown on the right hand side of figure 3.6.

Remark 3.4.1. *The choice of volume element is worth investigating. While the approximation $d\Omega(\mathbf{r}_i) := m_i/\rho(\mathbf{r}_i)$ has been adopted in this work, it makes the method more complicated due to the implicit nature in which the de-filtered variables must be extracted from the filtered variables. An intuitive way is to use the volume element*

$$d\Omega(\mathbf{r}_i) = \frac{1}{\sqrt{\sum_{j=1} \varphi^h(\mathbf{r}_i - \mathbf{r}_j) \sum_{j=1} w^h(\mathbf{r}_i - \mathbf{r}_j)}} \tag{3.49}$$

3.5 Constructing Compatible Convolution and Deconvolution Filter on $\mathbb{R}^2$

Problem: Given a convolution filter $w_h \in C_c^\infty(\Omega_h)$ that is used to compute local approximations $\{\langle \rho_h(\mathbf{r}) \rangle, \langle p_h(\mathbf{r}) \rangle, \widetilde{\mathbf{u}}_h(\mathbf{r})\}$ from the continuum field, construct a compatible deconvolution filter $\varphi_h \in C_c^\infty(\Omega_h)$ that faithfully reconstructs the underlying continuum field $\{\rho, p, \mathbf{u}\}$ from these local approximations.

The approach to this problem was mainly motivated by pioneering work of Germano [26], Konstantopoulos et al. [27], Mary and Rice [28] and others on differential filters.

3.5.1 Translation Operator

To address the above problem, we extensively exploit the nice property of the translation (Lagrange shift) operator $\hat{T} : L^2(\mathbb{R}) \to L^2(\mathbb{R})$ which is (i) well defined (ii) linear (iii) bounded and (iv) unitary. In ν-dimensions we have;

$$\rho(\mathbf{r} - h\mathbf{r}^*) := \hat{T}(-h\mathbf{r}^*)\rho(\mathbf{r}) \equiv e^{-h\mathbf{r}^* \cdot \nabla} \rho(\mathbf{r}) \tag{3.50}$$

provided that the turbulent flow is smooth enough.

Proof. we temporarily regard $\rho(\mathbf{r} - h\mathbf{r}^*)$ as a function of s. Let

$$\begin{aligned} \Psi(s) &\overset{\text{def}}{=} \rho(\mathbf{r} - sh\mathbf{r}^*) \equiv \rho(\mathbf{v}) \quad \mathbf{v} := \mathbf{r} - sh\mathbf{r}^* \\ &= \sum_{n=0}^{\infty} \frac{s^n}{n!} \Psi^{(n)}(0) \end{aligned}$$

We thus need $\Psi(1) = \rho(\mathbf{r} - \mathbf{hr}^*)$. Now,

$$\begin{aligned}\Psi'(s) &= \frac{\partial \rho(\mathbf{v})}{\partial v^\alpha}\frac{\partial v^\alpha}{\partial s} \qquad \alpha = 1, 2, 3. \quad \text{(sum over } \alpha\text{)} \\ &= -\frac{\partial \rho(\mathbf{v})}{\partial v^\alpha} h x^*_\alpha\end{aligned}$$

Hence

$$\Psi^{(n)}(s) = (-h\mathbf{r}^* \cdot \nabla_{\mathbf{v}})\rho(\mathbf{v})^n \quad \text{giving} \quad \Psi^{(n)}(0) = (-h\mathbf{r}^* \cdot \nabla_{\mathbf{r}})^n \rho(\mathbf{r})$$

Then, for $\Psi(1)$ we obtain

$$\rho(\mathbf{r} - h\mathbf{r}^*) = \sum_{n=0}^{\infty} \frac{(-h\mathbf{r}^* \cdot \nabla_{\mathbf{r}})^n}{n!}\rho(\mathbf{r}) = e^{-h\mathbf{r}^* \cdot \nabla}\rho(\mathbf{r})$$

□

Furthermore, the aforementioned properties of the translation operator can be proved as follows;

1. $\hat{T}(-h\mathbf{r}^*)$ is linear.

   Proof. for $f, g \in L^2(\mathbb{R})$ and $\alpha, \beta \in \mathbb{R}$

   $$\begin{aligned}&\hat{T}(-h\mathbf{r}^*)[\alpha f + \beta g](\mathbf{r}) = [\alpha f + \beta g](\mathbf{r} - h\mathbf{r}^*) = \alpha f(\mathbf{r} - h\mathbf{r}^*) + \beta g(\mathbf{r} - h\mathbf{r}^*) \\ &= \alpha \hat{T}(-h\mathbf{r}^*) f(\mathbf{r}) + \beta \hat{T}(-h\mathbf{r}^*) g(\mathbf{r})\end{aligned}$$

   so $\hat{T}(-h\mathbf{r}^*)$ is a linear operator. □

2. $\hat{T}(-h\mathbf{r}^*)$ is well-defined.

   Proof. for $\rho \in L^2(\mathbb{R}^n)$

   $$\begin{aligned}\int_{\mathbb{R}^n} h^n |\hat{T}(-h\mathbf{r}^*)\rho(\mathbf{r})| d^n(\mathbf{r}^*) &= \int_{\mathbb{R}^n} h^n |\rho(\mathbf{r} - \mathbf{hr}^*)|^2 d^n(\mathbf{r}^*) \\ &= \int_{\mathbb{R}^n} |\rho(\mathbf{r}')|^2 d^n(\mathbf{r}') < \infty\end{aligned}$$

   therefore $\hat{T}(-h\mathbf{r}^*)\rho(\mathbf{r}) \in L^2(\mathbb{R})$, so $\hat{T}(-h\mathbf{r}^*)$ is well-defined. □

3. $\hat{T}(-h\mathbf{r}^*)$ is bounded.

   Proof. for $\rho \in L^2(\mathbb{R}^n)$

   $$\begin{aligned}||\hat{T}(-h\mathbf{r}^*)\rho(\mathbf{r})||^2 &= \int_{\mathbb{R}^n} h^n |\hat{T}(-h\mathbf{r}^*)\rho(\mathbf{r})|^2 d^n(\mathbf{r}^*) \\ &= \int_{\mathbb{R}^n} |\rho(\mathbf{r}')|^2 d^n(\mathbf{r}') \quad \text{by (2) above.} \\ &= ||\rho(\mathbf{r})||^2 \\ \therefore ||\hat{T}(-h\mathbf{r}^*)\rho(\mathbf{r})|| &= ||\rho(\mathbf{r})||\end{aligned}$$

   meaning that $\hat{T}(-h\mathbf{r}^*)$ is bounded (an isometry). □

3.5.2 Convolution Operator

Consider the equation (3.29) in the FIT of proposition 3.4.1. For FIT with compactly supported filters defined on $\Omega_h(\mathbf{r}) := \{\mathbf{r}, \mathbf{r}' \in \mathbb{R}^3 | \ ||\mathbf{r} - \mathbf{r}'|| \leq h, \ w_h \geq 0\}$, centered around $\mathbf{r} = (x, y, z)^{\mathrm{T}}$. The following definition can be adopted for the 3-dimensional case

$$\begin{aligned}
&\langle \rho_h(x, y, z) \rangle \\
&= \int_{-\infty}^{\infty} \int_{-\infty}^{\infty} \int_{-\infty}^{\infty} \rho(x', y', z') w_h \left(|| \left(x - x', y - y', z - z' \right) || \right) dx' dy' dz' \\
&= \int_{-\infty}^{\infty} \int_{-\infty}^{\infty} \int_{-\infty}^{\infty} \rho(x', y', z') h^{-3} w \left(\left|\left| \left(\frac{x - x'}{h}, \frac{y - y'}{h}, \frac{z - z'}{h} \right) \right|\right| \right) dx' dy' dz' \\
&= \int_{-\infty}^{\infty} \int_{-\infty}^{\infty} \int_{-\infty}^{\infty} \rho(x - hx^*, y - hy^*, z - z^*) w \left(|| \left(x^*, y^*, z^* \right) || \right) dx^* dy^* dz^* \qquad (3.51)
\end{aligned}$$

by invoking a change of variables $hx^* := x - x'$, $hy^* := y - y'$ and $hz^* := z - z'$. In compact form we then have

$$\langle \rho_h(\mathbf{r}) \rangle = \int_{\mathbb{R}^\nu} w \left(||\mathbf{r}^*|| \right) \rho(\mathbf{r} - h\mathbf{r}^*) d^\nu \mathbf{r}^* \qquad (3.52)$$

showing that convolution is commutative. Finally, combining (3.50) and (3.52) the FIT now transforms into differential form as

$$\langle \rho_h(\mathbf{r}) \rangle = \left(\int_{\mathbb{R}^\nu} w \left(||\mathbf{r}^*|| \right) \hat{T}(-h\mathbf{r}^*) d^\nu \mathbf{r}^* \right) \rho(\mathbf{r}) \equiv C_w(\hat{T}) \rho(\mathbf{r}) \qquad (3.53)$$

where we identify $C_w(\hat{T})$ as the convolution operator, which is continuous (and hence bounded) and is compact.

$$C_w(\hat{T}) \stackrel{\text{def}}{=} \int_{\mathbb{R}^\nu} w \left(||\mathbf{r}^*|| \right) \hat{T}(-h\mathbf{r}^*) d^\nu \mathbf{r}^* \qquad (3.54)$$

We shall explicitly compute $C_w(\hat{T})$ for compactly supported filters on $\Omega_h(\mathbf{r}) \in \mathbb{R}^2$ as commonly used in SPH. In particular, since the convolution filter is radially or circularly symmetric, using polar coordinates $\mathbf{r}^* := (||\mathbf{r}^*|| \cos\theta, ||\mathbf{r}^*|| \sin\theta)^{\mathrm{T}}$ with $||\mathbf{r}^*|| \in [0, 2]$ and $\theta \in [0, 2\pi]$ it is easy to show that the convolution operator becomes

$$\begin{aligned}
C_w(\hat{T}) &= \Theta_0 J_0 + \Theta_1 J_1 \frac{h^2}{2!} \Delta + \Theta_2 J_2 \frac{h^4}{4!} \Delta^2 + \Theta_3 J_3 \frac{h^6}{6!} \Delta^3 + ... \\
&= \sum_{k=0}^{\infty} \Theta_k J_k \frac{h^{2k}}{(2k)!} \nabla^{2k} \qquad (3.55)
\end{aligned}$$

Where $\Delta = \nabla^2$ is the laplacian operator and the moments of the convolution filter J_k and the angular part Θ_k are given by

$$\Theta_k = \frac{2\pi \Gamma(k + \frac{1}{2})}{\Gamma(k+1)\Gamma(\frac{1}{2})}, \quad J_k = \int_0^2 ||\mathbf{r}^*||^{2k+1} w(||\mathbf{r}^*||) d||\mathbf{r}^*||, \quad k = 0, 1, 2, 3, ... \qquad (3.56)$$

It is important to note that (3.53) is well posed if and only if $\forall k$, $|J_k| < \infty$ meaning that the convolution filter w_h must be rapidly decaying in space.

3.5.3 Deconvolution Operator

For the convolution operator given by (3.55), its associated deconvolution operator is determined from the completeness (3.44) by solving a set of inhomogeneous equations appropriate to the algebra of power series. First, we present the following version of (3.44) suitable for series algebra

Corollary 3.5.1 (Operator form of completeness statement)**.** *Let $w_h \in C_c^\infty(\Omega_h)$ be a convolution filter with associated convolution operator $C_w(\hat{T})$. Similarly, let $\varphi_h \in C_c^\infty(\Omega_h)$ be the deconvolution filter with associated deconvolution operator $D_w(\hat{T})$. Then the completeness statement (3.44) can be expressed in operator form as*

$$C_w(\hat{T})D_\varphi(\hat{T}) = 1 \Longleftrightarrow D_\varphi(\hat{T})C_w(\hat{T}) = 1 \tag{3.57}$$

Using the method of Cauchy products, for a 2D filter, it is easy to show that the deconvolution filter is given by

$$D_\varphi(\hat{T}) := \text{Inv}\{C_w(\hat{T})\} = \sum_{k=0}^{\infty} M_k \frac{h^{2k}}{(2k)!}\nabla^{2k} \tag{3.58}$$

where the coefficients $\{M_k|\ k = 0, 1, 2, 3, \dots\}$ are given by the following infinite dimensional determinant

$$M_k = (-1)^k \begin{vmatrix} \vdots & \vdots & \vdots & \vdots & \vdots & \vdots & \vdots \\ \dots & 66\Theta_1 J_1 & 1 & 0 & 0 & 0 & 0 \\ \dots & 990\Theta_2 J_2 & 45\Theta_1 J_1 & 1 & 0 & 0 & 0 \\ \dots & 616\Theta_3 J_3 & 210\Theta_2 J_2 & 28\Theta_1 J_1 & 1 & 0 & 0 \\ \dots & 990\Theta_4 J_4 & 210\Theta_3 J_3 & 70\Theta_2 J_2 & 15\Theta_1 J_1 & 1 & 0 \\ \dots & 66\Theta_5 J_5 & 45\Theta_4 J_4 & 28\Theta_3 J_3 & 15\Theta_2 J_2 & 6\Theta_1 J_1 & 1 \\ \dots & \Theta_6 J_6 & \Theta_5 J_5 & \Theta_4 J_4 & \Theta_3 J_3 & \Theta_2 J_2 & \Theta_1 J_1 \end{vmatrix} \tag{3.59}$$

and the k^{th} coefficient can be extracted from the above formula as minor determinants starting from the bottom right element, for example

$$\begin{aligned} M_1 &= (-1)^1 \left|\Theta_1 J_1\right|, \quad M_2 = (-1)^2 \begin{vmatrix} 6\Theta_1 J_1 & 1 \\ \Theta_2 J_2 & \Theta_1 J_1 \end{vmatrix}, \\ M_3 &= (-1)^3 \begin{vmatrix} 15\Theta_1 J_1 & 1 & 0 \\ 15\Theta_2 J_2 & 6\Theta_1 J_1 & 1 \\ \Theta_3 J_3 & \Theta_2 J_2 & \Theta_1 J_1 \end{vmatrix}, \dots \end{aligned} \tag{3.60}$$

However, we can directly obtain the deconvolution operator from the DIT of proposition 3.4.2, Similar to the procedure used for constructing the convolution operator above. For the DIT with compactly supported filters defined on $\Omega_h(\mathbf{r}) \in \mathbb{R}^3$, a compact space centered around $\mathbf{r} = (x, y, z)^{\mathrm{T}}$. Then given the DIT

$$\begin{aligned} \rho(\mathbf{r}) &= \int_{\mathbb{R}^\nu} \langle \rho_h(\mathbf{r}')\rangle \varphi_h(\mathbf{r} - \mathbf{r}') d^\nu \mathbf{r}' \\ &= \left(\int_{\mathbb{R}^\nu} \varphi(||\mathbf{r}^*||)\hat{T}(-h\mathbf{r}^*) d^\nu \mathbf{r}^* \right) \langle \rho_h(\mathbf{r})\rangle, \quad \text{set } h\mathbf{r}^* := \mathbf{r} - \mathbf{r}' \\ \rho(\mathbf{r}) &= D_\varphi(\hat{T})\langle \rho_h(\mathbf{r})\rangle \end{aligned} \tag{3.61}$$

where the deconvolution operator $D_\varphi(\hat{T})$ is now given by the following series.

$$D_\varphi(\hat{T}) = \sum_{k=0}^{\infty} \Theta_k L_k \frac{h^{2k}}{(2k)!} \nabla^{2k} \tag{3.62}$$

The deconvolution filter moments L_k and the angular part Θ_k are given by

$$\Theta_k = \frac{2\pi\Gamma(k+\frac{1}{2})}{\Gamma(k+1)\Gamma(\frac{1}{2})}, \quad L_k = \int_0^2 ||\mathbf{r}^*||^{2k+1} \varphi(||\mathbf{r}^*||) d||\mathbf{r}^*||, \quad k = 0, 1, 2, 3, ... \tag{3.63}$$

Again, we note that (3.61) is well posed if and only if $\forall k$, $|L_k| < \infty$ meaning that the deconvolution filter φ_h must also be rapidly decaying in space. Since the w_h and φ_h are inverse filters, it follows that (3.58) and(3.62) are equivalent, a fundamental result of this discussion and presented in the following proposition.

Proposition 3.5.1. *Let the moments of the convolution filter w_h be J_k and the convolution operator given as $C_w(\hat{T})$. Then the moment L_k of the associated deconvolution filter φ_h can be analytically determined without prior knowledge of φ_h. Mathematically,*

$$L_k = \frac{M_k}{\Theta_k} \tag{3.64}$$

3.5.4 Convolution & deconvolution operators for the Gaussian filter

Consider a special case of the Gaussian filter given by

$$w_h := \alpha h^{-\nu} e^{-||\mathbf{r}-\mathbf{r}'||^2/h^2} \tag{3.65}$$

The moments of this filter in 2D are; $J_k := \Gamma(k+1)/(2\pi)$, with the angular elements Θ_k given by (3.56). Then the associated convolution and deconvolution operator coefficients are given by

$$\Theta_k J_k = \frac{\Gamma(k+\frac{1}{2})}{\Gamma(\frac{1}{2})}, \quad M_k = (-1)^k \frac{\Gamma(k+\frac{1}{2})}{\Gamma(\frac{1}{2})} \tag{3.66}$$

$$C_w(\hat{T}) = \sum_{k=0}^{\infty} \frac{\Gamma(k+\frac{1}{2})}{\Gamma(\frac{1}{2})} \frac{h^{2k}}{(2k)!} \nabla^{2k} = \sum_{k=0}^{\infty} \frac{h^{2k}}{4^k k!} \nabla^{2k} = e^{\frac{1}{4}h^2\nabla^2} \tag{3.67}$$

$$D_\varphi(\hat{T}) = \sum_{k=0}^{\infty} (-1)^k \frac{\Gamma(k+\frac{1}{2})}{\Gamma(\frac{1}{2})} \frac{h^{2k}}{(2k)!} \nabla^{2k} = \sum_{k=0}^{\infty} (-1)^k \frac{h^{2k}}{4^k k!} \nabla^{2k} = e^{-\frac{1}{4}h^2\nabla^2} \tag{3.68}$$

which are well known operators for the Gaussian filter. [27].

3.5.5 matrix coefficients of convolution/deconvolution operators

We define the convolution filter w_h as the "matrix element" of the convolution operator $C_w(\hat{T})$.

$$\begin{aligned} w_h(\mathbf{r}-\mathbf{r}') &\triangleq \langle \mathbf{r}'|C_w(\hat{T})|\mathbf{r}\rangle \\ &= \langle \mathbf{r}'|\left(\hat{1}+\sum_{k=1}^{\infty}\Theta_k J_k \frac{h^{2k}}{(2k)!}\nabla^{2k}\right)|\mathbf{r}\rangle \\ &= \langle \mathbf{r}'|\hat{1}|\mathbf{r}\rangle + \sum_{k=1}^{\infty}\Theta_k J_k \frac{h^{2k}}{(2k)!}\langle \mathbf{r}'\nabla^{2k}|\mathbf{r}\rangle \\ \therefore w_h(\mathbf{r}-\mathbf{r}') &= \delta(\mathbf{r}-\mathbf{r}') + \sum_{k=1}^{\infty}\Theta_k J_k \frac{h^{2k}}{(2k)!}\nabla^{2k}\delta(\mathbf{r}-\mathbf{r}') \end{aligned} \tag{3.69}$$

Similarly, the deconvolution filter is defined as the "matrix element" of the deconvolution operator with respect to the continuous position basis. Following the same procedure above, the deconvolution filter takes the form

$$\begin{aligned} \varphi_h(\mathbf{r}-\mathbf{r}') &\triangleq \langle \mathbf{r}'|D_\varphi(\hat{T})|\mathbf{r}\rangle \\ \therefore \varphi_h(\mathbf{r}-\mathbf{r}') &= \delta(\mathbf{r}-\mathbf{r}') + \sum_{k=1}^{\infty}\Theta_k L_k \frac{h^{2k}}{(2k)!}\nabla^{2k}\delta(\mathbf{r}-\mathbf{r}') \end{aligned} \tag{3.70}$$

For both operators, in the continuum limit we have the flowing important property

$$\lim_{h\to 0} w_h(\mathbf{r}-\mathbf{r}') \equiv \delta(\mathbf{r}-\mathbf{r}'), \quad \lim_{h\to 0}\varphi_h(\mathbf{r}-\mathbf{r}') \equiv \delta(\mathbf{r}-\mathbf{r}') \tag{3.71}$$

3.5.6 Properties of convolution and deconvolution operators

We study the properties of convolution and deconvolution operators by investigating their action on functionals or generalized functions.

[1] The action of convolution and deconvolution operators on Dirac's delta function is to produce the convolution and deconvolution filters respectively. Mathematically,

$$C_w(\hat{T})\delta(\mathbf{r}-\mathbf{r}') = w_h(\mathbf{r}-\mathbf{r}'), \quad D_\varphi(\hat{T})\delta(\mathbf{r}-\mathbf{r}') = \varphi_h(\mathbf{r}-\mathbf{r}') \tag{3.72}$$

Proof.

$$\begin{aligned} w_h(\mathbf{r}-\mathbf{r}'') &= \int_{\mathbb{R}^\nu} w_h(\mathbf{r}-\mathbf{r}')\delta(\mathbf{r}'-\mathbf{r}'')d^\nu\mathbf{r}' \quad \text{completeness} \\ &= \int_{\mathbb{R}^\nu} w(\mathbf{r}^*)\delta(\mathbf{r}-h\mathbf{r}^*-\mathbf{r}'')d^\nu\mathbf{r}^*, \text{ change of variables} \\ &= \left(\int_{\mathbb{R}^\nu} w(\mathbf{r}^*)\hat{T}(-h\mathbf{r}^*)d^\nu\mathbf{r}^*\right)\delta(\mathbf{r}-\mathbf{r}'') \\ \therefore w_h(\mathbf{r}-\mathbf{r}'') &= C_w(\hat{T})\delta(\mathbf{r}-\mathbf{r}'') \end{aligned}$$

A similar proof for the deconvolution operator follows, hence completing the proof. □

[2] The convolution filter is the Green's function of the deconvolution operator, whereas the deconvolution filter is the Green's function of the convolution operator i.e.

$$C_w(\hat{T})\varphi_h(\mathbf{r}-\mathbf{r}'') = \delta(\mathbf{r}-\mathbf{r}''), \quad D_\varphi(\hat{T})w(\mathbf{r}-\mathbf{r}'') = \delta(\mathbf{r}-\mathbf{r}'') \tag{3.73}$$

Either of these relations is equivalent to the completeness statement (3.44). A proof of this can be directly obtained from (3.72) or directly from (3.44). Following the latter approach

Proof.

$$\begin{aligned}
\delta(\mathbf{r}-\mathbf{r}'') &= \int_{\mathbb{R}^\nu} \varphi_h(\mathbf{r}-\mathbf{r}')w_h(\mathbf{r}'-\mathbf{r}'')d^\nu\mathbf{r}' \quad \text{completeness} \\
&= \int_{\mathbb{R}^\nu} \varphi(\mathbf{r}^*)w_h(\mathbf{r}-h\mathbf{r}^*-\mathbf{r}'')d^3\mathbf{r}^*, \text{ change of variables} \\
&= \left(\int_{\mathbb{R}^\nu} \varphi(\mathbf{r}^*)\hat{T}(-h\mathbf{r}^*)d^\nu\mathbf{r}^*\right) w_h(\mathbf{r}-\mathbf{r}'') \\
\therefore \delta(\mathbf{r}-\mathbf{r}'') &= D_\varphi(\hat{T})w_h(\mathbf{r}-\mathbf{r}'')
\end{aligned}$$

For a direct proof from (3.72); we multiply by $D_\varphi(\hat{T})$ to the first equation in (3.72) to get $D_\varphi(\hat{T})C_w(\hat{T})\delta(\mathbf{r}-\mathbf{r}') = D_\varphi(\hat{T})w_h(\mathbf{r}-\mathbf{r}')$ yielding the required result since $D_\varphi(\hat{T})C_w(\hat{T}) = 1$.

A similar proof for the deconvolution operator follows, hence completing the proof. □

[3] The completeness statement (3.44) can be expressed in operator form as

$$C_w(\hat{T})D_\varphi(\hat{T}) = 1, \quad D_\varphi(\hat{T})C_w(\hat{T}) = 1 \tag{3.74}$$

Proof.

$$\begin{aligned}
C_w(\hat{T})\varphi_h(\mathbf{r}-\mathbf{r}'') &= \delta(\mathbf{r}-\mathbf{r}'') \quad \text{by (3.73) above} \\
C_w(\hat{T})D_\varphi(\hat{T})\delta(\mathbf{r}-\mathbf{r}'') &= \delta(\mathbf{r}-\mathbf{r}'') \quad \text{by (3.72) above} \\
\therefore C_w(\hat{T})D_\varphi(\hat{T}) &= 1
\end{aligned}$$

□

[4] The action of the square convolution operator on the deconvolution filter yields the deconvolution filter. Similarly, the action of the square convolution operator on the deconvolution filter yields the convolution filter.

$$C_w(\hat{T})^2\varphi_h(\mathbf{r}-\mathbf{r}'') = w_h(\mathbf{r}-\mathbf{r}''), \quad D_\varphi(\hat{T})^2w(\mathbf{r}-\mathbf{r}'') = \varphi_h(\mathbf{r}-\mathbf{r}'') \tag{3.75}$$

Proof.

$$\begin{aligned}
C_w(\hat{T})^2\varphi_h(\mathbf{r}-\mathbf{r}'') &= C_w(\hat{T})C_w(\hat{T})\varphi_h(\mathbf{r}-\mathbf{r}'') \\
&= C_w(\hat{T})\delta(\mathbf{r}-\mathbf{r}'') \quad \text{by (3.73)} \\
&= w_h(\mathbf{r}-\mathbf{r}'') \quad \text{by (3.72)}
\end{aligned}$$

A similar proof can be done for the square deconvolution operator. □

3.5.7 Cauchy product of deconvolution operator with itself

The Cauchy product is the discrete convolution of two infinite series. Since the square deconvolution operator (3.75) can be interpreted as the discrete convolution of the deconvolution operator with itself, we have,

$$\begin{aligned} D_\varphi(\hat{T})^2 &= D_\varphi(\hat{T}) \cdot D_\varphi(\hat{T}) \\ &= \left(\sum_{l=0}^{\infty} M_l \frac{h^{2l}}{(2l)!}\nabla^{2l}\right) \cdot \left(\sum_{m=0}^{\infty} M_m \frac{h^{2m}}{(2m)!}\nabla^{2m}\right) \\ \therefore D_\varphi(\hat{T})^2 &= \sum_{k=0}^{\infty} \widetilde{M}_k \frac{h^{2k}}{(2k)!}\nabla^{2k} \quad \text{where} \quad \widetilde{M}_k = \sum_{j=0}^{k} \binom{2k}{2j} M_j M_{k-j} \end{aligned} \tag{3.76}$$

Given a convolution filter w_h, it then follows from (3.75) and (3.76) that the deconvolution filter is given by the following formula.

$$\varphi_h(\mathbf{r}-\mathbf{r}'') = \sum_{k=0}^{\infty} \widetilde{M}_k \frac{h^{2k}}{(2k)!}\nabla^{2k} w_h(\mathbf{r}-\mathbf{r}'') \tag{3.77}$$

which is an exact deconvolution filter uniquely defined for each specified convolution filter with finite moments. Furthermore, the above series solution is truncated due to the fundamental limitation that computers can only handle finite collections of data. The approximate deconvolution filter, ADF then becomes

$$\varphi_{h,n}(\mathbf{r}-\mathbf{r}'') = \sum_{k=0}^{n} \widetilde{M}_k \frac{h^{2k}}{(2k)!}\nabla^{2k} w_h(\mathbf{r}-\mathbf{r}'') \equiv \sum_{k=0}^{n} f_k(h)\psi_{h,2k}(\mathbf{r}-\mathbf{r}'') \tag{3.78}$$

This series is convergent and the functions $f_k(h)$ satisfy

$$\lim_{h\to 0} \frac{f_{k+1}(h)}{f_k(h)} = \lim_{h\to 0} \frac{\widetilde{M}_{k+1}}{\widetilde{M}_k} \frac{h^{2(k+1)}}{h^{2k}} \frac{(2k)!}{(2k+2)!} \equiv 0 \tag{3.79}$$

This means that each member of the set of filters approaches zero more rapidly than the previous member as $h \to 0$. Therefore the set of basis functions $\{\psi_{h,2k} |\, k = 0, 1, 2, ...\}$ forms an asymptotic sequence in h. The difference between the true value φ_h and approximate expression $\varphi_{h,n}$ goes to zero $(\varphi_h - \varphi_{h,n})/h^n \to 0$ as $h \to 0$.

It is important to investigate how well an order-n deconvolution filter $\varphi_{h,n}$ approximates the exact deconvolution filter φ_h by comparing the moments. The exact moments of L_k of φ_h are readily computable without knowledge of the filter itself and are given by (3.64). Based on the choice of n, the moments of the approximate deconvolution filter $\varphi_{h,n}$ are given by

$$\text{exact}: \quad L_k = \frac{M_k}{\Theta_k}, \quad \text{approx}: \quad L_k^{(n)} = \int_{V_h} ||\mathbf{r}^*||^{2k+1} \varphi_n(\mathbf{r}^*) d||\mathbf{r}^*|| \tag{3.80}$$

Figure 3.7 indicates the moments of the deconvolution filter of the convolution filter given by (3.82) with $p = 5$. As can be clearly seen, the k^{th} moment L_k of an n^{th} order approximate

Moment	Approximate deconvolution filter				Exact φ_h
	$\varphi_{h,1}$	$\varphi_{h,2}$	$\varphi_{h,3}$	$\varphi_{h,4}$	
L_0	0.15915494	0.15915494	0.15915494	0.15915494	0.15915494
L_1	-0.0347461	-0.0347461	-0.0347469	-0.0347455	-0.0347461
L_2	-0.0457652*	0.015423	0.0154208	0.015424	0.0154226
L_3	-0.0492201*	0.0578682*	-0.0104030	-0.010395	-0.0103981
L_4	-0.0580177*	0.440901*	-0.13588*	0.00943111	0.00942152

Figure 3.7: The first five moments of the approximate deconvolution filter for the convolution filter given by equation (3.82) with $p = 5$. The $(*)$ indicates kernel inconsistency due to truncation.

deconvolution filter $\varphi_{h,n}$ is approximately equal to the exact moment for $k = 0, 1, ..., n$. Therefore, $\varphi_{h,n}$ approximates φ_h to degree of accuracy $2n$. Formally,

$$L_k^{(n)} \simeq L_k \quad {}^\forall k = 0, 1, 2, \dots n \tag{3.81}$$

Therefore, an n^{th} order deconvolution filter cannot reproduce all moments since $\{L_k^{(n)} \neq L_k |\ k = n+1, n+2, n+3, \dots\}$ will be inconsistent with the exact moments. However, as it will be shown below, exact deconvolution is unstable meaning that approximate filters (finite n) are more practical.

3.6 Convolution filters

A natural choice for the convolution filter in SPH is the Gaussian filter [29]. In fact Monaghan [16][30] suggests this as the first Golden Rule of SPH. All popular convolution filters are piece-wise continuous polynomials including the B-spline functions [31][30] and Wendland functions [32][33]. These filters are constructed to be Gaussian-like but they have compact support and give progressively better approximation to the Gaussian with higher filter order.

For the purposes of the work in this thesis a new set of rational convolution filters are introduced as they have better interpolatory properties than their polynomial counterparts. They are smoother and less oscillatory than polynomial filters.

$$G_{h,p} = \begin{cases} \alpha_p h^{-\nu} \left(\frac{1-\frac{1}{4h^2}||\mathbf{r}-\mathbf{r}'||^2}{1+\frac{1}{4h^2}||\mathbf{r}-\mathbf{r}'||^2} \right)^p & ||\mathbf{r}-\mathbf{r}'|| \leq 2h \\ 0 & \text{otherwise} \end{cases} \simeq \alpha_p h^{-\nu} \exp\left(-\pi \sqrt[\nu]{\alpha_p^2} \frac{||\mathbf{r}-\mathbf{r}'||^2}{h^2} \right) \tag{3.82}$$

The Weierstrass approximation theorem states that every continuous function defined on a closed interval $[\alpha, \beta]$ can be uniformly approximated as closely as desired by a polynomial function.

Theorem 3.6.1 (Weierstrass approximation theorem)**.** *Suppose $G_h : \Omega_h(\mathbf{r}) \to \mathbb{R}$ is a continuous real-valued function defined on the real, compact space $\Omega_h(\mathbf{r})$. For all $\mathbb{R} \ni \varepsilon > 0$ there exists a polynomial $w_h : \Omega_h(\mathbf{r}) \to \mathbb{R}$ such that for all $\mathbf{r}, \mathbf{r}' \in \Omega_h(\mathbf{r})$,we have,*

$$|G_h(\mathbf{r}-\mathbf{r}') - w_h(\mathbf{r}-\mathbf{r}')| < \varepsilon \quad \text{or} \quad ||G_h(\mathbf{r}-\mathbf{r}') - w_h(\mathbf{r}-\mathbf{r}')|| < \varepsilon \tag{3.83}$$

where $q := ||\mathbf{r} - \mathbf{r}'||/h \in [-2, 2]$

For the rational convolution filter (3.82) with $p = 7$, a possible approximating polynomial is given by

$$w(q) = \left(1 - \frac{q^2}{4}\right)^8 \left(2048 - 3072q^2 + 2816q^4 - 1984q^6 + 1184q^8 - 628q^{10} + 305q^{12}\right) \tag{3.84}$$

The convolution filter (3.84) is structurally suitable for constructing ADMs specified by (3.78).

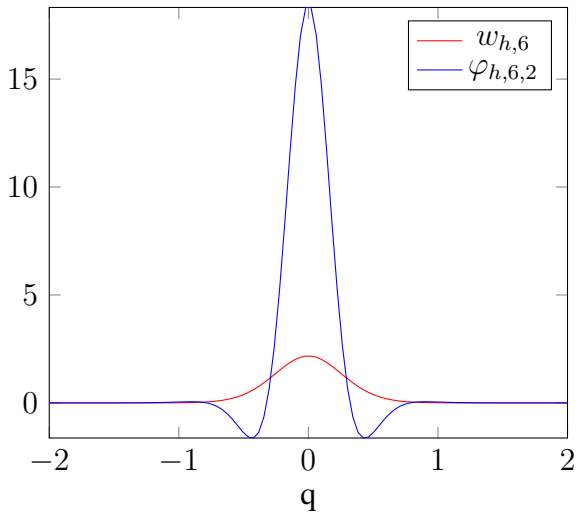

Figure 3.8: A plot of the convolution filter $w_{h,p}$ for p=6 (red) and the corresponding deconvolution filter $\varphi_{h,p,n}$ (blue) obtained by truncating the infinite sum at $n = 2$. The filter cut-off length h has been set to unity.

The smoothing length is set by applying the mass conservation law to the test space Ω_h; the total mass of fluid particles in Ω_h must be constant. For the 2D work presented in this thesis we then have that

$$M(\Omega_h) = \int_{\Omega_h(\mathbf{r})} \rho(\mathbf{r}) d^\nu(\mathbf{r}) \tag{3.85}$$

$$\simeq \rho_0 \pi (2h)^2 \tag{3.86}$$

We can introduce a new parameter ξ for the support radius of Ω_h in units of h and assuming the mass of each particle is constant, we have

$$h := \xi \Delta r \qquad \Delta r = \sqrt{\Delta x^2 + \Delta y^2} \qquad M(\Omega_h) = m N_n \tag{3.87}$$

with particle mass m, average number of particles in Ω_h is N_n the dimensions of the fluid particle are respectively Δx and Δy. Combining (3.86) and (3.87) we then have compact support radius in units of h as

$$\xi = \sqrt{\frac{N_n}{4\pi}} \tag{3.88}$$

In this work, for each problem we fix N_n and then determine the corresponding value of ξ and hence h.

3.7 Spectral Analysis

There are two factors that determine the upper limit of n; numerical stability and numerical instability due to filtering/de-filtering. Increasing n leads to improved accuracy and hence reduced numerical dissipation. Consider the Navier-Stokes equations, assuming Kolmogorov's -5/3 law, i.e. $E(k) \propto k^{-5/3}$, numerical dissipation can be approximated as a normalized coefficient

$$\begin{aligned} c_{n,\text{dissp}} &= \frac{\int_{\mathbb{R}^2} ||\mathbf{k}||^2 E(\mathbf{k}) d^2\mathbf{k} - \int_{\mathbb{R}^2} ||\mathbf{k}||^2 E(\mathbf{k}) |\hat{\varphi}_n(\mathbf{k}h)\hat{w}(\mathbf{k}h)|^2 d^2\mathbf{k}}{\int_{\mathbb{R}^2} ||\mathbf{k}||^2 E(k) d^2\mathbf{k}} \\ &= \frac{\int_0^{k_c} k^2 E(k) dk - \int_0^{k_c} k^2 E(k) |\hat{\varphi}_n(kh)\hat{w}(kh)|^2 dk}{\int_0^{k_c} k^2 E(k) dk} \end{aligned} \tag{3.89}$$

where the dimensionless cut-off wavenumber $k_c^* := k_c h = \pi$ is the cut-off wave number; the highest wavenumber that can be represented on a grid. The first term in the numerator is the exact dissipation and the second term is the restored dissipation, and thus the difference corresponds to numerical dissipation.

on the other hand, numerical instability is much more difficult to quantify. Assuming the numerical error is due to spectral truncation, the energy error is on the order of $E_e(k) \propto k^2$ at high wavenumber. We can define a normalized numerical instability coefficient as

$$\begin{aligned} c_{n,\text{instab}} &= \frac{\int_{\mathbb{R}^2} ||\mathbf{k}||^2 E_e(k) |\hat{\varphi}_n(\mathbf{k}h)\hat{w}(\mathbf{k}h)|^2 d^2\mathbf{k}}{\int_{\mathbb{R}^2} ||\mathbf{k}||^2 E(\mathbf{k}) d^2\mathbf{k}} \\ &= \frac{\int_0^{k_c} k^2 E_e(k) |\hat{\varphi}_n(kh)\hat{w}(kh)|^2 dk}{\int_0^{k_c} k^2 E_e(k) dk} \end{aligned} \tag{3.90}$$

Proposition 3.7.1. *Exact deconvolution has zero numerical dissipation.*

Proof. We first compute the Fourier transform of the completeness statement (3.44) to obtain

$$\widehat{\varphi}(k^*)\widehat{w}(k^*) = 1 \quad k^* := kh \tag{3.91}$$

$$\therefore \lim_{n\to\infty} c_{n,\text{dissp}} = 0 \quad \text{by 3.89} \tag{3.92}$$

□

Proposition 3.7.2. *Exact deconvolution is numerically unstable.*

Proof. From 3.90 we have

$$\lim_{n\to\infty} c_{n,\text{instab}} = 1 \quad \text{by 3.90} \tag{3.93}$$

□

Using Wendland's $C6$ filter as the convolution filter, by constructing its associated approximate deconvolution filter, the numerical dissipation and instability coefficients are plotted in the Fourier space as shown in figure 3.9. It can be noted that as the order of the

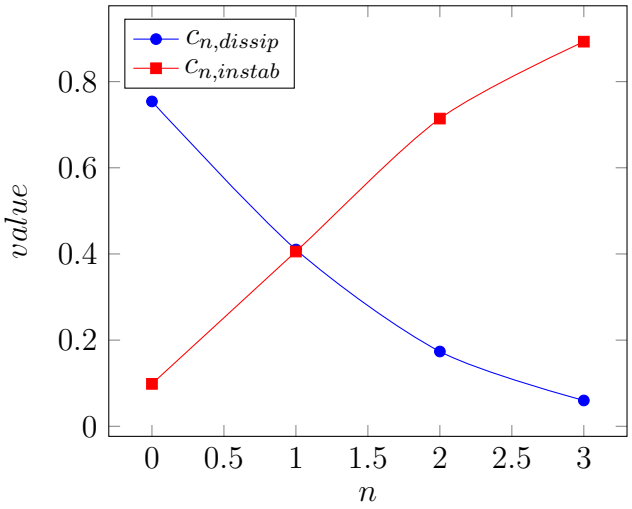

Figure 3.9: Coefficients $c_{n,dissip}$ and $c_{n,instab}$ for the deconvolution filter associated with Wendland's C5 filter. Here n correspond to the value at which the deconvolution filter φ_n is truncated.

deconvolution filter increases, numerical dissipation decreases as expected. However, with decreased numerical dissipation there is nothing to mitigate any associated numerical instabilities hence the coefficient of numerical instability is large. The hypothesis used in [34] that the energy error follows a square law i.e. $E(\mathbf{k}^*) \propto ||\mathbf{k}^*||^2$ is qualitative and not necessarily accurate. There is further room for improvement in order to obtain a more accurate estimation of numerical instability.

Figure 3.10 shows a plot of the Fourier transform of the n^{th} order deconvolution up to order $2n = 6$. Note that at zeroth order, the deconvolution filter is identical to the convolution filter i.e. $w^h \equiv \varphi_0^h$ and the Fourier transform is shown by the solid black curve in Figure 3.10. The range of wavenumbers over which the deconvolution filter has values greater than 1 increases with filter order. The implication of this characteristic shape of the deconvolution filter in Fourier space is twofold. First, the deconvolution filter is able to restore the low frequency components, consistent with its mathematical property that it becomes a Dirac delta function in the limit $h \to 0$; see equation (3.71) for a proof of this. Second, the deconvolution filter damping the high frequency components for stability reasons. It has been shown that exact deconvolution is unstable, thus approximate deconvolution which damps high frequency components is what is practically usable[34].

The next thing worth investigating is the resolution of identity given by equation (3.44). In Fourier space, we have the spectrum $\hat{\varphi}(\mathbf{k}^*)\hat{w}(\mathbf{k}^*) = 1$ for all normalized wavenumbers $\mathbf{k}^*$. For the ADM, the resolution of identity is expectedly not exact and has a spectrum given by $\hat{\varphi}_n(\mathbf{k}^*)\hat{w}(\mathbf{k}^*)$ whose plot in the Fourier space is shown in figure 3.11. It shows that the higher the order of the deconvolution filter, the larger the bandwidth of wavenumbers restored. We also see that in the limit $n \to \infty$, we have $\hat{\varphi}_n(\mathbf{k}^*)\hat{w}(\mathbf{k}^*) \to 1$ as expected from the theory presented in this chapter.

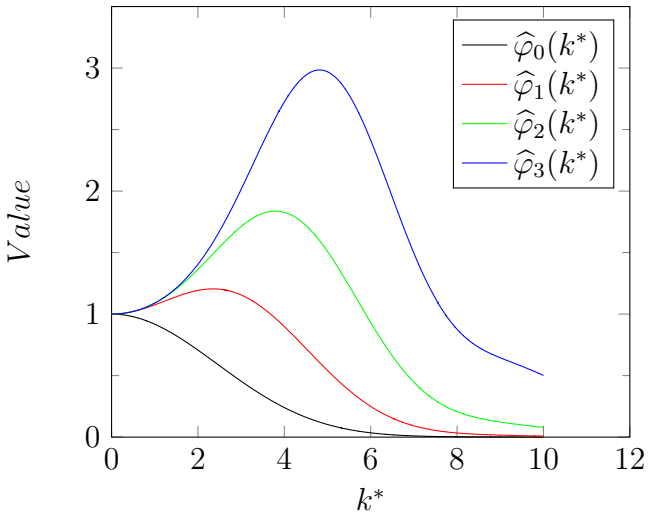

Figure 3.10: Fourier transform of the deconvolution filter $\{\widehat{\varphi}_n(k^*)|n = 0, 1, 2, 3\}$ associated with Wendland $C6$ filter in physical space with $k^* = kh$ the non-dimensional wavenumber.

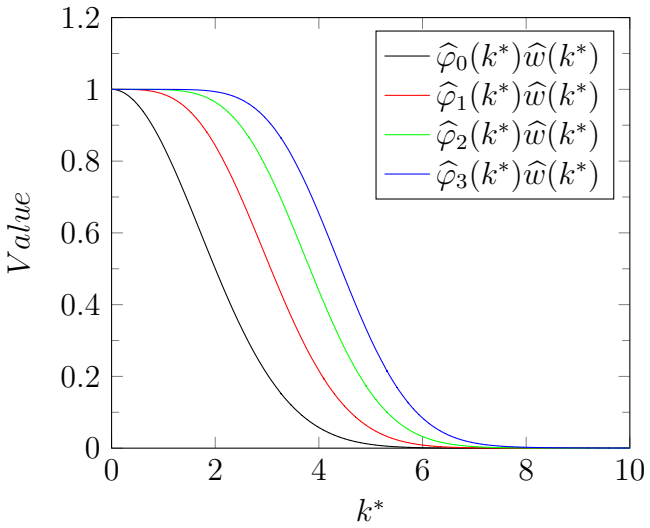

Figure 3.11: Fourier transform of the deconvolution filter $\{\widehat{\varphi}_n(k^*)\widehat{w}(k^*)|\ n = 0, 1, 2, 3\}$ associated with Wendland $C6$ filter in physical space with $k^* = kh$ the non-dimensional wavenumber.

3.8 Conclusion

In order to improve the performance and mathematical consistency of SPH, a transform pair called FIT and DIT has been proposed. A rigorous procedure for deriving convolution and deconvolution operators from the transform pair has been given. Using these operators, a method for constructing an exact, compatible and unique deconvolution filter has been proposed. Following the discussion that this exact deconvolution filter is unstable, an approximate deconvolution filter has proposed; the ideas of ADM are studied in many areas of science such as LES and image processing [35][36][37][38][39] [40] [28] [41] and convergence of ADMs [42].

Having developed a framework for constructing compatible convolution and deconvolution filters, the next two chapters deal with the application of the FIT and DIT to the CNSEs.

Chapter 4

SPH Consistent with explicit LES

Filtering problem: The goal of this chapter is to address the filtering problem: Given the continuum or disordered field$\{\rho(\mathbf{r}),\, p(\mathbf{r}),\, \mathbf{u}(\mathbf{r})\}$ defined on a domain Ω, compute local average fields $\{\langle\rho_h(\mathbf{r})\rangle,\, \langle p_h(\mathbf{r})\rangle,\, \widetilde{\mathbf{u}}_h(\mathbf{r})\}$ that faithfully represent the behavior of the disordered field on scales above some, user defined, filter length (here denoted h) and which truncates scales smaller than $\mathcal{O}(h)$.

Standard SPH is based upon the fundamental principle that any field $\Phi : \Omega_h(\mathbf{r}) \to \mathbb{R}$ can be expressed by an integral interpolant $\langle\Phi_h(\mathbf{r})\rangle := \int_{\Omega_h(\mathbf{r})} \Phi(\mathbf{r}')w_h(\mathbf{r}-\mathbf{r}')d^\nu\mathbf{r}'$. However, following the discussion from the previous section, if the particles are uniformly distributed locally and the kernel support does not intersect the domain boundaries, the local approximation becomes $\langle\Phi_h(\mathbf{r})\rangle = \Phi(\mathbf{r}) + \mathcal{O}(h^2)$ meaning SPH is second order accurate. The integral interpolant then assumes the standard form and constitutes the most fundamental principle as $\Phi(\mathbf{r}) = \int_{\Omega_h(\mathbf{r})} \Phi(\mathbf{r}')w_h(\mathbf{r}-\mathbf{r}')d^\nu\mathbf{r}' + \mathcal{O}(h^2)$. Formally, this is called zeroth order deconvolution. Unfortunately, as the particle system evolves the local particle distribution is no longer uniform, particles get disordered. Therefore, error estimation becomes a very challenging task. To address this limitation on the order of accuracy, in chapter 3 the FIT and DIT were introduced as a transform pair that will lead to the development of SPH algorithms of arbitrary accuracy.

In the following sections, we demonstrate that application of the FIT to the CNSEs leads to a version SPH that is consistent with explicit LES. The concept of local fluctuations and the relation with local uniformity of particle distribution is discussed. The chapter concludes by stressing the implications of the choice of velocity smoothing on the complexity of the mathematical structure of the smoothed CNSEs.

4.1 Application of FIT

Our choice of the filtering procedure defined by proposition 3.4.1 is to derive a set of integro-differential equations that are in principle "equivalent" to the filtered equations of explicit LES. Therefore, well established techniques such as turbulence of sub-grid stress tensors in the LES context can be applied to this version of SPH. We first prepare a useful theorem that is extensively used in the this section.

Theorem 4.1.1 (Reynolds' transport theorem)**.** *Let f:$\bar{\mathcal{D}} \times \mathcal{I} \to \mathbb{R}$ be a smooth and continuous function and $\Omega_t := \varphi(\Omega_0, t) \subseteq \mathcal{D}$, then for each $t \in \mathcal{I}$ and $\Omega_0 \subseteq \mathcal{D}$ as an arbitrary reference*

fluid domain. Then,

$$\frac{d}{dt}\int_{\Omega_t} f(\mathbf{r},t)d^n\mathbf{r} = \int_{\Omega_t}\left(\frac{d}{dt}f(\mathbf{r},t) + f(\mathbf{r},t)\nabla\cdot\mathbf{u}(\mathbf{r},t)\right)d^n\mathbf{r} \tag{4.1}$$

4.1.1 Filtered continuity equation

To obtain a consistent set of filtered CNSEs, we proceed as follows. Consider a test particle located at position $\mathbf{r}$ with a test space (domain of influence) $\Omega_h(\mathbf{r})$, a compact space. When a measurement is performed over this test space to determine the test particle's physical attributes, the measurement outcomes are the local field approximations $\{\langle\rho_h(\mathbf{r})\rangle, \langle p_h(\mathbf{r})\rangle, \widetilde{\mathbf{u}}_h(\mathbf{r})\}$ defined by the FIT of proposition 3.4.1. These are the observables or macroscopic variables that would faithfully represent the behavior of the underlying, disordered continuum fields $\{\rho(\mathbf{r}), p(\mathbf{r}), \mathbf{u}(\mathbf{r})\}$ above the filter width h consequently truncating scales smaller than $\mathcal{O}(h)$. Let the set $\{\mathcal{P}_j|\ ||\mathbf{r}-\mathbf{r}' < 2h||,\ j=1,...,N_n\}$ represent all other material elements within the test space. For this set of support material particles, the point-form of physical attributes $\{\rho(\mathbf{r}_j), p(\mathbf{r}_j), \mathbf{u}(\mathbf{r}_j)|\ j=1,...,N_n\} \in \mathrm{L}^2(\Omega_h;\mathbb{R}^n)$ are given. We then have after testing the continuity equation

$$\begin{aligned}\int_{\Omega_h(\mathbf{r})}\left(\frac{d\rho(\mathbf{r}_j)}{dt} + \rho(\mathbf{r}_j)\nabla_j\cdot\mathbf{u}(\mathbf{r}_j)\right)w_h(\mathbf{r}-\mathbf{r}_j)d\Omega(\mathbf{r}_j)\\ \overset{N_n\uparrow\infty}{\longrightarrow}\int_{\Omega_h(\mathbf{r})}\left(\frac{d\rho(\mathbf{r}')}{dt} + \rho(\mathbf{r}')\nabla'\cdot\mathbf{u}(\mathbf{r}')\right)w_h(\mathbf{r}-\mathbf{r}')d\Omega(\mathbf{r}')\end{aligned} \tag{4.2}$$

where now $\mathbf{r}' \in \Omega(\mathbf{r})$ is the position of a fluid particle in the test space. Here *weak convergence* has been assumed, provided the test space is sufficiently populated uniformly by fluid particles. Then the weak form of the continuity equation becomes

$$\int_{\Omega_h(\mathbf{r})}\left(\frac{d\rho(\mathbf{r}')}{dt} + \rho(\mathbf{r}')\nabla'\cdot\mathbf{u}(\mathbf{r}')\right)w_h(\mathbf{r}-\mathbf{r}')d\Omega(\mathbf{r}') = 0 \quad {}^{\forall}w_h \in C_0^\infty(\Omega_h) \tag{4.3}$$

which is further simplified to

$$\int_{\Omega_h(\mathbf{r})}\left\{\frac{d}{dt}\Big(\rho(\mathbf{r}')w_h\Big) + \Big(\rho(\mathbf{r}')w_h\Big)\nabla'\cdot\mathbf{u}(\mathbf{r}')\right\}d\Omega(\mathbf{r}') = \int_{\Omega_h(\mathbf{r})}\rho(\mathbf{r}')\frac{dw_h}{dt}d\Omega(\mathbf{r}') \tag{4.4}$$

Using the Reynolds transport theorem 4.1.1 it is possible to simplify (4.4) even further yielding

$$\frac{d}{dt}\int_{\Omega_h(\mathbf{r})}\rho(\mathbf{r}')w_h d\Omega(\mathbf{r}') = \int_{\Omega_h(\mathbf{r})}\rho(\mathbf{r}')\frac{dw_h}{dt}d\Omega(\mathbf{r}') \tag{4.5}$$

Since the goal is to compute the local approximations for a target particle using the disordered fields $\{\rho(\mathbf{r}), p(\mathbf{r}), \mathbf{u}(\mathbf{r})\}$, we move the target particle with the local velocity. Accordingly,

$$\text{smoothed or target particle:}\quad \frac{d\mathbf{r}}{dt} := \widetilde{\mathbf{u}}_h(\mathbf{r}) \quad \text{support particle:}\quad \frac{d\mathbf{r}'}{dt} := \mathbf{u}(\mathbf{r}') \tag{4.6}$$

The right hand side of the above equation is finally simplified with the help of the chain rule of calculus.

$$\frac{d}{dt}\int_{\Omega_h(\mathbf{r})}\rho(\mathbf{r}')w_h d\Omega(\mathbf{r}') = \int_{\Omega_h(\mathbf{r})}\rho(\mathbf{r}')\frac{dw_h}{dt}d\Omega(\mathbf{r}')$$

$$\frac{d}{dt}\int_{\Omega(\mathbf{r})}\rho(\mathbf{r}')w_h d\Omega(\mathbf{r}') = \int_{\Omega(\mathbf{r})}\rho(\mathbf{r}')\left(\frac{d\mathbf{r}}{dt}\cdot\frac{\partial w_h}{\partial \mathbf{r}} + \frac{d\mathbf{r}'}{dt}\cdot\frac{\partial w_h}{\partial \mathbf{r}'}\right)d\Omega(\mathbf{r}')$$

$$\therefore \frac{d}{dt}\langle\rho_h(\mathbf{r}\rangle = \int_{\Omega(\mathbf{r})}\rho(\mathbf{r}')\Big(\widetilde{\mathbf{u}}_h(\mathbf{r}) - \mathbf{u}(\mathbf{r}')\Big)\cdot\nabla w_h d\Omega(\mathbf{r}') \tag{4.7}$$

Equation (4.7) is the filtered form of the continuity equation in integro-differential form. Using the FIT, it is easy to prove that, when expressed in differential form, this equation reduces to the canonical form of the continuity equation (3.1) but with the unfiltered variables replaced by the filtered ones. To prove this, we unplug the space derivative ∇ from under the integral in (4.7) and using the FIT of proposition 3.4.1 as follows;

Proof. Unplugging the space derivatives from the integral in (4.7) we have,

$$\begin{aligned}\frac{d}{dt}\langle\rho_h(\mathbf{r})\rangle &= \widetilde{\mathbf{u}}_h(\mathbf{r})\cdot\nabla\int_{\Omega_h(\mathbf{r})}\rho(\mathbf{r}')w_h(\mathbf{r}-\mathbf{r}')d\Omega(\mathbf{r}')\\ &\quad -\nabla\cdot\int_{\Omega_h(\mathbf{r})}\rho(\mathbf{r}')\mathbf{u}(\mathbf{r}')w_h(\mathbf{r}-\mathbf{r}')d\Omega(\mathbf{r}')\\ &= \widetilde{\mathbf{u}}_h(\mathbf{r})\cdot\nabla\langle\rho_h(\mathbf{r})\rangle - \nabla\cdot\big(\langle\rho_h(\mathbf{r})\rangle\widetilde{\mathbf{u}}_h(\mathbf{r})\big) \quad \text{by the FIT}\\ \therefore \frac{d}{dt}\langle\rho_h(\mathbf{r})\rangle &= -\langle\rho_h(\mathbf{r})\rangle\nabla\cdot\widetilde{\mathbf{u}}_h(\mathbf{r})\end{aligned} \tag{4.8}$$

and we arrive at the filtered form of the point form of the continuum continuity equation, consistent with explicit LES. The "smoothed" material derivatives becomes

$$\frac{d}{dt} = \frac{\partial}{\partial t} + \widetilde{\mathbf{u}}_h\cdot\boldsymbol{\nabla} \tag{4.9}$$

□

Corollary 4.1.1 (filtered velocity divergence)**.** *Due to the equivalence of (4.7) and (4.8), the velocity divergence in a continuum can be calculated as an integral*

$$-\langle\rho_h(\mathbf{r})\rangle\nabla\cdot\widetilde{\mathbf{u}}_h(\mathbf{r}) = \int_{\Omega(\mathbf{r})}\rho(\mathbf{r}')\Big(\widetilde{\mathbf{u}}_h(\mathbf{r}) - \mathbf{u}(\mathbf{r}')\Big)\cdot\nabla w_h d\Omega(\mathbf{r}') \tag{4.10}$$

We emphasize that (4.10) is the most fundamental result of the filtering process. It will be used to generate integral representations of the pressure gradient and divergence of the stress tensor.

4.1.2 Filtered momentum equation

Similar to the continuity equation above, we start with the weak form

$$\int_{\Omega(\mathbf{r})}\left(\rho(\mathbf{r}')\frac{d\mathbf{u}(\mathbf{r}')}{dt} - \nabla'\cdot\underline{\underline{\tau}}(\mathbf{r}') - \rho(\mathbf{r}')\mathbf{b}(\mathbf{r}')\right)w_h d\Omega(\mathbf{r}') = 0 \quad {}^{\forall}w_h \in C_c^{\infty}(\Omega_h) \tag{4.11}$$

which may be further re-arranged as follows

$$\int_{\Omega(\mathbf{r})} \rho(\mathbf{r}')\frac{d}{dt}\Big(\mathbf{u}(\mathbf{r}')w_h\Big)d\Omega(\mathbf{r}') = \int_{\Omega(\mathbf{r})} \rho(\mathbf{r}')\mathbf{u}(\mathbf{r}')\frac{dw_h}{dt}d\Omega(\mathbf{r}') + \langle\nabla\cdot\underline{\underline{\tau}}, w_h\rangle + \langle\rho_h(\mathbf{r})\rangle\widetilde{\mathbf{b}}_h(\mathbf{r}) \tag{4.12}$$

where the FIT 3.4.1 has directly been applied to the last term on the right hand side of (4.12). Note the inner product notation for the stress term; this will be expanded shortly. The next thing is to apply the Reynolds transport theorem 4.1.1 along with the FIT to the left hand side yielding

$$\begin{aligned}
\frac{d}{dt}\int_{\Omega(\mathbf{r})} \rho(\mathbf{r}')\mathbf{u}(\mathbf{r}')w_h d\Omega(\mathbf{r}') &= \int_{\Omega(\mathbf{r})} \rho(\mathbf{r}')\mathbf{u}(\mathbf{r}')\frac{dw_h}{dt}d\Omega(\mathbf{r}') + \langle\nabla\cdot\underline{\underline{\tau}}, w_h\rangle + \langle\rho_h(\mathbf{r})\rangle\widetilde{\mathbf{b}}_h(\mathbf{r}) \\
\frac{d}{dt}\Big(\langle\rho_h(\mathbf{r})\rangle\widetilde{\mathbf{u}}_h(\mathbf{r})\Big) &= \int_{\Omega(\mathbf{r})} \rho(\mathbf{r}')\mathbf{u}(\mathbf{r}')\frac{dw_h}{dt}d\Omega(\mathbf{r}') + \langle\nabla\cdot\underline{\underline{\tau}}, w_h\rangle + \langle\rho_h(\mathbf{r})\rangle\widetilde{\mathbf{b}}_h(\mathbf{r}) \\
\langle\rho_h(\mathbf{r})\rangle\frac{d}{dt}\widetilde{\mathbf{u}}_h(\mathbf{r}) + \widetilde{\mathbf{u}}_h(\mathbf{r})\rangle\frac{d}{dt}\langle\rho_h(\mathbf{r})\rangle &= \int_{\Omega(\mathbf{r})} \rho(\mathbf{r}')\mathbf{u}(\mathbf{r}')\frac{dw_h}{dt}d\Omega(\mathbf{r}') + \langle\nabla\cdot\underline{\underline{\tau}}, w_h\rangle + \langle\rho_h(\mathbf{r})\rangle\widetilde{\mathbf{b}}_h(\mathbf{r})
\end{aligned} \tag{4.13}$$

By substituting (4.7) and applying the chain rule of calculus to the right hand side, we obtain the general form of the filtered momentum equation.

$$\begin{aligned}
\langle\rho_h(\mathbf{r})\rangle\frac{d}{dt}\widetilde{\mathbf{u}}_h(\mathbf{r}) = &-\int_{\Omega(\mathbf{r})} \rho(\mathbf{r}')\Big(\widetilde{\mathbf{u}}_h(\mathbf{r}) - \mathbf{u}(\mathbf{r}')\Big)\otimes\Big(\widetilde{\mathbf{u}}_h(\mathbf{r}) - \mathbf{u}(\mathbf{r}')\Big)\nabla w_h d\Omega(\mathbf{r}') \\
&+ \langle\nabla\cdot\underline{\underline{\tau}}, w_h\rangle + \langle\rho_h(\mathbf{r})\rangle\widetilde{\mathbf{b}}_h(\mathbf{r})
\end{aligned} \tag{4.14}$$

Definition 4.1.1 (sub-grid stress tensor,SGS)**.** *The filtered momentum equation (4.14) introduces momentum transfer due to small scale motion. This is defined by the following*

$$\begin{aligned}
\langle\underline{\underline{\mathcal{H}}}_h(\mathbf{r})\rangle &= \int_{\Omega(\mathbf{r})} \rho(\mathbf{r}')(\mathbf{u}(\mathbf{r}') - \widetilde{\mathbf{u}}_h(\mathbf{r}))\otimes(\mathbf{u}(\mathbf{r}') - \widetilde{\mathbf{u}}_h(\mathbf{r}))w_h d\Omega(\mathbf{r}') \\
&= \langle\rho_h(\mathbf{r})\rangle\Big(\widetilde{(\mathbf{u}\otimes\mathbf{u})}_h(\mathbf{r}) - \widetilde{\mathbf{u}}_h(\mathbf{r})\otimes\widetilde{\mathbf{u}}_h(\mathbf{r})\Big) \quad \textit{by the FIT}
\end{aligned} \tag{4.15}$$

which is a symmetric tensor, a property that is fundamental to the global conservation of energy. We note that the presence of the thermo-kinetic stresses in the momentum equation is purely due to the localization of the flow field by the filtering process. In Large Eddy Simulation, LES it is also called the sub-grid stress (SGS) tensor and in the context of particle methods it would be appropriately called sub-particle stress (SPS) tensor. Since the filtering operation filters out high frequency components of the flow field $\{\rho, p, \mathbf{u}\}$, the SGS tensors captures the effect of small scale motion on the mean flow $\{\langle\rho_h\rangle, \langle p_h\rangle, \widetilde{\mathbf{u}}_h\}$.

As a consequence of the FIT, the SGS tensor (4.15) has the following interesting property with respect to the action of the divergence operation on it;

$$\nabla\cdot\langle\underline{\underline{\mathcal{H}}}_h(\mathbf{r})\rangle = \int_{\Omega(\mathbf{r})} \rho(\mathbf{r}')(\mathbf{u}(\mathbf{r}') - \widetilde{\mathbf{u}}_h(\mathbf{r}))\otimes(\mathbf{u}(\mathbf{r}') - \widetilde{\mathbf{u}}_h(\mathbf{r}))\cdot\nabla w_h d\Omega(\mathbf{r}') \quad \text{by the FIT} \tag{4.16}$$

Proof.

$$
\begin{aligned}
&\int_{\Omega(\mathbf{r})} \rho(\mathbf{r}')(\mathbf{u}(\mathbf{r}') - \widetilde{\mathbf{u}}_h(\mathbf{r})) \otimes (\mathbf{u}(\mathbf{r}') - \widetilde{\mathbf{u}}_h(\mathbf{r})) \cdot \nabla w_h d\Omega(\mathbf{r}') \\
&= \nabla \cdot \int_{\Omega(\mathbf{r})} \rho(\mathbf{r}')\mathbf{u}(\mathbf{r}') \otimes \mathbf{u}(\mathbf{r}') w_h d\Omega(\mathbf{r}') - \left(\nabla \cdot \int_{\Omega(\mathbf{r})} \rho(\mathbf{r}')\mathbf{u}(\mathbf{r}') w_h d\Omega(\mathbf{r}') \right) \otimes \widetilde{\mathbf{u}}_h(\mathbf{r}) \\
&\qquad - \widetilde{\mathbf{u}}_h(\mathbf{r}) \otimes \nabla \cdot \int_{\Omega(\mathbf{r})} \rho(\mathbf{r}')\mathbf{u}(\mathbf{r}') w_h d\Omega(\mathbf{r}') + \widetilde{\mathbf{u}}_h(\mathbf{r}) \otimes \widetilde{\mathbf{u}}_h(\mathbf{r}) \cdot \nabla \int_{\Omega(\mathbf{r})} \rho(\mathbf{r}') w_h d\Omega(\mathbf{r}') \\
&= \nabla \cdot \left(\langle \rho_h \rangle \widetilde{(\mathbf{u} \otimes \mathbf{u})}_h \right) - \left(\nabla \cdot (\langle \rho_h \rangle \widetilde{\mathbf{u}}_h) \right) \otimes \widetilde{\mathbf{u}}_h - \widetilde{\mathbf{u}}_h \otimes \nabla \cdot \left(\langle \rho_h \rangle \widetilde{\mathbf{u}}_h \right) + \widetilde{\mathbf{u}}_h \otimes \widetilde{\mathbf{u}}_h \cdot \nabla \langle \rho_h \rangle \\
&= \nabla \cdot \left[\langle \rho_h \rangle \left(\widetilde{(\mathbf{u} \otimes \mathbf{u})}_h - \widetilde{\mathbf{u}}_h \otimes \widetilde{\mathbf{u}}_h \right) \right] \\
&= \nabla \cdot \langle \underline{\underline{\mathcal{H}}}_h(\mathbf{r}) \rangle \quad \text{by (4.15) above}
\end{aligned}
$$

as claimed. □

The SGS tensors are the components of a second order tensor, which is obviously symmetric. The diagonal components are normal stresses whereas the off-diagonal components are shear stresses. The density weighted turbulent kinetic energy $\widetilde{k}_h$ is defined to be half the trace of the SGS tensor and is thus

$$
\begin{aligned}
\langle \rho_h(\mathbf{r}) \rangle \widetilde{k}_h(\mathbf{r}) &:= \frac{1}{2} \operatorname{tr} \left(\langle \underline{\underline{\mathcal{H}}}_h(\mathbf{r}) \rangle \right) \\
&= \frac{1}{2} \int_{\Omega(\mathbf{r})} \rho(\mathbf{r}') ||\widetilde{\mathbf{u}}_h(\mathbf{r}) - \mathbf{u}(\mathbf{r}')||^2 w_h d\Omega(\mathbf{r}')
\end{aligned} \tag{4.17}
$$

It is the locally averaged kinetic energy per unit mass of the fluctuating velocity field.

By direct filtering of the energy conservation law (2.9), a sub-grid term called turbulent dissipation rate appears in the filtered energy balance equation. It is the rate at which turbulent kinetic energy is converted to thermal internal energy of the system. This is defined as

$$
\langle \rho_h(\mathbf{r}) \rangle \widetilde{\varepsilon}_h(\mathbf{r}) = \int_{\Omega(\mathbf{r})} \rho(\mathbf{r}') \nu \underline{\underline{\hat{\sigma}}}_h(\mathbf{r}') : \nabla' \hat{\mathbf{u}}_h(\mathbf{r}') d\Omega(\mathbf{r}') \tag{4.18}
$$

where ν^{eff} is the effective kinematic viscosity and the small-scale dissipation function is given as

$$
\nu \underline{\underline{\hat{\sigma}}}_h(\mathbf{r}) : \nabla \hat{\mathbf{u}}_h(\mathbf{r}) = - \int_{\Omega(\mathbf{r})} \nu^{\text{eff}} \left(\frac{\langle \rho_h(\mathbf{r}') \rangle}{\rho(\mathbf{r})} + \frac{\langle \rho_h(\mathbf{r}) \rangle}{\rho(\mathbf{r}')} \right) ||\widetilde{\mathbf{u}}_h(\mathbf{r}) - \mathbf{u}(\mathbf{r}')||^2 \frac{(\mathbf{r} - \mathbf{r}') \cdot \nabla \varphi_h}{||\mathbf{r} - \mathbf{r}'||^2} d\Omega(\mathbf{r}') \tag{4.19}
$$

It is important to note that the turbulent dissipation function satisfies the physical requirement that it be negative definite i.e. $\widetilde{\varepsilon}_h \leq 0$.

The integro-differential forms for the pressure (3.2) can be derived in a similar way. With brevity this derivation will be omitted. The complete filtered differential and integro-differential forms of the CNSEs can now be expressed as

$$\frac{d}{dt}\langle\rho_h(\mathbf{r})\rangle = -\langle\rho_h(\mathbf{r})\rangle\nabla\cdot\widetilde{\mathbf{u}}_h(\mathbf{r}) \tag{4.20}$$

$$\frac{d}{dt}\langle p_h(\mathbf{r})\rangle = -\langle K_S\nabla\cdot\mathbf{u}, w_h\rangle + \gamma\alpha\langle K_S\nabla\cdot(\kappa_s\nabla p), w_h\rangle \tag{4.21}$$

$$\langle\rho_h\rangle\frac{d}{dt}\widetilde{\mathbf{u}}_h = \langle\nabla\cdot\underline{\underline{\tau}}, w_h\rangle - \nabla\cdot\langle\underline{\underline{\mathcal{H}}}_h\rangle + \langle\rho_h\rangle\widetilde{\mathbf{b}}_h \tag{4.22}$$

$$\frac{d\mathbf{r}}{dt} = \widetilde{\mathbf{u}}_h(\mathbf{r}) \tag{4.23}$$

The filtered equations (4.20), (4.21), (4.22), (4.23) are not closed because the SGS tensor contains unfiltered velocities. To overcome this closure problem several models including the eddy viscosity model, Smagorinsky model and Germano dynamic model are widely used in LES.

By proper choice of the FIT, we obtain an SPH model consistent with explicit LES where the smoothed differential operators in (4.20), (4.21), (4.22) can now be expressed in integral form as;

$$\langle\rho_h(\mathbf{r})\rangle\nabla\cdot\widetilde{\mathbf{u}}_h(\mathbf{r}) = -\int_{\Omega(\mathbf{r})}\rho(\mathbf{r}')\left(\widetilde{\mathbf{u}}(\mathbf{r}) - \mathbf{u}(\mathbf{r}')\right)\cdot\nabla w_h d\Omega(\mathbf{r}') \tag{4.24}$$

$$\nabla\cdot\langle\underline{\underline{\mathcal{H}}}_h(\mathbf{r})\rangle = \int_{\Omega(\mathbf{r})}\rho(\mathbf{r}')(\mathbf{u}(\mathbf{r}') - \widetilde{\mathbf{u}}_h(\mathbf{r}))\otimes(\mathbf{u}(\mathbf{r}') - \widetilde{\mathbf{u}}_h(\mathbf{r}))\cdot\nabla w_h d\Omega(\mathbf{r}') \tag{4.25}$$

$$\langle\nabla\cdot\underline{\underline{\tau}}, w_h\rangle = \int_{\Omega(\mathbf{r})}\underline{\underline{\tau}}(\mathbf{r}')\cdot\nabla w_h d\Omega(\mathbf{r}') + \text{Surface terms or S.T.} \tag{4.26}$$

$$\nabla\cdot(\kappa_s\nabla\langle p_h\rangle) = -2\int_{\Omega(\mathbf{r})}(\kappa_s(\mathbf{r}) + \kappa_s(\mathbf{r}'))[\langle p_h(\mathbf{r})\rangle - p(\mathbf{r}')]\frac{(\mathbf{r}-\mathbf{r}')\cdot\nabla w_h}{||\mathbf{r}-\mathbf{r}'||^2}d\Omega(\mathbf{r}') + \text{S.T.} \tag{4.27}$$

Using these integral operators, one can then invoke particle discretization using the SPH quadrature: integrals are replaced by summations. Unfortunately, applying the FIT to the CNSEs introduces additional variables: the number of variables is now doubled and therefore the system is no longer closed. The most natural approach for closure is via approximate deconvolution methods (ADM) as discussed in chapter 2.

4.2 Concept of Fluctuations and Filtering Regularization

Consider the fluid domain Ω to be unbounded or that $supp(w^h)\cap\partial\Omega = \varnothing$, then the FIT of proposition 3.4.1 can be expressed as follows.

Proposition 4.2.1 (FIT on unbounded domains)**.** *Let $\Omega_h(\mathbf{r})$ be a locally compact space within the fluid domain Ω. Then the filtered mass density, momentum density and pressure*

are given by the FIT; for each $w_h \in C_c^\infty(\Omega_h)$

$$\langle \rho_h(\mathbf{r}) \rangle = \rho(\mathbf{r}) - \int_{\Omega_h(\mathbf{r})} \Big(\rho(\mathbf{r}) - \rho(\mathbf{r}') \Big) w_h(\mathbf{r} - \mathbf{r}') d\Omega(\mathbf{r}') \equiv \rho(\mathbf{r}) - \hat{\rho}_h(\mathbf{r}) \tag{4.28}$$

$$\widetilde{\mathbf{u}}_h(\mathbf{r}) = \mathbf{u}(\mathbf{r}) - \frac{1}{\langle \rho_h \rangle} \int_{\Omega_h(\mathbf{r})} \rho(\mathbf{r}') \Big(\mathbf{u}(\mathbf{r}) - \mathbf{u}(\mathbf{r}') \Big) w_h(\mathbf{r} - \mathbf{r}') d\Omega(\mathbf{r}') \equiv \mathbf{u}(\mathbf{r}) - \hat{\mathbf{u}}_h(\mathbf{r}) \tag{4.29}$$

$$\langle p_h(\mathbf{r}) \rangle = p(\mathbf{r}) - \int_{\Omega_h(\mathbf{r})} \Big(p(\mathbf{r}) - p(\mathbf{r}') \Big) w_h(\mathbf{r} - \mathbf{r}') d\Omega(\mathbf{r}') \equiv p(\mathbf{r}) - \hat{p}_h(\mathbf{r}) \tag{4.30}$$

Therefore, the FIT is an integral transform that filters out the local fluctuation field $\{\hat{\rho}_h, \hat{\mathbf{u}}_h, \hat{p}_h\}$ from the underlying disordered field $\{\rho, \mathbf{u}, p\}$ to generate a smooth field $\{\langle \rho_h \rangle, \widetilde{\mathbf{u}}_h, \langle p_h \rangle\}$. The smoothing process prevents the production of small scale flow structures due to the fluctuations $\{\hat{\rho}_h, \hat{\mathbf{u}}_h, \hat{p}_h\}$. Under the assumptions that the fluid particles are uniformly distributed locally, the fluctuations may be taken to be small. However, one has to be cautious as this is a very crude approximation. This special case is called the SPH golden rule. To prove this claim, we first prepare the following theorem.

Definition 4.2.1 (Cauchy-Schwartz inequality)**.** *Let* $\mathbf{u}$*,* $\mathbf{v}$ *be vectors in a vector space* Ω *with an inner product. The Cauchy-Schwartz inequality states that*

$$|\mathbf{u} \cdot \mathbf{v}|| \leq ||\mathbf{u}||||\mathbf{v}|| \tag{4.31}$$

Proof. Assuming that $\mathbf{v} \neq 0$, let $\lambda \in \mathbb{C}$ be given by $\lambda := \mathbf{u} \cdot \mathbf{v}/||\mathbf{v}||^2$, then

$$\begin{aligned} 0 &\leq ||\mathbf{u} + \lambda \mathbf{v}||^2 \\ &= ||\mathbf{u}||^2 - \lambda \overline{\mathbf{u} \cdot \mathbf{v}} - \overline{\lambda}(\mathbf{u} \cdot \mathbf{v}) + \overline{\lambda}\lambda ||\mathbf{v}||^2 \\ &= ||\mathbf{u}||^2 - \frac{|\mathbf{u} \cdot \mathbf{v}|^2}{||\mathbf{v}||^2} \end{aligned}$$

Therefore, $|\mathbf{u} \cdot \mathbf{v}| \leq ||\mathbf{u}||||\mathbf{v}||$. □

Definition 4.2.2 (Lipschitz continuity)**.** *Let* Ω *be the fluid domain and* $\Omega_h(\mathbf{r}) = \{\mathbf{r}, \mathbf{r}' \in \mathbb{R}^n \big| \, w_h(\mathbf{r} - \mathbf{r}') \geq 0, \, ||\mathbf{r} - \mathbf{r}'|| \leq h\}$ *the test space centered about* $\mathbf{r}$*. A mapping* $\Psi : \mathbb{R}^d \to \mathbb{R}^n$ *is Lipschitz continuous of* $\Omega_h(\mathbf{r})$ *if* $^\exists M \geq 0$ *such that* $^\forall \mathbf{r}, \mathbf{r}' \in \Omega_h(\mathbf{r}) \subset \Omega$

$$|\rho(\mathbf{r}) - \rho(\mathbf{r}')| \leq M ||\mathbf{r} - \mathbf{r}'|| \tag{4.32}$$

Proof. Define $\varphi(s) : [0, 1] \mapsto \Omega_h(\mathbf{r})$ in the following way:

$$\varphi(s) := \mathbf{r}' + (\mathbf{r} - \mathbf{r}')s$$

This function is differentiable on $(0, 1)$ and continuous on $[0, 1]$ and so is the composite function $\rho \circ \varphi$. According to the mean value theorem for a single variable function, there exists a $\xi \in [0, 1]$ such that

$$(\rho \circ \varphi)'(\xi) = (\rho \circ \varphi)(1) - (\rho \circ \varphi)(0)$$

By the chain rule of composite functions, then the following result is obtained

$$\rho(\mathbf{r}) - \rho(\mathbf{r}') = \nabla\rho(\varphi(s)) \cdot (\mathbf{r} - \mathbf{r}')$$
$$|\rho(\mathbf{r}) - \rho(\mathbf{r}')| \leq ||\nabla\rho(\varphi(s))||||\mathbf{r} - \mathbf{r}'||$$

Then $^{\forall}\mathbf{r}, \mathbf{r}' \in \Omega_h(\mathbf{r}) \subset \Omega$, since the gradient of the fluid density is bounded, it follows that $^{\exists}M \geq 0$ so that $||\nabla\rho(\varphi(s))|| \leq M$. We say that ρ is Lipschitz continuous with

$$|\rho(\mathbf{r}) - \rho(\mathbf{r}')| \leq ||\nabla\rho(\varphi(s))||||\mathbf{r} - \mathbf{r}'|| \leq M||\mathbf{r} - \mathbf{r}'||$$

□

Theorem 4.2.1 (uniform continuity)**.** *If the fluid density $\rho : \Omega_h(\mathbf{r}) \subset \Omega \to \mathbb{R}$ satisfies the Lipschitz inequality $^{\forall}\mathbf{r}, \mathbf{r}' \in \Omega_h(\mathbf{r}) \subset \Omega$, then ρ is uniformly continuous.*

Proof. $^{\exists}\varepsilon > 0$ so that for $h = \varepsilon/M$, then $^{\forall}\mathbf{r}, \mathbf{r}' \in \Omega_h(\mathbf{r}) \subset \Omega$, $||\mathbf{r} - \mathbf{r}'|| < h$ implies that

$$|\rho(\mathbf{r}) - \rho(\mathbf{r}')| \leq M||\mathbf{r} - \mathbf{r}'|| = Mh = \varepsilon$$

□

Theorem 4.2.2 (convolution regularization)**.** *The filtering of the fluid density $\rho : \Omega_h(\mathbf{r}) \subset \Omega \to \mathbb{R}$ by the convolution filter $w_h \in \mathrm{C}_c^{\infty}(\Omega)$ yields the local density approximation $\langle\rho_h\rangle : \Omega_h(\mathbf{r}) \subset \Omega \to \mathbb{R}$ as given by the FIT. Then for all $\mathbf{r} \in \Omega_h(\mathbf{r})$, in the continuum limit*

$$\lim_{h\to 0}\langle\rho_h(\mathbf{r})\rangle = \rho(\mathbf{r}) \Longleftrightarrow \lim_{h\to 0}\hat{\rho}_h(\mathbf{r})\rangle = 0 \tag{4.33}$$

uniformly.

Proof. Take h so that $\Omega_h(\mathbf{r})$:=supp$(w_h) = \{\mathbf{r}, \mathbf{r}' \in \mathbb{R}^n : ||\mathbf{r} - \mathbf{r}'|| \leq h,\ w_h \geq 0\}$. We have

$$\hat{\rho}_h(\mathbf{r}) \stackrel{\text{def}}{=} \int_{\Omega_h(\mathbf{r})} \Big(\rho(\mathbf{r}) - \rho(\mathbf{r}')\Big) w_h(\mathbf{r} - \mathbf{r}') d^n\mathbf{r}'$$
$$|\hat{\rho}_h(\mathbf{r})| = \left| \int_{\Omega_h(\mathbf{r})} \rho(\mathbf{r}) - \rho(\mathbf{r}') w_h(\mathbf{r} - \mathbf{r}') d^n\mathbf{r}' \right|$$
$$\leq \int_{\Omega_h(\mathbf{r})} |\rho(\mathbf{r}) - \rho(\mathbf{r}')| w_h(\mathbf{r} - \mathbf{r}') d^n\mathbf{r}'$$
$$\leq \text{uniform continuity}$$
$$\leq \varepsilon \int_{\Omega_h(\mathbf{r})} w_h(\mathbf{r} - \mathbf{r}') d^n\mathbf{r}'$$
$$\therefore |\hat{\rho}_h(\mathbf{r})| \leq \varepsilon$$

□

By the filtering regularization theorem 4.2.2 above, it follows that if the local distribution of fluid particles is uniformly continuous then the local density fluctuations are arbitrarily small (vanishing in the continuum limit). In the next section we discuss one application of the filtering regularization theorem as an SPH approximation rule.

4.3 SPH approximation rules

In formulating SPH, Monaghan [16] proposed a number of approximation rules which are collectively called the Golden Rules of SPH. Using these rules and the SPH quadrature, the continuous hydrodynamic conservation laws (4.20), (4.21), (4.22) and (4.23) can be collocated into discrete form; this is called particle discretization. This process transforms a continuous fluid into a discrete fluid where the fluid particles transport all the physical information such as fluid density [43].

In particular smoothed particle hydrodynamics is an example of a zeroth oder approximate deconvolution model. The zeroth order ADM implies that local fluctuations are negligibly small such that

(1) for a clearer and coherent physical interpretation, Monaghan recommends using the Gaussian as the convolution filter. With a compact support $\Omega_h(\mathbf{r})$:=supp$(w_h) \approx \{\mathbf{r}, \mathbf{r}' \in \mathbb{R}^n : ||\mathbf{r} - \mathbf{r}'|| \leq 3h\}$ the Gaussian filter decays rapidly and has been shown to be accurate compared to other filters [29]. Although long range interactions must strictly be taken into account with this filter, they are negligibly small [44].

(2) By the filtering regularization theorem 4.2.2 above, provided that h is small, the second Golden Rule of SPH states that

$$\langle \rho_h \rangle \approx \rho, \quad \langle p_h \rangle \approx p, \quad \widetilde{\mathbf{u}}_h \approx \mathbf{u} \tag{4.34}$$

with order of accuracy $\mathcal{O}(h^2)$ (see chapter 2) with the underlying assumptions that the particle distribution on $\Omega_h(\mathbf{r})$:=supp(w_h) is uniformly continuous and Ω_h does not intersect the domain boundaries. Consequently, after particle discretization, the convergence obtained does not remain as favorable. These approximations are very crude [25],[45]. Furthermore, this inaccuracy will lead to difficulties in enforcing essential boundary conditions.

(3) The local average of a product of two functions can be approximated by a product of the individual function averages. Mathematically,

$$\langle fg \rangle_h \approx \langle f_h \rangle \langle g_h \rangle \tag{4.35}$$

The immediate consequence of assumptions (4.34) and (4.35) should not be generally acceptable in multi-scale computations [43]. Under this set of assumptions, the sub-grid stress tensor given by definition (4.1.1) and the field fluctuations vanish. However, these contain mechanical information at sub-grid scale. Just like in the explicit LES approach, in this version of SPH the sub-grid stress tensor captures the effect of unresolved scales on large scale motion (mean flow). Therefore, with the above set of assumptions classical SPH would be unsuitable for simulating turbulent flows.

4.4 Choice of velocity smoothing

In recent years, Monaghan [46], [47] has pioneered the development of a turbulent model for smoothed particle hydrodynamics called SPH$-\epsilon$. Similar to Monaghan's model, Hu et.al.

[48] have recently proposed a model called SPH$-\sigma$. Due to the adopted velocity smoothing approach in both models, they are fundamentally similar to the Lagrangian Averaged Navier-Stokes, LANS-α model.

The choice of velocity smoothing is very important especially in the study of turbulence as it leads to varying mathematical structure of the filtered equations. Here a comparison of the velocity smoothing of Monaghan's SPH$-\epsilon$ with the FIT proposed in this thesis are compared.

$$\hat{\mathbf{u}}(\mathbf{r}) = \mathbf{u}(\mathbf{r}) - \epsilon \int \Big(\mathbf{u}(\mathbf{r}) - \mathbf{u}(\mathbf{r}')\Big) w_h(\mathbf{r}-\mathbf{r}')d\mathbf{r}' \tag{4.36}$$

The parameter ϵ is a constant $0 \leq \epsilon \leq 1$. It can be shown that this smoothing approach is similar to the one we propose in this paper. Consider the FIT for unbounded domains 4.2.1,

$$\widetilde{\mathbf{u}}_h = \mathbf{u}(\mathbf{r}) - \frac{1}{\langle \rho_h(\mathbf{r})\rangle} \int \rho(\mathbf{r}') \Big(\mathbf{u}(\mathbf{r}) - \mathbf{u}(\mathbf{r}')\Big) w_h(\mathbf{r}-\mathbf{r}')d\mathbf{r}' \tag{4.37}$$

which leads to the explicit Large Eddy Simulation (LES) model for compressible flows.

As a consequence of the choice of velocity smoothing, we inspect Monaghan's SPH-ϵ model in which their choice of velocity smoothing (4.36) as well as derivation from a Lagrangian leads to a scalar turbulence term in the momentum given as

$$\rho_0 \frac{d}{dt}\mathbf{u}(\mathbf{r}) = -\frac{\epsilon}{2} \int \rho(\mathbf{r}')|\mathbf{u}(\mathbf{r}) - \mathbf{u}(\mathbf{r}')|^2 \nabla w_h d\mathbf{r}' \tag{4.38}$$

which is the acceleration due to turbulence. This term only modifies the pressure and does not contribute to the shear viscosity. On the other hand the SPS tensor quantity in our model is a tensorial quantity given by definition (4.1.1). In particular, the turbulence acceleration in this case is

$$\begin{aligned} &\langle \rho_h(\mathbf{r})\rangle \frac{d}{dt}\widetilde{\mathbf{u}}_h(\mathbf{r}) \\ &\quad = -\int_{\Omega_h(\mathbf{r})} \rho(\mathbf{r}')(\mathbf{u}(\mathbf{r}) - \widetilde{\mathbf{u}}_h(\mathbf{r}')) \otimes (\mathbf{u}(\mathbf{r}) - \widetilde{\mathbf{u}}_h(\mathbf{r}')) \cdot \nabla \varphi_h d\Omega(\mathbf{r}') \end{aligned} \tag{4.39}$$

Therefore the turbulence term in our model takes into account flow directionality as it is a tensor. On the other hand, (4.38) is a scalar (possibly because it was derived from a Lagrangian) and thus cannot take flow directionality into account. Moreover, it only modifies the pressure term in the momentum equation without any contribution to the shear viscosity that is known to dominate the molecular viscosity at high Reynolds number. It can then be argued that Monaghan's model, in its present form, cannot fully account for turbulent phenomena. It is, however, clear that if the off diagonal terms in (4.39) are zero, the kernel is normalized as it should and the fluid is incompressible then the two models are again similar.

Other forms of velocity smoothing techniques are possible. Unlike the FIT procedure which appears unambiguous, the velocity smoothing can be defined in multiple other ways. It may seem more natural to define the local velocity in the same structural form as the local density and pressure such that

$$\langle \mathbf{u}_h(\mathbf{r})\rangle = \int_{\Omega_h(\mathbf{r})} \mathbf{u}_h(\mathbf{r}') w_h(\mathbf{r}-\mathbf{r}')d^n\mathbf{r}' \tag{4.40}$$

or a re-normalized form

$$\langle \mathbf{u}_h(\mathbf{r}) \rangle = \frac{\int_{\Omega_h(\mathbf{r})} \mathbf{u}_h(\mathbf{r}') w_h(\mathbf{r} - \mathbf{r}') d^n \mathbf{r}'}{\int_{\Omega_h(\mathbf{r})} w_h(\mathbf{r} - \mathbf{r}') d^n \mathbf{r}'} \tag{4.41}$$

While both definitions (4.40) and (4.40) are mathematically valid, they lack physical foundation in principle. Moreover, they both introduce mass transfer due turbulence in the continuity equation leading to a closure problem.

4.5 Conclusion

The FIT has been successfully applied to the CNSEs to derive a set of filtered equations that are consistent with explicit LES. Most importantly, the origin of the SGS tensor has been clearly demonstrated. With a consistent set of filtered equations, closure models used in LES schemes can be adopted for this version of SPH. However, the ADM discussed in this chapter 2 is a much more natural choice for closure.

The correct way of moving the target particle under the influence of support particles has also been given. Furthermore, an exact integral formula for the turbulent kinetic energy has been derived from the SGS tensor whereas the associated turbulence dissipation rate has been proposed, based on intuition and deeper understanding of the SPH concepts, without giving any rigorous treatment.

Finally, the concept of fluctuations has been introduced in this chapter. A general conclusion is that if the smoothing length h is sufficiently small and that local particle distribution remains uniform throughout the time evolution of the system, then the fluctuations are arbitrarily small and can thus be neglected. In this case the filtered field and the disordered field are approximately the same, hence no closure problem regarding the SGS tensor and other aspects of the proposed SPH model.

Chapter 5

SPH consistent with implicit LES

De-filtering problem: The problem to be addressed in the section can be formally posed as follows; Given the filtered equations governing the evolution of the local approximations $\{\langle\rho_h\rangle, \langle p_h\rangle, \widetilde{\mathbf{u}}_h\}$, de-filter these averaged equations to find the integro-differential equations governing the evolution of the underlying disordered field $\{\rho, p, \mathbf{u}\}$. The goal of this de-filtering process is to recover or restore the mechanical information at small scale that is lost during the filtering process. Consequently, any turbulent phenomena will be implicitly modeled in this approach. Therefore, the method will be referred to as SPH-i, where the i means implicit; it signifies the fact that this version of SPH is consistent with implicit LES.

5.1 De-filtering the filtered CNSE

The DIT of proposition 3.4.2 is now applied to the filtered equations to reconstruct the original flow field provided that the local approximation $\{\langle\rho_h\rangle, \langle p_h\rangle, \widetilde{\mathbf{u}}_h\}$ still contains enough mechanical information that a de-convolution filter can recover the original underlying field $\{\rho, p, \mathbf{u}\}$.

In SPH, the target particle moves with the filtered or smoothed velocity. In the context of the proposed SPH-i, the target particle moves with the de-filtered velocity. Consider a test particle located at position $\mathbf{r}$ having a test space $\Omega_h(\mathbf{r})$. Let there be a support material particle located at $\mathbf{r}'$ so that $\mathbf{r}' \in \Omega_h(\mathbf{r})$. We define the velocities on this locally compact space as

$$\text{unsmoothed or target particle:} \quad \frac{d\mathbf{r}}{dt} = \mathbf{u}(\mathbf{r}), \quad \text{support particle:} \quad \frac{d\mathbf{r}'}{dt} = \widetilde{\mathbf{u}}_h(\mathbf{r}') \tag{5.1}$$

Consider the filtered continuity equation given by (4.20). To de-filter it, we first consider the continuum point $\mathbf{r}'$ with a test space $\Omega_h(\mathbf{r}')$ for all $\mathbf{r}' \in \Omega_h(\mathbf{r})$. Using the locally averaged variables on $\Omega_h(\mathbf{r}')$, the de-filtered continuity equation is then tested with the deconvolution filter as given below.

$$\int_{\Omega_h(\mathbf{r})} \left\{ \frac{d}{dt}\langle\rho_h(\mathbf{r}')\rangle + \langle\rho_h(\mathbf{r}')\rangle\nabla'\cdot\widetilde{\mathbf{u}}_h(\mathbf{r}') \right\} \varphi_h(\mathbf{r}-\mathbf{r}')d\Omega(\mathbf{r}') = 0,$$
$$^{\forall} w_h \in C_0^\infty(\Omega_h), \quad ^{\exists}\varphi_h \in C_0^\infty(\Omega_h) \tag{5.2}$$

This can be rearranged into suitable form yielding

$$\begin{aligned}
&\int_{\Omega_h(\mathbf{r})} \left\{ \frac{d}{dt}\Big(\langle \rho_h(\mathbf{r}') \rangle \varphi_h \Big) + \Big(\langle \rho_h(\mathbf{r}') \rangle \varphi_h \Big) \nabla' \cdot \widetilde{\mathbf{u}}_h(\mathbf{r}') \right\} d\Omega(\mathbf{r}'), \\
&= \int_{\Omega_h(\mathbf{r})} \langle \rho_h(\mathbf{r}') \rangle \frac{d}{dt} \varphi_h(\mathbf{r} - \mathbf{r}') d\Omega(\mathbf{r}')
\end{aligned} \tag{5.3}$$

In this form, Reynold's Transport Theorem 4.1.1 is applied to the left hand side and the chain rule of differentiation to the right hand side. Accordingly,

$$\begin{aligned}
&\frac{d}{dt} \int_{\Omega_h(\mathbf{r})} \langle \rho_h(\mathbf{r}') \rangle \varphi_h(\mathbf{r} - \mathbf{r}') d\Omega(\mathbf{r}') \\
&\quad = \int_{\Omega_h(\mathbf{r})} \langle \rho_h(\mathbf{r}') \rangle \frac{d}{dt} \varphi_h(\mathbf{r} - \mathbf{r}') d\Omega(\mathbf{r}') \\
&\quad = \int_{\Omega_h(\mathbf{r})} \langle \rho_h(\mathbf{r}') \rangle \left\{ \frac{d\mathbf{r}}{dt} \cdot \nabla \varphi_h + \frac{d\mathbf{r}'}{dt} \cdot \nabla' \varphi_h \right\} d\Omega(\mathbf{r}') \\
&\quad = \int_{\Omega_h(\mathbf{r})} \langle \rho_h(\mathbf{r}') \rangle \left\{ \mathbf{u}(\mathbf{r}) \cdot \nabla \varphi_h + \widetilde{\mathbf{u}}_h(\mathbf{r}') \cdot \nabla' \varphi_h \right\} d\Omega(\mathbf{r}') \\
&\quad = \int_{\Omega_h(\mathbf{r})} \langle \rho_h(\mathbf{r}') \rangle \Big(\mathbf{u}(\mathbf{r}) - \widetilde{\mathbf{u}}_h(\mathbf{r}') \Big) \cdot \nabla \varphi_h d\Omega(\mathbf{r}') \\
&\frac{d}{dt} \rho(\mathbf{r}) = \int_{\Omega_h(\mathbf{r})} \langle \rho_h(\mathbf{r}') \rangle \Big(\mathbf{u}(\mathbf{r}) - \widetilde{\mathbf{u}}_h(\mathbf{r}') \Big) \cdot \nabla \varphi_h d\Omega(\mathbf{r}')
\end{aligned} \tag{5.4}$$

where the anti-symmetry property of the deconvolution gradient $\nabla' \varphi = -\nabla \varphi$ has been used to simplify the above.

Further transformation of (5.4) into differential form leads to the canonical point form of the continuum continuity equation.

Proof. We begin by unplugging the space derivatives from the integral in (5.4) and using the DIT of proposition 3.4.2 to get

$$\begin{aligned}
\frac{d}{dt} \rho(\mathbf{r}) &= \mathbf{u}(\mathbf{r}) \cdot \nabla \int_{\Omega_h(\mathbf{r})} \langle \rho_h(\mathbf{r}') \rangle \varphi_h(\mathbf{r} - \mathbf{r}') d\Omega(\mathbf{r}') \\
&\quad - \nabla \cdot \int_{\Omega_h(\mathbf{r})} \langle \rho_h(\mathbf{r}') \rangle \widetilde{\mathbf{u}}_h(\mathbf{r}') \varphi_h(\mathbf{r} - \mathbf{r}') d\Omega(\mathbf{r}') \\
&= \mathbf{u}(\mathbf{r}) \cdot \nabla \rho(\mathbf{r}) - \nabla \cdot \big(\rho(\mathbf{r}) \mathbf{u}(\mathbf{r}) \big) \quad \text{by the DIT} \\
&= -\rho(\mathbf{r}) \nabla \cdot \mathbf{u}(\mathbf{r})
\end{aligned} \tag{5.5}$$

and we recover the point form of the continuum continuity equation. Furthermore, the de-filtered material derivative becomes

$$\frac{d}{dt} = \frac{\partial}{\partial t} + \mathbf{u} \cdot \nabla \tag{5.6}$$

□

Note that (5.4) and (5.5) both represent the continuum form of the continuity equation. This equivalence immediately leads to the following corollary.

Corollary 5.1.1 (de-filtered velocity divergence)**.** *Due to the equivalence of (5.4) and (5.5), the velocity divergence in a continuum can be calculated as an integral*

$$\rho(\mathbf{r})\nabla\cdot\mathbf{u}(\mathbf{r}) = -\int_{\Omega_h(\mathbf{r})}\langle\rho_h(\mathbf{r}')\rangle\Big(\mathbf{u}(\mathbf{r})-\widetilde{\mathbf{u}}_h(\mathbf{r}')\Big)\cdot\nabla\varphi_h d\Omega(\mathbf{r}') \tag{5.7}$$

We emphasize that (5.7) is the most fundamental result of the de-filtering process. It will be used to generate integral representations of the pressure gradient and divergence of the stress tensor by the variational principle.

5.1.1 De-filtered momentum equation

De-filtering the smoothed momentum (4.22) is a bit more involving than that of the continuity equation due to the presence of sub-grid stresses. It is prudent to clearly demonstrate how the SGS tensor vanishes after the de-filtering process. Consequently, any sub-scale phenomena will be implicitly modeled- a concept that underpins the development of implicit LES models. With this understanding, the proposed SPH-i model does not require any turbulence modeling (the i in SPH-i signifies that any turbulent phenomena is implicitly captured).

First consider a fluid particle at the continuum point $\mathbf{r}'$ with a test space $\Omega_h(\mathbf{r}')$ for all $\mathbf{r}'\in\Omega_h(\mathbf{r})$. The filtered momentum equation is then tested with the deconvolution kernel

$$\begin{aligned}\int_{\Omega_h(\mathbf{r})}\Big\{&\langle\rho_h(\mathbf{r}')\rangle\frac{d}{dt}\widetilde{\mathbf{u}}_h(\mathbf{r}') - \langle\nabla'\cdot\underline{\underline{\tau}}(\mathbf{r}'),w_h\rangle + \nabla'\cdot\langle\underline{\underline{\mathcal{H}}}_h(\mathbf{r}')\rangle+\\ &\langle\rho_h(\mathbf{r}')\rangle\widetilde{\mathbf{b}}_h(\mathbf{r}')\Big\}\varphi(\mathbf{r}-\mathbf{r}')d\Omega(\mathbf{r}') = 0 \quad {}^{\forall}w_h\in C_c^\infty(\Omega_h),\ {}^{\exists}\varphi_h\in C_c^\infty(\Omega_h)\end{aligned} \tag{5.8}$$

which can be re-written as

$$\begin{aligned}\int_{\Omega_h(\mathbf{r})}\langle\rho_h(\mathbf{r}')\rangle\frac{d}{dt}\Big(\widetilde{\mathbf{u}}_h(\mathbf{r}')\varphi_h\Big)d\Omega(\mathbf{r}') &= \int_{\Omega_h(\mathbf{r})}\langle\rho_h(\mathbf{r}')\rangle\widetilde{\mathbf{u}}_h(\mathbf{r}')\frac{d\varphi_h}{dt}d\Omega(\mathbf{r}')\\ &+\int_{\Omega_h(\mathbf{r})}\nabla''\cdot\underline{\underline{\tau}}(\mathbf{r}'')\left(\int_{\Omega_h(\mathbf{r}')}w_h(\mathbf{r}''-\mathbf{r}')\varphi(\mathbf{r}-\mathbf{r}')d\Omega(\mathbf{r}')\right)d\Omega(\mathbf{r}'')\\ &-\int_{\Omega_h(\mathbf{r})}\nabla'\cdot\langle\underline{\underline{\mathcal{H}}}_h(\mathbf{r}')\rangle\varphi(\mathbf{r}-\mathbf{r}')d\Omega(\mathbf{r}')\\ &+\int_{\Omega_h(\mathbf{r})}\langle\rho_h(\mathbf{r}')\rangle\widetilde{\mathbf{b}}_h(\mathbf{r}')\varphi(\mathbf{r}-\mathbf{r}')d\Omega(\mathbf{r}')\end{aligned} \tag{5.9}$$

note use of the completeness statement 3.44 to simplify the second on the right hand side.

$$\begin{aligned}\int_{\Omega_h(\mathbf{r})}\langle\rho_h(\mathbf{r}')\rangle\frac{d}{dt}\left(\widetilde{\mathbf{u}}_h(\mathbf{r}')\varphi_h\right)d\Omega(\mathbf{r}') &= \int_{\Omega_h(\mathbf{r})}\langle\rho_h(\mathbf{r}')\rangle\widetilde{\mathbf{u}}_h(\mathbf{r}')\frac{d}{dt}\varphi_h d\Omega(\mathbf{r}') + \rho(\mathbf{r})\mathbf{b}(\mathbf{r})\\ &+\int_{\Omega_h(\mathbf{r})}\nabla''\cdot\underline{\underline{\tau}}(\mathbf{r}'')\delta(\mathbf{r}-\mathbf{r}')d\Omega(\mathbf{r}'') - \int_{\Omega_h(\mathbf{r})}\nabla'\cdot\langle\underline{\underline{\mathcal{H}}}_h(\mathbf{r}')\rangle\varphi(\mathbf{r}-\mathbf{r}')d\Omega(\mathbf{r}')\end{aligned} \tag{5.10}$$

Once again by applying the Reynold's transport theorem 4.1.1 we obtain

$$\frac{d}{dt}\int_{\Omega_h(\mathbf{r})}\langle\rho_h(\mathbf{r}')\rangle\widetilde{\mathbf{u}}_h(\mathbf{r}')\varphi_h d\Omega(\mathbf{r}') = \int_{\Omega_h(\mathbf{r})}\langle\rho_h(\mathbf{r}')\rangle\widetilde{\mathbf{u}}_h(\mathbf{r}')\frac{d}{dt}\varphi_h d\Omega(\mathbf{r}') + \nabla\cdot\underline{\underline{\tau}}(\mathbf{r}) - \int_{\Omega_h(\mathbf{r})}\nabla'\cdot\langle\underline{\underline{\mathcal{H}}}_h(\mathbf{r}')\rangle\varphi(\mathbf{r}-\mathbf{r}')d\Omega(\mathbf{r}') + \rho(\mathbf{r})\mathbf{b}(\mathbf{r}) \tag{5.11}$$

By further applying the DIT to the left hand side and the chain rule of differentiation to the first term on the right hand side the following simplified integro-differential equation is obtained.

$$\rho(\mathbf{r})\frac{d\mathbf{u}(\mathbf{r})}{dt} = -\int_{\Omega_h(\mathbf{r})}\langle\rho_h(\mathbf{r}')\rangle(\mathbf{u}(\mathbf{r})-\widetilde{\mathbf{u}}_h(\mathbf{r}'))\otimes(\mathbf{u}(\mathbf{r})-\widetilde{\mathbf{u}}_h(\mathbf{r}'))\cdot\nabla\varphi_h d\Omega(\mathbf{r}') - \int_{\Omega_h(\mathbf{r})}\nabla'\cdot\langle\underline{\underline{\mathcal{H}}}_h(\mathbf{r}')\rangle\varphi(\mathbf{r}-\mathbf{r}')d\Omega(\mathbf{r}') + \nabla\cdot\underline{\underline{\tau}}(\mathbf{r}) + \rho(\mathbf{r})\mathbf{b}(\mathbf{r}) \tag{5.12}$$

The next step is to show that the first and second terms on the right hand side of (5.12) add to zero by noting the following; By expanding the integrand in the first term and applying the DIT yields

$$\int_{\Omega_h(\mathbf{r})}\langle\rho_h(\mathbf{r}')\rangle(\mathbf{u}(\mathbf{r})-\widetilde{\mathbf{u}}_h(\mathbf{r}'))\otimes(\mathbf{u}(\mathbf{r})-\widetilde{\mathbf{u}}_h(\mathbf{r}'))\cdot\nabla\varphi_h d\Omega(\mathbf{r}') = \nabla\cdot\left(\int_{\Omega_h(\mathbf{r})}\langle\rho_h(\mathbf{r}')\rangle\widetilde{\mathbf{u}}_h(\mathbf{r}')\otimes\widetilde{\mathbf{u}}_h(\mathbf{r}')\varphi(\mathbf{r}-\mathbf{r}')d\Omega(\mathbf{r}') - \rho(\mathbf{r})\mathbf{u}(\mathbf{r})\otimes\mathbf{u}(\mathbf{r})\right) \tag{5.13}$$

Furthermore, using Gauss' theorem it easy is to show that the second term transforms to

$$\int_{\Omega_h(\mathbf{r})}\nabla'\cdot\langle\underline{\underline{\mathcal{H}}}_h(\mathbf{r}')\rangle\varphi(\mathbf{r}-\mathbf{r}')d\Omega(\mathbf{r}') = -\nabla\cdot\left(\int_{\Omega_h(\mathbf{r})}\langle\rho_h(\mathbf{r}')\rangle\widetilde{\mathbf{u}}_h(\mathbf{r}')\otimes\widetilde{\mathbf{u}}_h(\mathbf{r}')\varphi(\mathbf{r}-\mathbf{r}')d\Omega(\mathbf{r}') - \rho(\mathbf{r})\mathbf{u}(\mathbf{r})\otimes\mathbf{u}(\mathbf{r})\right) + \int_{\partial\Omega_\Gamma(\mathbf{r})}\hat{n}(\mathbf{r}')\cdot\langle\underline{\underline{\mathcal{H}}}_h(\mathbf{r}')\rangle\varphi(\mathbf{r}-\mathbf{r}')d^{\nu-1}\Gamma(\mathbf{r}') \tag{5.14}$$

where $\partial\Omega_\Gamma(\mathbf{r})$ is the surface that bounds the test space $\Omega_h(\mathbf{r})$. Therefore, plugging (5.13) and (5.14) into (5.12)

$$\rho(\mathbf{r})\frac{d\mathbf{u}(\mathbf{r})}{dt} = \nabla\cdot\underline{\underline{\tau}}(\mathbf{r}) + \rho(\mathbf{r})\mathbf{b}(\mathbf{r}) + \int_{\partial\Omega_\Gamma(\mathbf{r})}\hat{n}(\mathbf{r}')\cdot\langle\underline{\underline{\mathcal{H}}}_h(\mathbf{r}')\rangle\varphi(\mathbf{r}-\mathbf{r}')d^{\nu-1}\Gamma(\mathbf{r}') \tag{5.15}$$

In particular if the fluid domain Ω is bounded by the surface $\partial\Omega$, then provided that $\partial\Omega_\Gamma(\mathbf{r})\cap\partial\Omega = \varnothing$, then the surface integral above is identically zero since $\varphi = 0$ on $\partial\Omega_\Gamma(\mathbf{r})$ by construct. Close to the boundary this assumption does not hold and the surface integral must be taken into account.

5.1.2 Momentum Conserving DIT for the Stress Tensor

Linear momentum conservation is fundamental to the long term stability of numerical algorithms. The SPH-i model is non-conserving, but momentum conserving integral operators can be constructed by sacrificing energy conservation. The energy will only be conserved in an approximate sense. Here we construct momentum conserving integral operators for the stress tensor. For a general and rigorous approach for dissipative systems, the reader is referred to [49].

For a continuum of fluid contained within the domain Ω, we can define the total energy of the hydrodynamic system as

$$E = \int_{\Omega} \left(\frac{1}{2} ||\mathbf{u}||^2 + u \right) \rho d\Omega \tag{5.16}$$

where u is the specific internal energy of the system.

With the help of the Reynolds transport theorem, the rate of change of the total energy is given as

$$\begin{aligned} \frac{d}{dt}E &= \int_{\Omega} \left(\rho \frac{d\mathbf{u}}{dt} \cdot \mathbf{u} + \rho \frac{du}{dt} \right) d\Omega \\ &= \int_{\Omega} \left(\nabla p \cdot \mathbf{u} - p \nabla \cdot \mathbf{u} \right) d\Omega \end{aligned} \tag{5.17}$$

If we now substitute for $\nabla \cdot \mathbf{u}$ from (5.7), and with further simplifications we obtain

$$\frac{d}{dt}E = \int_{\Omega} \left(\nabla p \cdot \mathbf{u} - \frac{p}{\rho} \int_{\Omega_h(\mathbf{r})} \langle \rho_h(\mathbf{r}') \rangle \left(\mathbf{u}(\mathbf{r}) - \widetilde{\mathbf{u}}_h(\mathbf{r}') \right) \cdot \nabla \varphi_h d\Omega(\mathbf{r}') \right) d\Omega \tag{5.18}$$

Using the FIT on unbounded domains of proposition 4.2.1, we can simplify (5.18) as

$$\begin{aligned} \frac{d}{dt}E = &\int_{\Omega} \left(\nabla p - \int_{\Omega_h(\mathbf{r})} \left(\frac{p(\mathbf{r})}{\rho(\mathbf{r})} \langle \rho_h(\mathbf{r}') \rangle + \frac{p(\mathbf{r}')}{\rho(\mathbf{r}')} \langle \rho_h(\mathbf{r}) \rangle \right) \nabla \varphi_h d\Omega(\mathbf{r}') \cdot \mathbf{u}(\mathbf{r}) \right) d\Omega \\ &+ \int_{\Omega} \frac{p(\mathbf{r})}{\rho(\mathbf{r})} \nabla \cdot \int_{\Omega_h(\mathbf{r})} \langle \rho_h(\mathbf{r}') \rangle \hat{\mathbf{u}}_h(\mathbf{r}') \varphi_h d\Omega(\mathbf{r}') d\Omega \end{aligned} \tag{5.19}$$

If we make an assumption that momentum transfer due to turbulent fluctuations is negligible, then the second term in (5.19) can be neglected. Therefore, energy is conserved under such conditions. Consequently, as the fluid domain Ω is arbitrary, we have

$$G(p|\varphi) = \nabla p = \int_{\Omega_h(\mathbf{r})} \left(\frac{p(\mathbf{r})}{\rho(\mathbf{r})} \langle \rho_h(\mathbf{r}') \rangle + \frac{p(\mathbf{r}')}{\rho(\mathbf{r}')} \langle \rho_h(\mathbf{r}) \rangle \right) \nabla \varphi_h d\Omega(\mathbf{r}') \tag{5.20}$$

The de-filtering integral transform for the pressure gradient $G(p|\varphi)$ is clearly anti-symmetric, thus momentum conserving, and is variationally consistent with the integral transform for the velocity divergence $D(\mathbf{u}|\varphi)$ defined below.

$$D(\mathbf{u}|\varphi) = \nabla \cdot \mathbf{u}(\mathbf{r}) = -\frac{1}{\rho(\mathbf{r})} \int_{\Omega_h(\mathbf{r})} \langle \rho_h(\mathbf{r}') \rangle \left(\mathbf{u}(\mathbf{r}) - \widetilde{\mathbf{u}}_h(\mathbf{r}') \right) \cdot \nabla \varphi_h d\Omega(\mathbf{r}') \tag{5.21}$$

Similar momentum conserving de-filtering integral transforms for the divergence of the deviatoric stress tensor $D(\mu, \underline{\underline{\sigma}}|\varphi)$ and the Laplacian of the pressure $L(\kappa^s, p|\varphi)$ can be constructed. With brevity this procedure is omitted but the result is given below.

$$\begin{aligned} D(\mu, \underline{\underline{\sigma}}|\varphi) &:= \nabla \cdot \underline{\underline{\sigma}} \\ &= \int_{\Omega_h(\mathbf{r})} \left(\frac{\underline{\underline{\sigma}}(\mathbf{r})}{\rho(\mathbf{r})} \langle \rho_h(\mathbf{r}') \rangle + \frac{\underline{\underline{\sigma}}(\mathbf{r}')}{\rho(\mathbf{r}')} \langle \rho_h(\mathbf{r}) \rangle \right) \cdot \nabla \varphi_h d\Omega(\mathbf{r}') \end{aligned} \tag{5.22}$$

$$\begin{aligned} L(\kappa^s, p|\varphi) &:= \nabla \cdot (\kappa^s \nabla p) \\ &= \frac{1}{2} \int_{\Omega_h(\mathbf{r})} \left[\left(\langle \kappa_h^s(\mathbf{r}) + \langle \kappa_h^s(\mathbf{r}') \right) \left(p(\mathbf{r}) - p(\mathbf{r}') \right) \right. \\ &+ \left. \left(\kappa^s(\mathbf{r}) + \kappa^s(\mathbf{r}') \right) \left(\langle p_h(\mathbf{r}) \rangle - \langle p_h(\mathbf{r}') \rangle \right) \right] \frac{(\mathbf{r} - \mathbf{r}') \cdot \nabla \varphi_h}{||\mathbf{r} - \mathbf{r}'||^2} d\Omega(\mathbf{r}') \end{aligned} \tag{5.23}$$

5.2 De-filtered SPH Model

The de-filtered SPH, SPH-i, model is a complete model resulting from the application of the DIT to the filtered CNSEs. Unlike the SPH which uses the zeroth order deconvolution method, SPH-i is based on the general deconvolution method. The mathematical procedure is shown below; steps [1]$\sim$[3] is the convolution operation on the fields $\{\rho, p, \mathbf{u}\}$ to produce local approximations $\{\langle \rho_h \rangle, \langle p_h \rangle, \widetilde{\mathbf{u}}_h\}$. For completeness, in steps [4]$\sim$[6] a deconvolution operation is dynamically performed on the local approximations to reconstruct the original continuum field $\{\rho, p, \mathbf{u}\}$. We also use the de-filtering integral operators (5.20), (5.21)and (5.23)

[1] smoothed mass density

$$\begin{aligned} \langle \rho_h(\mathbf{r}) \rangle &= \int_{\Omega_h(\mathbf{r})} \rho(\mathbf{r}') w_h(\mathbf{r} - \mathbf{r}') d\Omega(\mathbf{r}') \\ &\doteq \rho(\mathbf{r}) - \int_{\Omega_h(\mathbf{r})} \Big(\rho(\mathbf{r}) - \rho(\mathbf{r}') \Big) w_h(\mathbf{r} - \mathbf{r}') d\Omega(\mathbf{r}') \end{aligned} \tag{5.24}$$

[2] smoothed pressure

$$\langle p_h(\mathbf{r}) \rangle = \int_{\Omega_h(\mathbf{r})} p(\mathbf{r}') w_h(\mathbf{r} - \mathbf{r}') d\Omega(\mathbf{r}') \tag{5.25}$$

$$\doteq p(\mathbf{r}) - \int_{\Omega_h(\mathbf{r})} \Big(p(\mathbf{r}) - p(\mathbf{r}') \Big) w_h(\mathbf{r} - \mathbf{r}') d\Omega(\mathbf{r}') \tag{5.26}$$

[3] smoothed velocity

$$\widetilde{\mathbf{u}}_h(\mathbf{r}) = \frac{1}{\langle \rho_h(\mathbf{r}) \rangle} \int_{\Omega_h(\mathbf{r})} \rho(\mathbf{r}') \mathbf{u}(\mathbf{r}') w_h(\mathbf{r} - \mathbf{r}') d\Omega(\mathbf{r}') \tag{5.27}$$

$$\doteq \mathbf{u}(\mathbf{r}) - \frac{1}{\langle \rho_h(\mathbf{r}) \rangle} \int_{\Omega_h(\mathbf{r})} \rho(\mathbf{r}') \Big(\mathbf{u}(\mathbf{r}) - \mathbf{u}(\mathbf{r}') \Big) w_h(\mathbf{r} - \mathbf{r}') d\Omega(\mathbf{r}') \tag{5.28}$$

[4] de-filtered continuity equation

$$\frac{d\rho}{dt} = -\rho D(\mathbf{u}|\varphi) \tag{5.29}$$

[5] de-filtered pressure equation

$$\begin{aligned}\kappa_s(p)\frac{dp}{dt} = &-D(\mathbf{u}|\varphi) \\ &+ \gamma\alpha L(\kappa_s(p), p|\varphi) - \alpha L\left(\frac{1}{\rho}, \rho|\varphi\right)\end{aligned} \tag{5.30}$$

[6] de-filtered momentum equation

$$\rho\frac{d\mathbf{u}}{dt} = -G(p|\varphi) + D(\mu, \underline{\underline{\sigma}}|\varphi) + G\left(\underline{\underline{\sigma}}|\varphi\right) + \rho\mathbf{b} \tag{5.31}$$

[7] moving the particles

$$\frac{d\mathbf{r}}{dt} = \mathbf{u}(\mathbf{r}) \tag{5.32}$$

To get the discrete forms we just replace integrals by summations. The reader must also see that the differential forms of the above are the original compressible Navier-Stokes equations.

The predictor-corrector integration proposed by Monaghan [50] is adopted. This scheme is implemented as follows;

(1) prediction step

$$\begin{aligned}
\langle\rho_i^h\rangle^{n+1/2} &= \rho_i^n - \frac{\Delta t}{2}\rho_i^n D_i(\mathbf{u}^n, \widetilde{\mathbf{u}}_h^n, \langle\rho_h\rangle^n, \rho^n|\varphi^n) - \hat{\rho}_i(\rho^n|w^n) \\
\langle p_i^h\rangle^{n+1/2} &= p_i^n + \frac{\Delta t}{2}\Big(- K_i^s D_i(\mathbf{u}^n, \widetilde{\mathbf{u}}_h^n, \langle\rho_h\rangle^n, \rho^n|\varphi^n) \\
&\qquad + K_i^s\gamma\alpha L_i(\kappa_s^n, \langle p_h\rangle^n, p^n|\varphi^n) - \alpha K_i^s L_i\left(\langle\rho_n\rangle^n, \rho|\varphi^n\right)\Big) \\
&\qquad - \hat{p}_i(p^n|w^n) \\
\widetilde{\mathbf{u}}_i^{h,n+1/2} &= \mathbf{u}_i^n + \frac{\Delta t}{2}\Big(- \frac{1}{\rho^n}G_i(p^n, \langle\rho_i\rangle^n, \rho^n|\varphi^n) + \frac{1}{\rho^n}D_i(\underline{\underline{\sigma}}^n, \langle\rho_h\rangle^n, \rho^n|\varphi^n) + \boldsymbol{g}\Big) \\
&\qquad - \hat{\mathbf{u}}_i(\mathbf{u}^n|w^n) \\
\rho_i^{n+1/2} &= \rho_i^n - \frac{\Delta t}{2}\rho_i^n D_i(\mathbf{u}^n, \widetilde{\mathbf{u}}_h^n, \langle\rho_h\rangle^n, \rho^n|\varphi^n) \\
p_i^{n+1/2} &= p_i^n + \frac{\Delta t}{2}\Big(- K_i^s D_i(\mathbf{u}^n, \widetilde{\mathbf{u}}_h^n, \langle\rho_h\rangle^n, \rho^n|\varphi^n) \\
&\qquad + K_i^s\gamma\alpha L_i(\kappa_s^n, \langle p_h\rangle^n, p^n|\varphi^n) - \alpha K_i^s L_i\left(\langle\rho_n\rangle^n, \rho|\varphi^n\right)\Big) \\
\mathbf{u}_i^{n+1/2} &= \mathbf{u}_i^n + \frac{\Delta t}{2}\Big(- \frac{1}{\rho^n}G_i(p^n, \langle\rho_i\rangle^n, \rho^n|\varphi^n) + \frac{1}{\rho^n}D_i(\underline{\underline{\sigma}}^n, \langle\rho_h\rangle^n, \rho^n|\varphi^n) + \boldsymbol{g}\Big)
\end{aligned} \tag{5.33}$$

(2) correction step

$$
\begin{aligned}
\langle \rho_i^h \rangle^{n+1/2} &= \rho_i^n - \frac{\Delta t}{2} \rho_i^{n+1/2} D_i(\mathbf{u}^{n+1/2}, \widetilde{\mathbf{u}}_h^{n+1/2}, \langle \rho_h \rangle^{n+1/2}, \rho^{n+1/2} | \varphi^{n+1/2}) \\
&\quad - \hat{\rho}_i(\rho^{n+1/2} | w^{n+1/2}) \\
\langle p_i^h \rangle^{n+1/2} &= p_i^n + \frac{\Delta t}{2} \Big(- K_i^{s,n+1/2} D_i(\mathbf{u}^{n+1/2}, \widetilde{\mathbf{u}}_h^{n+1/2}, \langle \rho_h \rangle^{n+1/2}, \rho^{n+1/2} | \varphi^{n+1/2}) \\
&\quad + \gamma \alpha K_i^{s,n+1/2} L_i(\kappa_s^{n+1/2}, \langle p_h \rangle^{n+1/2}, p^{n+1/2} | \varphi^{n+1/2}) \\
&\quad - \alpha K_i^s L_i \left(\langle \rho_{n+1/2} \rangle^{n+1/2}, \rho | \varphi^{n+1/2} \right) \Big) - \hat{p}_i(\rho^{n+1/2}, p^{n+1/2} | w^{n+1/2}) \\
\widetilde{\mathbf{u}}_i^{h,n+1/2} &= \mathbf{u}_i^n + \frac{\Delta t}{2} \Big(- \frac{1}{\rho^{n+1/2}} G_i(p^{n+1/2}, \langle \rho_i \rangle^{n+1/2}, \rho^{n+1/2} | \varphi^{n+1/2}) \\
&\quad + \frac{1}{\rho^{n+1/2}} D_i(\underline{\underline{\sigma}}^{n+1/2}, \langle \rho_h \rangle^{n+1/2}, \rho^{n+1/2} | \varphi^{n+1/2}) + \boldsymbol{g} \Big) \\
&\quad - \hat{\mathbf{u}}_i(\mathbf{u}^{n+1/2}, \langle \rho_h \rangle^{n+1/2} | w^{n+1/2}) \\
\rho_i^{n+1/2} &= \rho_i^n - \frac{\Delta t}{2} \rho_i^{n+1/2} D_i(\mathbf{u}^n, \widetilde{\mathbf{u}}_h^n, \langle \rho_h \rangle^{n+1/2}, \rho^{n+1/2} | \varphi^{n+1/2}) \\
p_i^{n+1/2} &= p_i^n + \frac{\Delta t}{2} \Big(- K_i^{s,n+1/2} D_i(\mathbf{u}^{n+1/2}, \widetilde{\mathbf{u}}_h^{n+1/2}, \langle \rho_h \rangle^{n+1/2}, \rho^{n+1/2} | \varphi^{n+1/2}) \\
&\quad + \gamma \alpha K_i^{s,n+1/2} L_i(\kappa_s^{n+1/2}, \langle p_h \rangle^{n+1/2}, p^{n+1/2} | \varphi^{n+1/2}) \\
&\quad - \alpha K_i^{s,n+1/2} L_i \left(\langle \rho_{n+1/2} \rangle^{n+1/2}, \rho | \varphi^{n+1/2} \right) \Big) \\
\mathbf{u}_i^{n+1/2} &= \mathbf{u}_i^n + \frac{\Delta t}{2} \Big(- \frac{1}{\rho^{n+1/2}} G_i(p^{n+1/2}, \langle \rho \rangle^{n+1/2}, \rho^{n+1/2} | \varphi^{n+1/2}) \\
&\quad + \frac{1}{\rho^{n+1/2}} D_i(\underline{\underline{\sigma}}^{n+1/2}, \langle \rho_h \rangle^{n+1/2}, \rho^{n+1/2} | \varphi^{n+1/2}) + \boldsymbol{g} \Big) \\
\mathbf{r}_i^{n+1/2} &= \mathbf{r}_i^n + \Delta t \mathbf{u}^{n+1/2}
\end{aligned}
\tag{5.34}
$$

(3) finally, the values are calculated at the end of the time step following:

$$
\begin{aligned}
\langle \rho_h \rangle_i^{n+1} &= 2\rho_i^{n+1/2} - \rho_i^n - \hat{\rho}_i^{n+1} \\
\langle p_h \rangle_i^{n+1} &= 2p_i^{n+1/2} - p_i^n - \hat{p}_i^{n+1} \\
\widetilde{\mathbf{u}}_i^{n+1} &= 2\mathbf{u}_i^{n+1/2} - \mathbf{u}_i^n - \hat{\mathbf{u}}_i^{n+1} \\
\rho_i^{n+1} &= 2\rho_i^{n+1/2} - \rho_i^n \\
p_i^{n+1} &= 2p_i^{n+1/2} - p_i^n \\
\mathbf{u}_i^{n+1} &= 2\mathbf{u}_i^{n+1/2} - \mathbf{u}_i^n \\
\mathbf{r}_i^{n+1} &= \mathbf{r}_i^n + \Delta t \mathbf{u}^{n+1/2}
\end{aligned}
\tag{5.35}
$$

Based on this scheme, an in-house 2D code was developed from the scratch initially in Fortran and subsequently in the C environment. The code later partially parallelized using

openMP multi-threading. An open source package called *libnabo* was used for neighbor search. it is a fast K Nearest Neighbor (KNN) library based on kd-tree. However, as the code is not fully parallel, a simulation time of $10s$ with say 45,000 particles would run for 21 hours on a 4 nodes of the HPC cluster in our university. Note also that compared to standard SPH, the computational cost for our SPH-i algorithm is twice greater since processes are involved; filtering and de-filtering.

5.3 Conclusion

In this paper a new method called de-filtered smoothed particle hydrodynamics SPH-i has been proposed as a complete form of Smoothed Particle Hydrodynamics. Outlined below are the fundamental differences between the two methods.

(1) Resolution of identity.
This is the main objective of both methods. It has been shown that SPH is incomplete as it uses the convolution operator to approximate identity with equality only achieved in the continuum limit; this is practically impossible. On the other hand, SPH-i uses two commuting operators that are inverse operators to exactly resolve identity. In this sense SPH-i is complete.

(2) Closure problem
When a proper smoothed velocity is chosen, SPH and LES solve the same governing equations. Therefore, SPH has the same closure problem as LES in that we have more variables than the number of equations. Closure models are needed to express the de-filtered quantities in terms of the smoothed quantities. On the other hand, SPH-i is a complete model with no closure problems.

(3) turbulent flows
Standard SPH follows the LES [51] or LANS-α[47][48] approach (depending on the formulation) in simulating turbulence whereas SPH-i is fundamentally a DNS approach since no approximations beyond the Navier-Stokes equations are assumed. Using the proposed SPH-i model, turbulent flows can be simulated without the additional complication of turbulence modeling.

(4) Particle motion
In the SPH context, the smoothed SPH particle moves with averaged physical properties $\{\langle\rho_h\rangle, \langle p_h\rangle, \widetilde{\mathbf{u}}_h\}$ and this particle is moved by $d\mathbf{r}/dt := \widetilde{\mathbf{u}}_h$. On the other had, the unsmoothed SPH-i particle moves with its individual disordered physical attributes given by the continuum field $\{\rho, p\rangle, \mathbf{u}\}$ and this particle is moved by $d\mathbf{u}/dt := \mathbf{u}$.

Furthermore, a general approach for constructing compatible convolution and deconvolution filter pairs on $\mathbb{R}^2$ has been proposed. The same ideas can easily be adopted to construct filter pairs on $\mathbb{R}^3$. We then conjecture that if spatial averages vary negligibly over a range of length scales then the convolution-deconvolution operators may be used to construct convolution and deconvolution filters. We have proposed a new class of compactly supported rational convolution filters (approximate Gaussian filters) from which approximate deconvolution filters were constructed by means of ADM.

As an alternative to the widely popular choice of using an equation of state for pressure, in this paper we propose a dynamic equation for updating the pressure; it admits both liquids and gases. Under the assumptions of isentropic flow, however, it has been shown that this equation reduces to an equation of state. From a purely computational perspective, by using an equation for pressure, the pressure can be updated at the same time as the density and velocity. Constructed as an alternative to the δ-SPH proposed in[7], it provides an implicit mechanism for filtering high frequency pressure oscillations, a feature that is absent in the widely used simple equation of state.

Chapter 6

Solid Boundary Treatment

Modeling solid boundary conditions remains an open problem in standard SPH. Unlike mesh-based approaches, it is currently not possible to directly and rigorously implement solid boundary conditions. Boundary conditions influence the accuracy of SPH, thus limiting the application of SPH to engineering problems.

6.1 Arbitrary boundaries

There are two main approaches for enforcing solid boundary conditions; the dynamic boundary condition and repulsive boundary condition. The dynamic boundary condition uses ghost or mirror particles outside the computational domain to implement the no-penetration boundary condition. However, this approach does not entirely prevent fluid particles escaping from the domain through the solid boundary. While the repulsive boundary condition can adequately prevent particle penetration, it causes truncation of the support domain of the fluid particles leading to pressure oscillations. By coupling the dynamic boundary condition with a repulsive force, Shao et.al [52] reported an improvement in the implementation of the solid boundary.

When a fluid particle is in the vicinity of a solid boundary, its physical properties should not change and it must not penetrate through; this is the no-penetration boundary condition. A particle near the wall still has physical properties such as density. In the context of particle methods, this is not particularly easy to implement.

6.2 Purely repulsive boundary force models

The solid boundary is modeled by a single layer of boundary particles with fixed mass, density and zero pressure. Their positions are fixed unless otherwise the solid boundary is moving. As a fluid particle approaches the solid boundary, the repulsive force becomes stronger with decreasing distance from the boundary. The earliest such model was the Lennard-Jones potential proposed by Monaghan [16] in his seminal work that he introduced SPH to free-

surface flow modeling.

$$\mathbf{f}(\mathbf{r}_{ij}) = \begin{cases} D\left[\left(\frac{r_0}{||\mathbf{r}_{ij}||}\right)^{12} - \left(\frac{r_0}{||\mathbf{r}_{ij}||}\right)^{4}\right]\frac{\mathbf{r}_{ij}}{||\mathbf{r}_{ij}||} & , ||\mathbf{r}_{ij}|| \leq r_0 \\ 0 & \text{otherwise} \end{cases} \tag{6.1}$$

where $||\mathbf{r}_{ij}||$ is the separation distance between fluid particle i and boundary particle j. The boundary layer or cut off length r_0 is generally chosen as the initial particle spacing. The parameter D is problem dependent; for dam break problems, for instance, it is chosen to be gd where d is the still water level. As can be seen from (6.1) the force acts along the line of sight between the two interacting particles. When a fluid particle is so close to the boundary particle, it feels a very large force which may disturb the flow. Further, to model slip boundary conditions boundary particles must be taken into account when calculating viscous forces. Due to the truncation of the support domain of fluid particles by the solid boundary, the boundary disturbs the density and pressure of nearby particles. These disturbances may enhance, leading to instabilities which may affect the evolution of the system in the long term. Another problem with this model is that the boundary force is radial; it is not constant when a fluid particle is moving at fixed distance from the boundary. This has a ripple effect on the fluid flow.

To address the drawbacks of the Lennard-Jones model, recently, Monaghan [53] has proposed an alternative model in which the resultant force on a fluid particle due to the boundary remains perpendicular to boundaries with negligible error. The force per unit mass is given as

$$\mathbf{f}(\mathbf{r}_{ij}) = \begin{cases} \frac{K}{\beta}\frac{\mathbf{r}_{ij}}{||\mathbf{r}_{ij}||^2}W\left(\frac{||\mathbf{r}_{ij}||}{h}\right)\frac{2m_i}{m_i+m_j} & , ||\mathbf{r}_{ij}|| \leq r_0 \\ 0 & \text{otherwise} \end{cases} \tag{6.2}$$

Here, the parameter β ensures that when the spacing between boundary particles is changed the resultant force on a fluid particle is invariant. If, for instance, the spacing is halved, the number of boundary particles is doubled but this is then mitigated by β being twice as great. Monaghan recommends that the spacing between boundary particles relative to fluid particles should be $\beta \sim 3$ to guarantee that (i) the tangential force relative to the normal force and (ii) the relative variation in normal force for a fixed distance above the boundary are both negligibly small ($< 10^{-5}$). The other parameter K is set to the typical velocity in the simulation; as such, it is problem dependent. The kernel W_{ij} can be any smoothing function. In [53] Monaghan uses the Wendland kernel.

Another recent radial boundary force model was proposed by Shao et.al [52].

$$\mathbf{f}_{ij} := K\left(1 - \frac{||\mathbf{r}_{ij}||}{r_0}\right) f(\eta)\frac{\mathbf{r}_{ij}}{||\mathbf{r}_{ij}||^2}, \quad \eta = \frac{\mathbf{r}_{ij}}{0.75||\mathbf{r}_{ij}||^2}, \quad 0 < ||\mathbf{r}_{ij}|| < r_0 \tag{6.3}$$

$$\mathbf{f}(\mathbf{r}_{ij}) = \begin{cases} \frac{2}{3} & , 0 < \eta \leq \frac{2}{3} \\ (2\eta - 1.5\eta^2) & , \frac{2}{3} < \eta \leq 1 \\ 0.5(2-\eta)^2 & , 1 < \eta \leq 2 \\ 0 & \text{otherwise} \end{cases} \tag{6.4}$$

Unlike the Lennard-Jones molecular force, this improved soft repulsive force model can prevent unphysical particle penetration without any observable pressure disturbances.

The above forces are not truly physical as they are not related to the direction and magnitude of the velocity field although they can successfully prevent particle penetration through the boundary.

6.3 Damped repulsive boundary force model

The radial boundary force models in the preceding section are all repulsive and nonlinear. It is possible to introduce linear force models which may not disturb the flow significantly. As fluid particles interact with solid boundaries, the interactions are not perfectly elastic. Therefore, the solid boundary is not only *repulsive*, it should also *slow down* the approaching fluid particles. The simplest way to take these two features of physical bodies into account is to use viscoelastic springs that damp out relative motion between fluid and boundary particles.

The objective is then to study a constrained problem where we want to derive a damped boundary force model such that a fluid particle i and a boundary particle j are at least a distance r_0 apart. For fluid particle i, we first determine the list of near neighbor boundary particles $j \in \mathcal{N}(i)$. To solve this problem a potential V^s is introduced as follows;

$$V^s(||\mathbf{r}_{ij}||) = \begin{cases} \sum_{i=1} \sum_{j \in \mathcal{N}(i)} \frac{1}{2} k_{ij}^s \left(||\mathbf{r}_{ij}|| - r_0\right)^2 & , ||\mathbf{r}_{ij}|| < r_0 \\ 0 & , \text{otherwise} \end{cases} \tag{6.5}$$

where k_{ij}^s are the stiffness coefficients for each interaction pair. Furthermore, for this elastic system, the Lagrangian can easily be written down.

$$L = \sum_{i=1} \frac{1}{2} m_i ||\mathbf{u}_i||^2 - V^s(||\mathbf{r}_{ij}||) \tag{6.6}$$

for all $||\mathbf{r}_{ij}|| \leq r_0$.

As the boundary is dissipative, the Rayleigh dissipation function that depends on relative position and velocity of the particles is introduced.

$$F^d = \sum_{i=1} \sum_{j \in \mathcal{N}(i)} \frac{1}{2} \underline{\underline{K}}_{ij}^d(\mathbf{r}_{ij}) : \mathbf{u}_{ij} \otimes \mathbf{u}_{ij} \tag{6.7}$$

which implicitly depends on the relative position $\mathbf{r}_{ij} := \mathbf{r}_i - \mathbf{r}_j$ with explicit dependence on the relative velocity $\mathbf{u}_{ij} := \mathbf{u}_i - \mathbf{u}_j$. The damping tensor $\underline{\underline{K}}_{ij}^d$ is assumed to be dependent on the radial position for each interaction pair (i, j). From purely mechanical arguments no conclusion can be drawn about the symmetries of $\underline{\underline{K}}_{ij}^d$ and k_{ij}^s with respect to the particle indexes i and j. Methods of statistical physics, however, make it possible to rigorously demonstrate that in all physically possible scenarios [54]

$$\underline{\underline{K}}_{ij}^d = \underline{\underline{K}}_{ji}^d \qquad k_{ij}^s = k_{ji}^s \tag{6.8}$$

There are many possible choices for the damping tensor, but for the purposes of this work the following form is used.

$$\underline{\underline{K}}_{ij}^d = \frac{1}{2} k_{ij}^d \frac{\mathbf{r}_{ij} \otimes \mathbf{r}_{ij}}{||\mathbf{r}_{ij}||^2} \tag{6.9}$$

Therefore, the resultant force experienced by a fluid particle i due to the influence of a set of near neighbor boundary particles $\mathcal{N}(i)$ can be determined by solving the Euler-Lagrange equations of motion.

$$\frac{d}{dt}\left(\frac{\partial L}{\partial \mathbf{u}_i}\right) - \frac{\partial L}{\partial \mathbf{r}_i} = -\frac{\partial F^d}{\partial \mathbf{u}_i} \tag{6.10}$$

Then the force exerted on fluid particle i is given by

$$\mathbf{f}_i := m_i \frac{d}{dt}\mathbf{u}_i = -\sum_{j=\mathcal{N}(i)} k_{ij}^s \left(||\mathbf{r}_{ij}|| - r_0\right) \frac{\mathbf{r}_{ij}}{||\mathbf{r}_{ij}||} - \sum_{j=\mathcal{N}(i)} k_{ij}^d \frac{\mathbf{u}_{ij}\cdot\mathbf{r}_{ij}}{||\mathbf{r}_{ij}||^2}\mathbf{r}_{ij} \tag{6.11}$$

with the force vanishing for $||\mathbf{r}_{ij}|| \geq r_0$. Next, for fluid particles $i = 1, 2, 3, ..., \mathrm{N}$ the total energy lost or gained from an applied force is defined through the line integral along each particle's trajectory C.

$$W = \sum_{i=1} \int_{C_i} \mathbf{f}_i \cdot d\mathbf{r}_i = \sum_{i=1} \int_{t_0}^{t} \mathbf{f}_i \cdot \mathbf{u}_i dt \tag{6.12}$$

Then the rate of work done induced by the boundary forces on the fluid can be computed with the help of Euler's theorem of homogeneous functions and the fundamental theorem of calculus to give the following important result.

$$\begin{aligned}
\dot{W} &= \frac{d}{dt}\sum_{i=1} \int_{t_0}^{t} \mathbf{f}_i \cdot \mathbf{u}_i dt \\
&= \sum_{i=1} \mathbf{f}_i^d \cdot \mathbf{u}_i \\
&= -\sum_{i=1} \frac{\partial F^d}{\partial \mathbf{u}_i} \cdot \mathbf{u}_i \\
\therefore \dot{W} &= -2F^d \leq 0
\end{aligned} \tag{6.13}$$

The minus sign is due to the force and velocity acting in opposite directions. Furthermore, since the dissipation function is non-negative $F^d \geq 0$, the damped boundary forces will slow down an approaching, accelerating fluid particle by damping out its energy. The second important feature of the boundary force model (6.11) is to constrain the fluid particles to be at least a distance r_0 from the boundary by minimizing the behavior function $C_{ij} := ||\mathbf{r}_{ij}|| - r_0$ to zero. Thirdly, the dissipative component of the force projects the relative velocity onto the relative position meaning that it does not damp rigid body rotations.

Determining the stiffness and damping coefficients for a complex system is a very challenging problem. Generally, these coefficients will be determined by trial and error. However, a seemingly good approximation for the damping coefficients that does not over dissipate the mechanical energy of the fluid body can be found. In this work, assuming homogeneity, it is computed as

$$k_{ij}^d \equiv k^d \doteq \frac{m_{\mathrm{B}}\nu}{\Delta r_{\mathrm{B}}^2} \tag{6.14}$$

where ν is the kinematic viscosity, m_{B} is the mass of a boundary particle and Δr_{B} is interval over which the boundary forces act i.e. boundary layer thickness.

Chapter 7

Power Balance

This chapter presents a study of the thermo-mechanical power delivered to a fluid body. A decomposition of this input power is made to separate useful power and power loss components. For wave energy harvesting purposes, it is this useful power that can be harnessed into electrical energy. The respective power terms are then presented in terms of the SPH-i model at both the continuum and discrete levels.

7.1 General

The first law of thermodynamics states that the rate of change of the total energy stored in a system must balance the sum of the net mechanical power delivered or extracted from the system by the environment and the rate at which any other energy enters the system. There are many forms in which energy can be stored including; mechanical motion, elastic energy, heat flux, electromagnetic currents etc. In this work only the interplay between mechanical power, elastic energy and heat will be considered.

A fluid domain Ω bounded by a surface $\partial\Omega$ is considered as the fluid body. To study the power delivered to this fluid body, we start with the CNSEs given by equations (2.7), (2.8) and (2.9). If we multiply the momentum conservation law (2.8) by $\mathbf{u}$ and integrate over the fluid domain Ω, we obtain

$$\int_{\Omega} \rho \frac{d}{dt}\left(\frac{1}{2}||\mathbf{u}||^2\right) d\Omega = \int_{\Omega} \rho \mathbf{b} \cdot \mathbf{u} d\Omega + \int_{\Omega} \left(\nabla \cdot \underline{\underline{\tau}}\right) \cdot \mathbf{u} d\Omega \tag{7.1}$$

where $\mathbf{b}$ is the body force per unit mass. With further application of vector calculus, the divergence theorem, Reynolds' transport theorem and the energy conservation law (2.9) to the second term in (7.1), we arrive at the balance

$$\frac{d}{dt}\int_{\Omega}\left(\frac{1}{2}||\mathbf{u}||^2 + u\right)\rho d\Omega = \int_{\Omega} \rho \mathbf{b} \cdot \mathbf{u} d\Omega + \int_{\partial\Omega} \underline{\underline{\tau}} : \mathbf{u} \otimes \hat{\mathbf{n}} dS - \int_{\partial\Omega} \mathbf{q} \cdot \hat{\mathbf{n}} dS \tag{7.2}$$

The left hand side of the balance (7.2) is the rate of change of the total energy of the fluid contained in the fluid body Ω. The internal energy U is expressed in terms of the internal energy density u which includes both elastic energy and also heat. The exact form of the elastic energy depends on the specific mechanical behavior of a material. The power balance (7.2) shows that the rate at which work is done to the fluid body Ω includes the power

delivered to it by body and surface forces, while the heat flux vector $\mathbf{q}$ estimates the amount of heat flowing out of the system. Thus, the thermo-mechanical power input to the system is given as

$$\begin{aligned}\mathcal{P}_{in} &= \int_{\Omega} \rho \mathbf{b} \cdot \mathbf{u} d\Omega + \int_{\partial\Omega} \underline{\underline{\tau}} : \mathbf{u} \otimes \hat{\mathbf{n}} dS - \int_{\partial\Omega} \mathbf{q} \cdot \hat{\mathbf{n}} dS \\ &= \int_{\Omega} \rho \mathbf{b} \cdot \mathbf{u} d\Omega + \int_{\Omega} \nabla \cdot \left(\underline{\underline{\tau}} \cdot \mathbf{u} \right) d\Omega + \int_{\Omega} \nabla \cdot (k \nabla T) \, d\Omega \end{aligned} \tag{7.3}$$

assuming Fourier's heat conduction law $\mathbf{q} := -\nabla T$ holds.

7.2 Decomposition of the input power

The input power is decomposed into useful power and power loss terms due to viscosity and heat outflow. The power terms are further represented at the continuum level using the SPH-i model.

(1) Power delivered by body forces

$$\mathcal{P}_{in}^{\text{bf}} = \int_{\Omega} \rho \mathbf{b} \cdot \mathbf{u} d\Omega \tag{7.4}$$

(2) Power delivered by normal stresses

$$\begin{aligned}\mathcal{P}_{in}^{\text{nf}} &= -\int_{\Omega} \nabla \cdot (p\mathbf{u}) \, d\Omega \\ &= -\int_{\Omega}\int_{\Omega} \left(\frac{p(\mathbf{r})\mathbf{u}(\mathbf{r})}{\rho(\mathbf{r})} \langle \rho_h(\mathbf{r}') \rangle + \frac{p(\mathbf{r}')\mathbf{u}(\mathbf{r}')}{\rho(\mathbf{r}')} \langle \rho_h(\mathbf{r}) \rangle \right) \cdot \nabla \varphi_h d\Omega(\mathbf{r}') d\Omega(\mathbf{r}) \end{aligned} \tag{7.5}$$

(3) Power delivered by shear stresses

$$\begin{aligned}\mathcal{P}_{in}^{\text{vf}} &= \int_{\Omega} \nabla \cdot \left(\underline{\underline{\sigma}} \cdot \mathbf{u} \right) d\Omega \\ &= \int_{\Omega}\int_{\Omega} \left(\frac{\underline{\underline{\sigma}}(\mathbf{r}) \cdot \mathbf{u}(\mathbf{r})}{\rho(\mathbf{r})} \langle \rho_h(\mathbf{r}') \rangle + \frac{\underline{\underline{\sigma}}(\mathbf{r}') \cdot \mathbf{u}(\mathbf{r}')}{\rho(\mathbf{r}')} \langle \rho_h(\mathbf{r}) \rangle \right) \cdot \nabla \varphi_h d\Omega(\mathbf{r}') d\Omega(\mathbf{r}) \end{aligned} \tag{7.6}$$

(4) Heat outflow through the control surface

$$\begin{aligned}\mathcal{P}_{in}^{\text{hf}} &:= \int_{\Omega} \nabla \cdot \left(\frac{\gamma k}{\beta} \kappa^s \nabla p \right) d\Omega \\ &= \int_{\Omega}\int_{\Omega} \frac{\gamma k}{\beta} \left(\kappa^s(\mathbf{r}) + \langle \kappa_h^s(\mathbf{r}') \rangle \right) \left(p(\mathbf{r}) - \langle p_h(\mathbf{r}') \rangle \right) \frac{(\mathbf{r} - \mathbf{r}') \cdot \nabla \varphi_h}{||\mathbf{r} - \mathbf{r}'||^2} d\Omega(\mathbf{r}') d\Omega(\mathbf{r}) \end{aligned} \tag{7.7}$$

The power term $\mathcal{P}_{in}^{\text{hf}}$ estimates the heat flowing out of the system and is thus not useful for wave energy harvesting purposes. Similarly, the power term $\mathcal{P}_{in}^{\text{vf}}$ is a power dissipation term. Therefore the useful power for wave energy harvesting purposes can be defined as

$$\mathcal{P}_{in} = \mathcal{P}_{in}^{\text{bf}} + \mathcal{P}_{in}^{\text{nf}} + \mathcal{P}_{in}^{\text{vf}} + \mathcal{P}_{in}^{\text{hf}} \tag{7.8}$$

$$\mathcal{P}_{in}^{\text{useful}} = \mathcal{P}_{in}^{\text{bf}} + \mathcal{P}_{in}^{\text{nf}} \tag{7.9}$$

7.3 Decomposition of the viscous power delivered

The velocity gradient or deformation tensor is made up of two parts; symmetric and anti-symmetric components.

$$\begin{aligned} \nabla\mathbf{u} &= \frac{1}{2}\left(\nabla\mathbf{u} + \nabla\mathbf{u}^{\text{T}}\right) + \frac{1}{2}\left(\nabla\mathbf{u} - \nabla\mathbf{u}^{\text{T}}\right) \\ &= \underline{\underline{S}} + \underline{\underline{\Omega}} \end{aligned} \tag{7.10}$$

where $\underline{\underline{S}}$ is the strain rate tensor and $\underline{\underline{\Omega}}$ is the rotation rate or vorticity tensor. It can be shown that the vorticity tensor is made up of the components of the vorticity vector $\boldsymbol{\omega}$ such that

$$\omega^{\gamma} = \epsilon^{\alpha\beta\gamma}\Omega^{\alpha\beta} \qquad \Omega^{\alpha\beta} = \frac{1}{2}\epsilon^{\alpha\beta\gamma}\omega^{\gamma} \qquad \boldsymbol{\omega} = \nabla \times \mathbf{u} \tag{7.11}$$

where $\epsilon^{\alpha\beta\gamma}$ is the Levi-Civita symbol. The vorticity tensor $\underline{\underline{\Omega}}$ may occur without change in volume and without shear deformation. It gives the rotation rate of the center of mass of a fluid particle.

For the discussion that follows, we prepare the following identities.

$$||\boldsymbol{\omega}||^2 = \nabla\mathbf{u} : \nabla\mathbf{u} - \nabla\mathbf{u} : \nabla\mathbf{u}^{\text{T}} \tag{7.12}$$

$$\nabla\mathbf{u} : \nabla\mathbf{u} = \nabla^2\left(\frac{1}{2}||\mathbf{u}||^2\right) - \nabla\cdot(\nabla\mathbf{u})\cdot\mathbf{u} \tag{7.13}$$

$$\nabla\mathbf{u} : \nabla\mathbf{u}^{\text{T}} = \nabla^2\left(\frac{1}{2}||\mathbf{u}||^2\right) - \nabla\cdot(\nabla\mathbf{u})\cdot\mathbf{u} - ||\boldsymbol{\omega}||^2 \tag{7.14}$$

$$\underline{\underline{\Omega}} : \nabla\mathbf{u} = \frac{1}{2}||\boldsymbol{\omega}||^2 \tag{7.15}$$

These identities can be proved as follows;

identities.

$$
\begin{aligned}
||\boldsymbol{\omega}||^2 &= \epsilon^{\alpha\beta\gamma}\partial_\alpha u^\beta \mathbf{e}^\gamma \cdot \epsilon^{\nu\mu\lambda}\partial_\nu u^\mu \mathbf{e}^\lambda \\
&= \epsilon^{\alpha\beta\gamma}\epsilon^{\nu\mu\gamma}\partial_\alpha u^\beta \partial_\nu u^\mu \\
&= \left(\delta^{\alpha\nu}\delta^{\beta\mu} - \delta^{\alpha\mu}\delta^{\beta\nu}\right)\partial_\alpha u^\beta \partial_\nu u^\mu \\
&= \partial_\alpha u^\beta \partial_\alpha u^\beta - \partial_\alpha u^\beta \partial_\beta u^\alpha \\
&= \nabla\mathbf{u} : \nabla\mathbf{u} - \nabla\mathbf{u} : \nabla\mathbf{u}^{\mathrm{T}} \\
\nabla^2\left(\frac{1}{2}||\mathbf{u}||^2\right) &= \partial_\alpha\partial_\alpha\left(\frac{1}{2}u^\beta u^\beta\right) \\
&= \partial_\alpha\left(u^\beta\partial_\alpha u^\beta\right) \\
&= \partial_\alpha u^\beta \partial_\alpha u^\beta + \partial_\alpha\left(\partial_\alpha u^\beta\right)u^\beta \\
&= \nabla\mathbf{u} : \nabla\mathbf{u} + \nabla\cdot(\nabla\mathbf{u})\cdot\mathbf{u} \\
\underline{\underline{\Omega}} : \nabla\mathbf{u} &= \left[\frac{1}{2}\left(\nabla\mathbf{u} - \nabla\mathbf{u}^{\mathrm{T}}\right) : \nabla\mathbf{u}\right] \\
&= \frac{1}{2}\left(\nabla\mathbf{u} : \nabla\mathbf{u} - \nabla\mathbf{u} : \nabla\mathbf{u}^{\mathrm{T}}\right) \\
&= \frac{1}{2}||\boldsymbol{\omega}||^2
\end{aligned}
$$

□

Using the definition of $\underline{\underline{\sigma}}$ given by (2.10) and the above identities, the dissipation function $\underline{\underline{\sigma}} : \nabla\mathbf{u}$ can be expressed as

$$
\begin{aligned}
\underline{\underline{\sigma}} : \nabla\mathbf{u} &= \mu\left(\nabla\mathbf{u} : \nabla\mathbf{u} + \nabla\mathbf{u}^{\mathrm{T}} : \nabla\mathbf{u}\right) - \frac{2}{d}\mu(\nabla\cdot\mathbf{u})\underline{\underline{1}} : \nabla\mathbf{u} \\
&= \mu\left[2\nabla^2\left(\frac{1}{2}||\mathbf{u}||^2\right) - 2\nabla\cdot(\nabla\mathbf{u})\cdot\mathbf{u} - ||\boldsymbol{\omega}||^2\right] - \frac{2}{d}\mu(\nabla\cdot\mathbf{u})^2
\end{aligned} \tag{7.16}
$$

It then follows that the specific power $\nabla\cdot\left(\underline{\underline{\sigma}}\cdot\mathbf{u}\right)$ delivered by viscous forces to the fluid body becomes

$$
\begin{aligned}
\nabla\cdot\left(\underline{\underline{\sigma}}\cdot\mathbf{u}\right) &= \left(\nabla\cdot\underline{\underline{\sigma}}\right)\cdot\mathbf{u} + \underline{\underline{\sigma}} : \nabla\mathbf{u} \\
&= \left(\nabla\cdot\underline{\underline{\sigma}}\right)\cdot\mathbf{u} - 2\mu\nabla\cdot(\nabla\mathbf{u})\cdot\mathbf{u} + \mu\left[2\nabla^2\left(\frac{1}{2}||\mathbf{u}||^2\right) - ||\boldsymbol{\omega}||^2\right] - \frac{2}{d}\mu(\nabla\cdot\mathbf{u})^2 \\
&= \nabla\cdot\left(\underline{\underline{\sigma}} - 2\mu\nabla\mathbf{u}\right)\cdot\mathbf{u} + \mu\left[2\nabla^2\left(\frac{1}{2}||\mathbf{u}||^2\right) - ||\boldsymbol{\omega}||^2\right] - \frac{2}{d}\mu(\nabla\cdot\mathbf{u})^2 \\
&= -2\mu\left(\nabla\cdot\underline{\underline{\Omega}}\right)\cdot\mathbf{u} + 2\mu\nabla^2\left(\frac{1}{2}||\mathbf{u}||^2\right) - \mu||\boldsymbol{\omega}||^2 - \frac{2}{d}\mu\nabla\cdot(\mathbf{u}\nabla\cdot\mathbf{u})
\end{aligned} \tag{7.17}
$$

Therefore, the power delivered to the fluid body by viscous forces, in decomposed form, takes the following form;

$$
\begin{aligned}
\int_\Omega \nabla\cdot\left(\underline{\underline{\sigma}}\cdot\mathbf{u}\right)dV = -2\mu\int_\Omega\left(\nabla\cdot\underline{\underline{\Omega}}\right)\cdot\mathbf{u}dV + 2\mu\int_\Omega\nabla^2\left(\frac{1}{2}||\mathbf{u}||^2\right)dV \\
- 2\mu\int_\Omega\frac{1}{2}||\boldsymbol{\omega}||^2dV - \frac{2}{d}\mu\int_\Omega\nabla\cdot(\mathbf{u}\nabla\cdot\mathbf{u})\,dV
\end{aligned} \tag{7.18}
$$

Next, equation (7.16) can be reshaped as;

$$\mathcal{P}_{in}^{vf} = \mathcal{P}_{in}^{\Omega} + \mathcal{P}_{in}^{fs} + \mathcal{P}_{in}^{\omega} \tag{7.19}$$

where the terms on the right-hand side are;

$$\begin{aligned}\mathcal{P}_{in}^{fs} &= 2\mu \int_{\Omega} \left[\nabla^2 \left(\frac{1}{2}||\mathbf{u}||^2\right) - \frac{1}{d}\nabla \cdot (\mathbf{u}\nabla \cdot \mathbf{u})\right] dV \qquad (7.20)\\ &= 2\mu \int_{\partial\Omega} \hat{n} \cdot \left[\nabla \left(\frac{1}{2}||\mathbf{u}||^2\right) - \mathbf{u}\nabla \cdot \mathbf{u}\right] dS\\ \mathcal{P}_{in}^{\Omega} &= -2\mu \int_{\Omega} \left(\nabla \cdot \underline{\underline{\Omega}}\right) \cdot \mathbf{u} dV \qquad (7.21)\\ &= 2\mu \int_{\Omega} \underline{\underline{E}} : \mathbf{u} \otimes \nabla\omega dV \qquad \text{in 2D}\\ \mathcal{P}_{in}^{\omega} &= -2\mu \int_{\Omega} \frac{1}{2}||\boldsymbol{\omega}||^2 dV \qquad (7.22)\end{aligned}$$

where the tensor $\underline{\underline{E}}$, in the basis set $\{\mathbf{e}^1, \mathbf{e}^2, \mathbf{e}^3\}$ and the 2D vorticity $\boldsymbol{\omega} = \omega\mathbf{e}^3$ is define as

$$\underline{\underline{E}} := \frac{1}{2}\left(\mathbf{e}^1 \otimes \mathbf{e}^2 - \mathbf{e}^2 \otimes \mathbf{e}^1\right) \tag{7.23}$$

The power terms $\mathcal{P}_{in}^{fs}$ is linked to the motion of the domain boundaries $\partial\Omega = \partial\Omega_{\text{FS}} \cup \partial\Omega_{SB}$; here $\partial\Omega_{\text{FS}}$ is the free surface and $\partial\Omega_{\text{SB}}$ is a moving solid boundary. The volume integral $\mathcal{P}_{in}^{\omega}$ is the power delivered to the fluid body due to enstrophy while $\mathcal{P}_{in}^{\Omega}$ is the power linked to the local rotation of the fluid particles.

By invoking the SPH quadrature, the power components above can be represented at the discrete level under the SPH-i approach. This procedure is called particle discretization. Here i represents the target or test fluid particle whereas $\mathcal{N}(i) \ni j$ is the set of nearest neighbor fluid particles to particle i. The mass element is defined as $m_i := \rho_i dV_i$.

$$\mathcal{P}_{in}^{\text{bf}} \doteq \sum_{i=1}^{N} m_i \boldsymbol{g} \cdot \mathbf{u}_i \tag{7.24}$$

$$\mathcal{P}_{in}^{\text{nf}} \doteq -\sum_{i=1}\sum_{j=1} \frac{m_i m_j}{\rho_i \rho_j}\left(\frac{p_i \mathbf{u}_i}{\rho_i}\langle\rho_j^h\rangle + \frac{p_j \mathbf{u}_j}{\rho_j}\langle\rho_i^h\rangle\right) \cdot \nabla_i \varphi_{ij}^h \tag{7.25}$$

$$\mathcal{P}_{in}^{\text{vf}} \doteq \sum_{i=1}\sum_{j=1} \frac{m_i m_j}{\rho_i \rho_j}\left(\frac{\underline{\underline{\sigma}}_i \cdot \mathbf{u}_i}{\rho_i}\langle\rho_j^h\rangle + \frac{\underline{\underline{\sigma}}_j \cdot \mathbf{u}_j}{\rho_j}\langle\rho_i^h\rangle\right) \cdot \nabla_i \varphi_{ij}^h \tag{7.26}$$

$$\mathcal{P}_{in}^{\text{hf}} \doteq \sum_{i=1}\sum_{j=1} \frac{m_i m_j}{\rho_i \rho_j}\frac{\gamma k}{\beta}\left(\kappa_i^s + \langle\kappa_j^s\rangle\right)\left(p_i - \langle p_j^h\rangle\right)\frac{\mathbf{r}_{ij} \cdot \nabla_i \varphi_{ij}^h}{||\mathbf{r}_{ij}||^2} \tag{7.27}$$

Chapter 8

Free-Surface Flow validation Tests

8.1 Hydrostatic pressure in a water tank

The hydrostatic pressure problem is one of the fundamental benchmark test cases in SPH. For many traditional SPH approaches it is a challenging problem to obtain a stable, regularized pressure field [6][55]. The set for this numerical simulation is as shown in figure 8.1. The numerical water tank has a square shape of side 1m. It is filled with fluid particles to a height of $h_0 = 0.3$m and a pressure probe point P is placed $y_p = 0.06$m above the bottom. With a zero reference pressure on the free surface, the hydrostatic pressure at the probe point P is given by $p = \rho_0 g(h_0 - y_p) = 2354.4$Pa. The initial particle spacing is set at $dx = dy = 0.01$m so that the total number of fluid particles is $N = 100 \times 30 = 3000$ while the average number of nearest neighbor is fixed at $N_n = 19$. The density is initialized to the rest value $\rho_0 = 1000\text{Kgm}^{-3}$ whereas the pressure and velocity are initially set to zero. As discussed in section 3.7, the compact support radius in units of h is then $\xi = \sqrt{N_n/4\pi} = 1.23$. The smoothing length is thus $h = \xi \Delta x = 0.0123$m.

The solid boundary treatment is enforced by the proposed damped boundary force model with a damping coefficient of $k^d = 0.10606\text{Nsm}^{-1}$ and a stiffness coefficient of $k^s = 0.06065\text{Nm}^{-1}$ for each particle.

The thermal diffusivity and kinematic viscosity were respectively $\alpha = 0.015\text{m}^2\text{s}^{-1}$ and $\nu = 1.0 \times 10^{-6}\text{m}^2\text{s}^{-1}$. A suitable time step for the time integration was $\Delta t = 1.0 \times 10^{-5}$s

Figure 8.2 shows a snapshot of the pressure filed obtained by the SPH$-i$ model at time

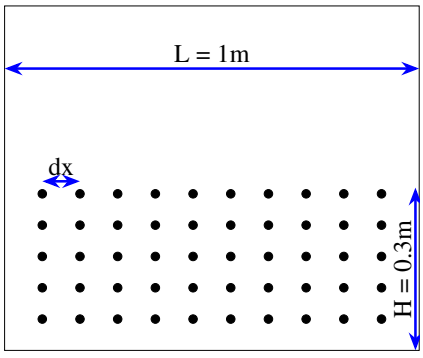

Figure 8.1: numerical water tank setup.

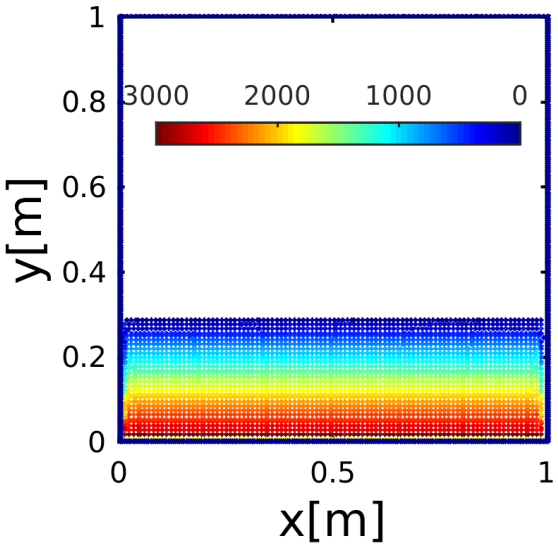

Figure 8.2: Snapshot of the pressure field at time $t = 15$s obtained by the SPH$-i$ model.

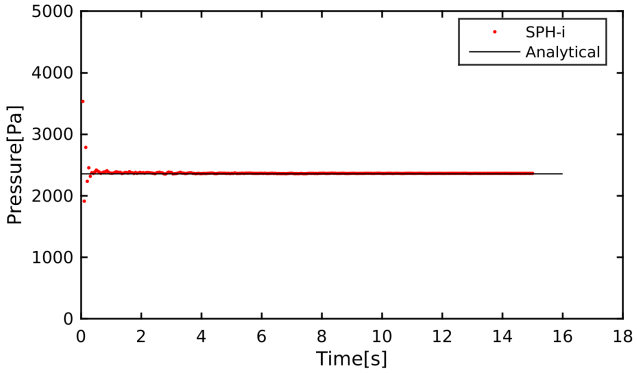

(a) Pressure time history

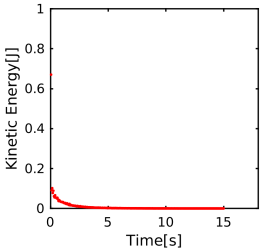

(b) Total kinetic energy

Figure 8.3: Time history of the pressure at the probe point P $(y = 0.06\text{m})$ obtained by the SPH$-i$ model in 8.3a. Here 8.3b is the total kinetic energy of the fluid.

$t = 15$s. In order to check the long term numerical stability, the simulation was allowed to run for an extended time of $t = 15$s. It is observed that SPH$-i$ model gives a smooth pressure distribution.

A time history of the pressure at the probe point P is as shown in figure 8.3a and 8.4a. Initially there is a time lag of about 0.5s during which time gravity squeezes the fluid down. However, pressure gradients quickly build up, and together with boundary forces counter-balances the gravitational push. Thus the fluid adjusts to a new equilibrium position through an oscillation mode. The SPH$-i$ models clearly preserves hydrostatic pressure equilibrium for long-time simulations as can be seen in figure 8.4a. This also indicates that the diffusion terms in the pressure equation can effectively smooth out numerical noise in the pressure field. Furthermore, the kinetic energy asymptotically decays to zero as shown in figure 8.3b. At finite times, however, the kinetic energy is small but non-zero. Therefore, the fluid particles will tend to oscillate about their mean positions; consistent with a physical system.

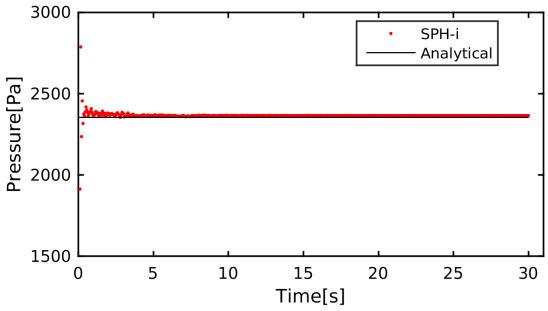

(a) Pressure time history

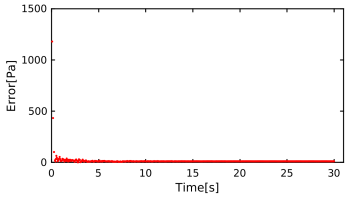

(b) Error

Figure 8.4: Time history of the pressure at the probe point P $(y = 0.06\text{m})$ obtained by the SPH$-i$ model in 8.4a. Here 8.4b is the residual between the numerical and exact solutions.

In some SPH models the hydrostatic pressure profile slowly diverges from the numerical solution at long-time simulation [6]. This is attributed to numerical diffusion in those models. To ascertain the possibility of any instability build-up due to numerical diffusion, the simulation was allowed to progress for a much long time as shown in figure 8.4.

8.2 Dam break on a dry bed

The second test case that was considered in this work is the violent shallow water breaking wave process generated by a dam break in a finite domain. It is one of the fundamental benchmark problems in the numerical study of free surface flows. The dam break flow is a highly nonlinear, complex phenomena that is characterized by large free surface deformation, splash up and multiple breaking events. Figure 8.5 shows a schematic diagram of the experiment reported in [56] of which the experimental data was obtained from Chen et.al. [6]. This experiment has been widely used in literature for numerical validations (refer to [6, 7, 57]) with comparisons made using various SPH models with varying degrees of accuracy. As discussed in [57], the dam break problem has several characteristic features including (i) irrotational fluid deformation (ii) water impact on vertical wall, (iii) backward plunging jet formation, (iv) several splashing cycles, (v) final sloshing flow regime, and (vi) adjustment to an hydrostatic equilibrium. The computational domain is of width $W = 1.6\text{m}$ and the water column is initially set at $L \times W = 0.6\text{m} \times 0.3\text{m}$. The initial spacing between fluid particles is $dr = 0.002\text{m}$ and in total $N = 45,000$ particles were used in the simulation. The average number of near neighbors was fixed at 91; chosen so as to minimize numerical dissipation attributable to filtering/de-filtering processes. Following the discussion in section 3.7, the compact support radius in units of h is then $\xi = \sqrt{N_n/4\pi} = 2.69$. The smoothing length is thus $h = \xi\Delta x = 0.00538\text{m}$. The sound speed was reduced to $c_s = 10\sqrt{2gH}$, thermal diffusivity $\alpha = 0.00015\text{m}^2\text{s}^{-1}$ and kinematic viscosity $\nu = 1.0 \times 10^{-6}\text{m}^2\text{s}^{-1}$ were used. To guarantee long term stability of the time integration a time step of $\Delta t = 1.0 \times 10^{-5}\text{s}$ was chosen. In the experiment a circularly shaped pressure gauge of diameter $9\text{cm}(\approx 0.15H)$ located on the vertical wall with center at 0.267H above the deck as shown in figure 8.5 was used to record the pressure time history at the probe point P.

For this test case, the Reynolds number, $Re = H\sqrt{gH}/\nu$, was 5.1×10^5 at a spatial

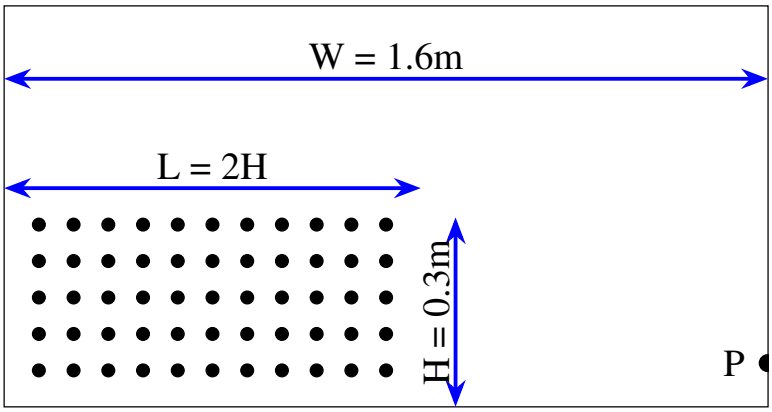

Figure 8.5: Initial set up of the numerical dam break problem.

resolution $H/dx = 150$. For the initial conditions on the field values, the fluid density was set to its rest value $\rho_0 = 1000\text{Kgm}^{-3}$ while the pressure and velocity were all initialized to zero.

The time evolution of the dam break flow is depicted in figure 8.6 along with the associated turbulent kinetic energy and turbulent dissipation rate. Initially the flow is practically uniform so that any turbulent fluctuations are negligibly small as discussed in proposition 4.2.2. Therefore, up until $t = 0.425$s both turbulent kinetic energy and the associated turbulence dissipation rate are negligibly small except near solid boundaries (see figure 8.6a and 8.6h). After the moving front hits and momentarily interacts with the right wall, turbulent kinetic energy is gradually produced (see figure 8.6b) and is quickly dissipated (see figures 8.6i). After impact with the right wall, a backward plunging jet is formed. As the plunging jet impinges on the free surface, at $t = 1.100$s, significant turbulent kinetic energy is produced (see figure 8.6c) and is quickly dissipated (see figure 8.6j). At times $t = 1.550$s and $t = 1.625$s, due to the collapse of entrapped cavities, more turbulent kinetic energy is produced and quickly dissipated . For $t > 1.625$s small secondary splash-ups develop, and finally flow enters a shallow water sloshing regime.

The plots in figure 8.7 show pressure plots obtained numerically by SPH$-i$ compared with experimental data [56]. As intuitively expected [7], when the moving front hits the vertical wall on the right, an impulse in the pressure is recorded at non-dimensional time $t\sqrt{g/H} \simeq 2.4$ and the numerical simulation by SPH$-i$ recovers the measurements relatively well.

All free -surface flow simulations with SPH$-i$ were single phase with density ratio $\rho_Y/\rho_X = 0$. The entrapment of air in the developing cavity as the plunging jet impinges on the interface introduces an air-pressure field that differs from the free-surface case. Colagrossi and Landrini [7] performed numerical simulations with their free surface and two-phase SPH models (see figure 8.8) and the free surface simulation by SPH$-i$ is shown in figure 8.7.

The backward plunging jet induces a second peak and in the experiment this occurs at $t\sqrt{g/H} \simeq 5.8$. This phenomena corresponds to the formation of a closed cavity and is here discussed by the pressure contours figure 8.8 for $\rho_Y/\rho_X = 0.001$ and 0 (top-right and bottom-left plots, respectively) and in the case of the proposed SPH$-i$ in figure 8.7 (top-right and bottom-left plots, respectively). In the free surface cases, the air-cushion effect

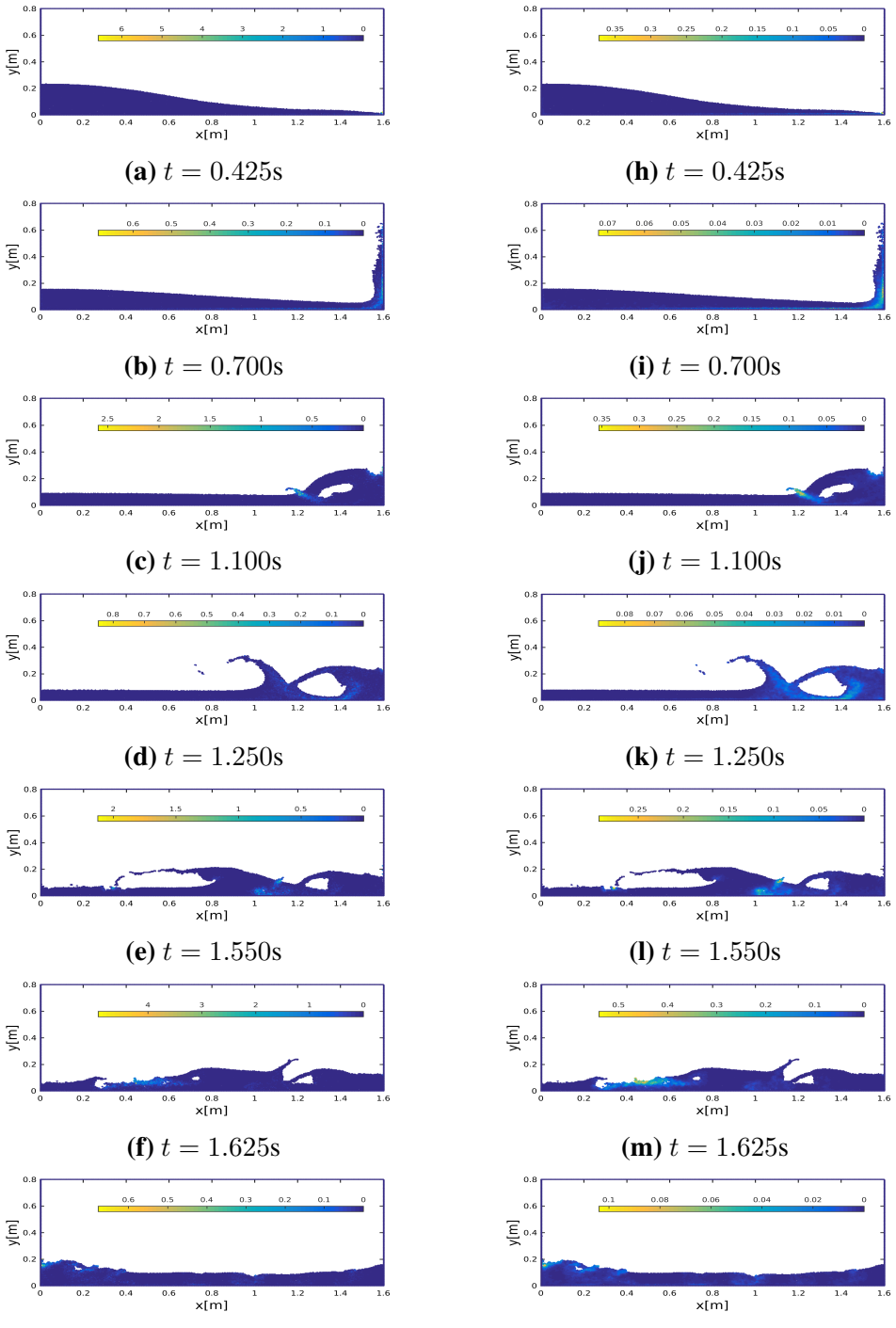

(a) $t = 0.425$s **(h)** $t = 0.425$s

(b) $t = 0.700$s **(i)** $t = 0.700$s

(c) $t = 1.100$s **(j)** $t = 1.100$s

(d) $t = 1.250$s **(k)** $t = 1.250$s

(e) $t = 1.550$s **(l)** $t = 1.550$s

(f) $t = 1.625$s **(m)** $t = 1.625$s

(g) $t = 2.275$s **(n)** $t = 2.275$s

Figure 8.6: Production and dissipation of turbulence in shallow water breaking waves, Re $= 5.1 \times 10^5$. Turbulent kinetic energy (left) and turbulent dissipation rate (right) at seven time instants.

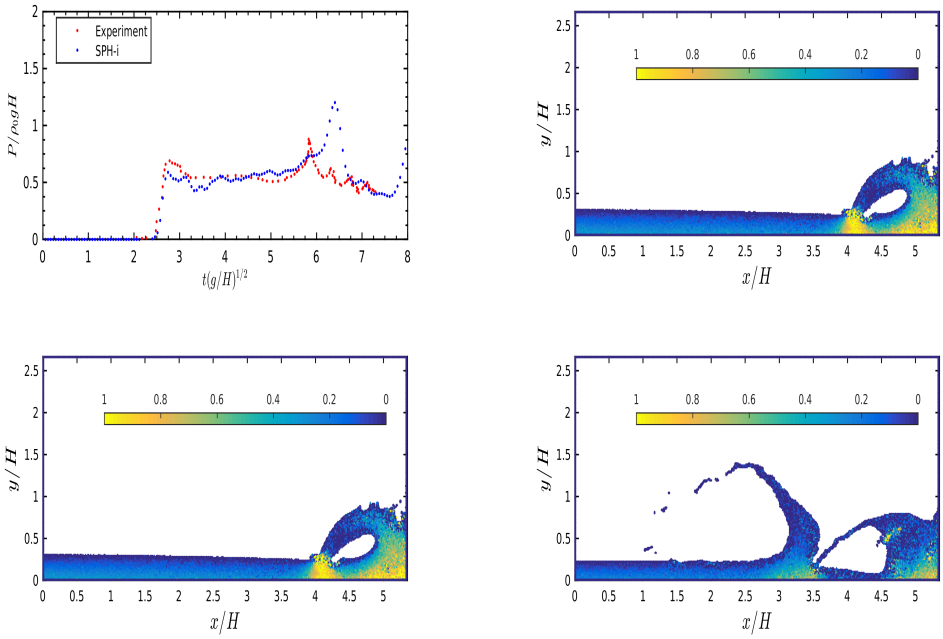

Figure 8.7: Dam break flow and impact against a vertical wall.Top left: pressure evolution on the wall; free-surface simulation by SPH$-i$ and experimental data from [56]. Bottom: free surface-flow configurations corresponding to peaks at $t\sqrt{g/H} \simeq 6.4$ and $t\sqrt{g/H} \simeq 8.0$ in the pressure evolution left and right respectively. Color: non-dimensional pressure field $P/\rho gH$ at two time instants.

is not observed which may account for the delayed pressure rise in the free surface flow cases since there is a fast circulatory flow around the entrapped cavity shown in the bottom-right plots of figures 8.8 and 8.7. Figure 8.9a shows the wave front just before impact with the vertical wall. The angle between the free surface and the bottom boundary is small $\sim 10^{\circ}$. For such small angles, an asymptotic solution based on linear wave theory [44] can be used for validation. The wave front moves with a velocity of about $U_{\max} = 1.95\sqrt{gH}$, the maximum pressure peak predicted by this theory is $P_{\max} = 0.7\rho_0 U_{\max}^2 = 2.67\rho_0 gH$. To compare this value with the SPH$-i$, a pressure probe P_0 was placed at the bottom corner on the right wall. Figure 8.9b shows the pressure time history obtained from the SPH$-i$ model. It is clear that the maximum pressure computed from the SPH$-i$ model is very close to the asymptotic solution.

8.3 Periodic wave breaking on a plane slope

Modeling of breaking waves is an important topic in coastal and marine engineering; understanding the energetics of breaking waves is fundamental to predicting the damage caused by breaking waves, tsunamis etc.

The type of wave profile converter that is proposed in this project is a rotating propeller that converts wave energy into rotational energy. A number of these rotating propellers are placed in the surf zone, near the wave breaking point. The fast forward current flow around the wave crest collides with wave energy converters (WECs), making the propellers to rotate

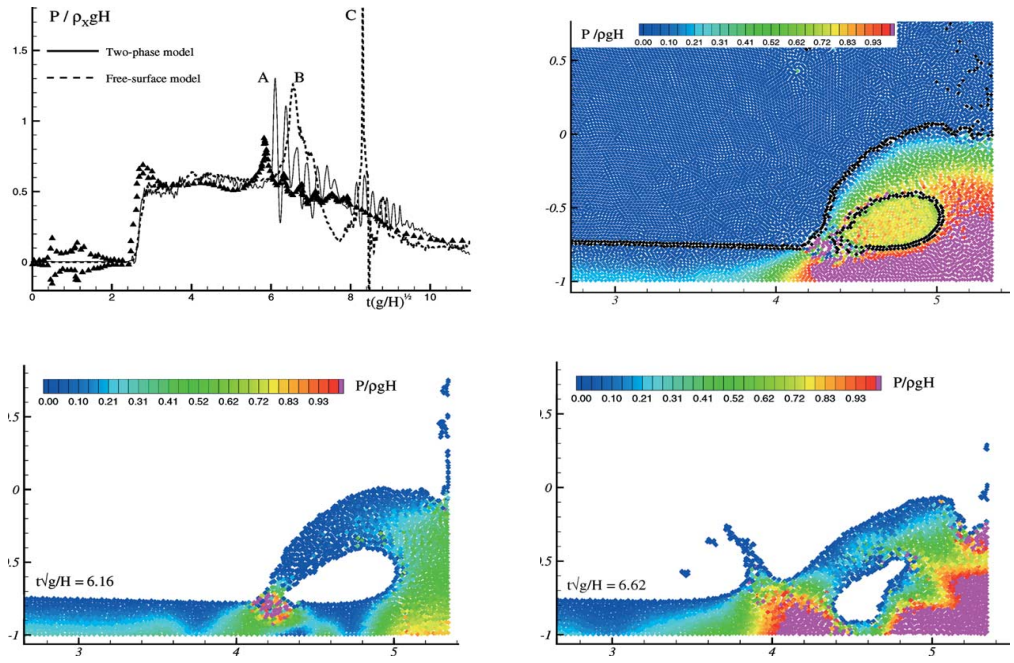

Figure 8.8: Dam break flow and impact against a vertical wall.Top left: pressure evolution on the wall; solid line: two-phase simulation; dashed line: free-surface simulation from [7];(•) experiments from [58]. Top right: air water-flow configuration, $\rho_Y/\rho_X = 0.001$, corresponding to the pressure peak A in the pressure evolution. Bottom: free surface-flow configurations corresponding to peaks B and C in the pressure evolution left and right respectively.

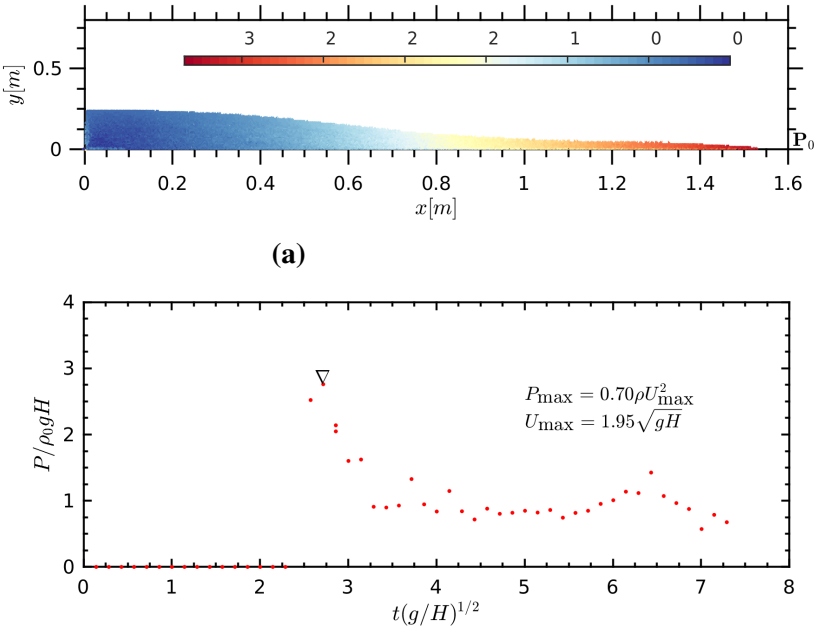

Figure 8.9: (8.9a):Fluid flow just before impact against the vertical wall. Particles are colored using the magnitude of the velocity field. (8.9b):shows the time history of SPH$-i$ pressure signals evaluated at the probe point P_0.

Figure 8.10: Wave Power Plant. Credit to my supervisor prof.Shintake for the schematic.

for the duration of wave breaking. Once the wave crest has passed, the propellers stop rotating until the next breaking wave arrives and so the generated electric power is pulsed. Under the uniform flow assumption, the accessible power of water within the plunging jet can be approximated by using the equation below.

$$P = \frac{1}{2}\rho S \bar{u}^3 \tag{8.1}$$

where $\rho = 1000\ \text{Kgm}^{-3}$ is water density, S is the surface area swept through by the propellers and $\bar{u}$ is the mean velocity of water. One characteristic feature of equation(8.1) is that wave power is proportional to the cube of fluid velocity in a way similar to wind power. Since water has a high density, high wave power can be extracted especially with the fast flow around the crest.

The generated unregulated AC power is rectified into DC power which is then temporarily stored in a super-capacitor bank. By further converting the DC power into AC power using *power inverters*, the stabilized AC line power is fed into the power grid. The power inverters offer dynamic reactive power control that helps maintain the reliability and integrity of the electric power grid. Regardless of whether there are ocean waves or not the power inverters will provide reactive power continuously. Therefore, installing these inverters on our small scale renewable energy storage system will improve voltage regulation.

Standard SPH is conceptually based on the same principle as explicit LES and therefore turbulence modeling is required. Turbulence modeling is of particular concern in modeling breaking wave phenomena. The first turbulence model for SPH was proposed by Gotoh [51]. Lo and Shao [59] first developed an ISPH-LES model while Dalrymple and Rogers[60][61] further employed the SPH for breaking waves on a beach. A comprehensive review of the various turbulent models developed for SPH was conducted by Issa and Violeau [62]. They found the results to be generally satisfactory and that improvements are necessary by investigating the free-surface influence and wall conditions. Shao and Changming [63] devised a 2D SPH-LES model to investigate plunging waves. With their model they found the computations to be in good agreement with documented data. The computed turbulence quantities

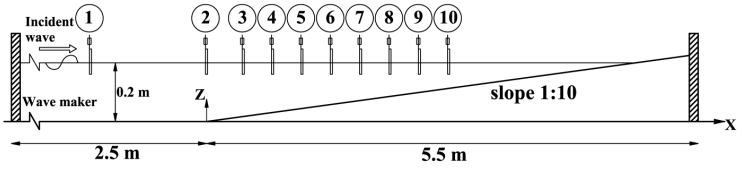

Figure 8.11: Schematic diagram of experimental set-up courtesy of Mahmoudi et.al [64]

Table 8.1: Wave breaker classification

Breaker type	ξ_0**-Range**	ξ_b**-Range**
collapsing	$\xi_0 > 3.3$	$\xi_b > 2.0$
plunging	$0.5 < \xi_0 < 3.3$	$0.4 < \xi_b < 2.0$
spilling	$\xi_0 < 0.5$	$\xi_b < 0.4$

under breaking waves agreed better with experiments when compared with $k - \epsilon$ models. An important observation arising from their work is that both the turbulence model and the spatial resolution play a fundamental role in the model predictions; with sub-particle effects becoming less significant with particle refinement.

To study the wave breaking phenomena, the SPH-i model developed in this work will be used. Comparisons with experimental data will be made.

When waves propagate in shallow water, they are influenced by shoaling effects due to the increase in wave height as water depth decreases. To investigate the breaking process, the experimental data from [64] will be used for benchmarking. In their experiment the wave propagation breaking process was recorded using a high speed camera placed normal to the glass walls of the wave flume. A schematic of the experiment set-up is shown figure 8.11. where H_0 is the wave height in deep water, H_b is the wave height at the break point i.e. edge of the surf zone and (ξ_0, ξ_b) is the iribarren number.

There are three types of breaking waves; spilling, plunging and surging. The iribarren number, defined below, is used for classifying the breaking waves. These are summarized in table 8.1. In this research plunging and spilling cases of periodic waves breaking on a plane slope were simulated. The initial particle water depth $h_0 = 0.2$m was used in all cases. The initial particle spacing was $dx = dy = 0.005$m leading to a total number of fluid particles $N = 27,160$. The average number of near neighbors was fixed at 91; chosen so as to minimize numerical dissipation attributable to filtering/de-filtering processes. Following the discussion in section 3.7, the compact support radius in units of h is then $\xi = \sqrt{N_n/4\pi} = 2.69$. The smoothing length is thus $h = \xi\Delta x = 0.00538$m.The stiffness and damping constants were fixed at $k^s = 0.00589\text{Nm}^{-1}$ and $k^d = 00002912\text{Nsm}^{-1}$.

Table 8.2: Parameter set-up for breaking wave test cases

Simulation case	**Wave height**	**Wave period**	**Stroke**	**Average Power**
case 1	0.0664	1.8	0.127	6.81
case 2	0.0758	2.7	0.224	9.52
case 3	0.07	1.14	0.08	6.25

$$\xi_0 = \frac{\tan\alpha}{\sqrt{H_0/L_0}} \qquad \text{or} \qquad \xi_b = \frac{\tan\alpha}{\sqrt{H_b/L_0}} \tag{8.2}$$

In SPH, there are two types of wavemakers are generally used; piston-type and flap-type. The piston wavemaker is used in this thesis. It is represented by a vertical column of boundary particle whose horizontal displacement, according to linear wave theory, is given by

$$x(t) = \frac{S}{2}\sin(\omega t) \tag{8.3}$$

where S is called the stroke i.e. the amplitude of the paddle oscillation. The oscillation frequency of the piston should be identical to the frequency of the generated waves. This type of wavemaker will generate a wave of height H provided that the stroke and wave height satisfy the following relation

$$\frac{H}{S} = 2\frac{\cosh(2kh_0) - 1}{\sinh(2kh_0) + 2kh_0} \tag{8.4}$$

which is the transfer function of the wave paddle. Here h_0 is the local fluid depth at the wavemaker or deep water depth. Fenton and McKee [65] derived an approximate equation for computing the wavelength of the generated waves

$$L = L_0\left(\tanh\left(\frac{2\pi h_0}{L_0}\right)^{\frac{3}{4}}\right)^{\frac{2}{3}} \qquad L_0 = \frac{gT^2}{2\pi} \tag{8.5}$$

in which L_0 is the deep water wavelength and L is the shallow water wavelength. From extended practical experience with this project, it was found that the paddle motion given by (8.3) could not lead to very stable simulations results. Therefore, for all test cases presented in this thesis the paddle motion was enforced according to the following

$$x(t) = \frac{S}{2}\Big(1 - \cos(\omega t)\Big) \tag{8.6}$$

By prescribing $\{\mathrm{T}, \mathrm{h}_0, \mathrm{H}\}$, the wavemaker can be setup by solving equations (8.5), (8.4) and (8.6). The speed of sound for determining the incompressibility modulus is obtained by $c_0 = 10\sqrt{gh_0}$ and the kinematic viscosity is taken as $\nu = 1.0\times10^{-6}\mathrm{m}^2/\mathrm{s}$, thermal diffusivity $\nu = 0.015\mathrm{m}^2/\mathrm{s}$ and adiabatic index $\gamma = 7$.

Figures 8.12 and 8.12 illustrates the plunging and splash-up processes of a periodic breaking wave whose physical parameters are respectively specified by case 1 and case 2 given in table 8.2. On the right-hand side are the snapshots taken using a high speed camera during laboratory experiments conducted by Mahmoudi et. al [64] while the SPH-i results are shown on the left hand side.

When waves propagate on a slope, wave shoaling occurs due to decreased water depth. The wave front continuously steepens until breaking occurs. As the wave propagates with phase velocity $v_p = \sqrt{gH}$, until breaking when when the fluid velocity $||\mathbf{u}||$ exceeds the phase velocity i.e. $||\mathbf{u}|| \geq v_p$.

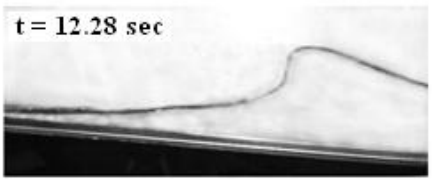

(a)

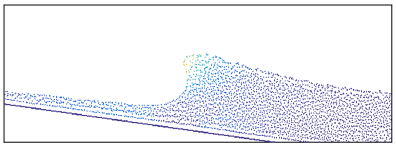

(b) $t = 12.28$s

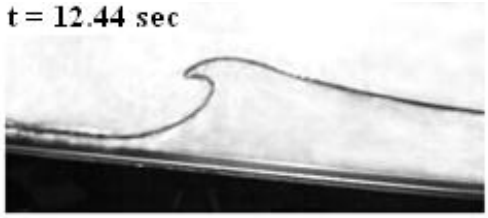

(c)

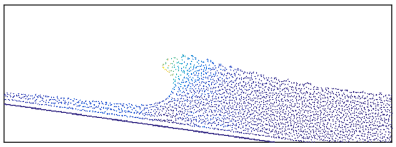

(d) $t = 12.44$s

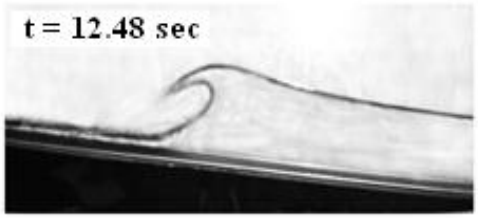

(e)

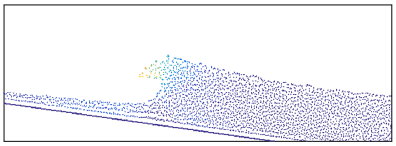

(f) $t = 12.48$s

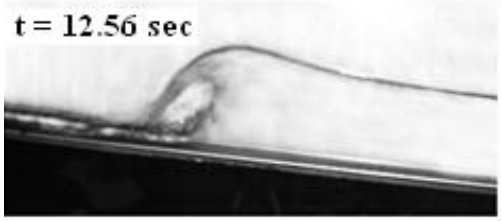

(g)

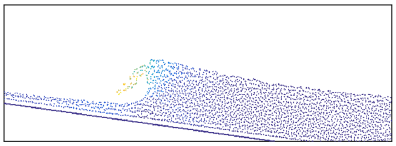

(h) $t = 12.56$s

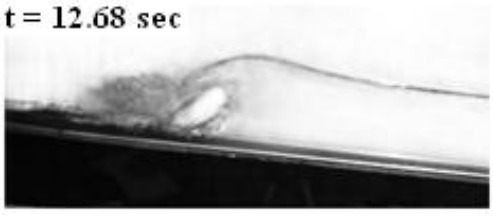

(i)

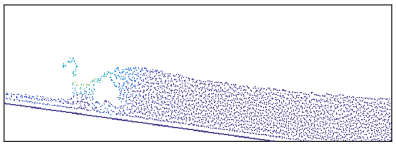

(j) $t = 12.68$s

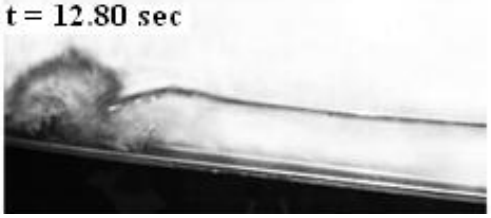

(k)

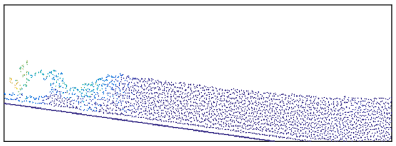

(l) $t = 12.80$s

Figure 8.12: Dissipation for a shallow water breaking wave. Kinetic energy density at eight time instants for case 1.

(a)

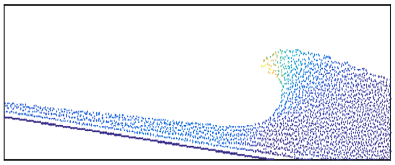

(b) $t = 14.80$s

(c)

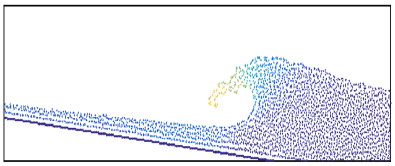

(d) $t = 14.88$s

(e)

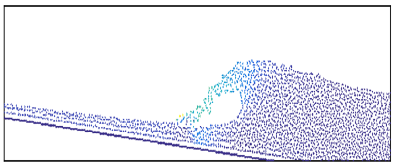

(f) $t = 14.92$s

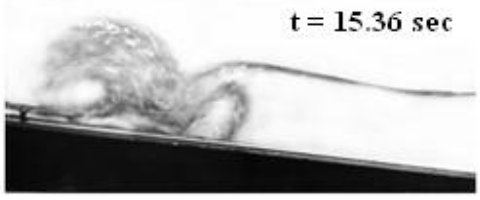

(g)

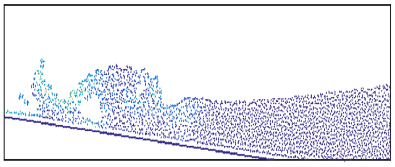

(h) $t = 15.36$s

Figure 8.13: Dissipation for a shallow water breaking wave. Kinetic energy density at four time instants for case 2.

The comparison between experimental and SPH-i results shows that the SPH-i model was able to successfully simulate the plunging breaking wave. In the initial set up of the breaker figures (8.12b),(8.12d) and (8.12f) is the on-set of turbulence. As the plunging jet hits the water surface, a splash-up process is generated; this leads to the formation of a turbulent bore that propagates towards the shore. This process is associated with high shear stress generated around the point of impact hence high turbulent kinetic energy is generated. Furthermore, as the wave undergoes breaking the kinetic energy of the fluid increases (see figure 8.12). It is this increase in kinetic energy that can be used to harness energy from the breaking wave.

The average power required to generate the waves for case 1, as shown in table 8.2 is 6.81W. Using equation (7.8), the instantaneous power delivered to the fluid body was computed and is shown in figure 8.14.

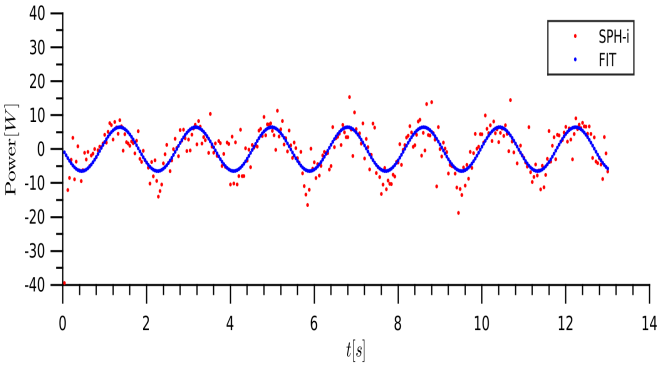

Figure 8.14: Instantaneous power delivered to fluid body Ω

The instantaneous power is a sinusoidal signal with period of $T = 1.8$s and amplitude of about $P_m = 10$W. Furthermore the average power over each half cycle can be computed as

$$\begin{aligned} \mathcal{P}^i &= \frac{2}{T}\int_0^{\frac{T}{2}} P_m \sin\left(\frac{2\pi}{T}t\right) dt \\ &\approx 6.37\text{W} \end{aligned} \tag{8.7}$$

which compared well with the value given in table 8.2

8.3.1 Turbulent production and dissipation of breaking waves

During the wave breaking process, wave power is dissipated due to various mechanisms including (i) turbulent dissipation (ii) viscous dissipation and (iii) boundary dissipation. Figure 8.15 depicts periodic waves undergoing the wave breaking process on a plane slope and the associated specific kinetic energy $\frac{1}{2}||\mathbf{u}_i||^2$ of each fluid particle at time $t = 5.68$s. As the wave approaches the breaking point, fluid velocity $\mathbf{u}_i$ approaches and exceeds the phase velocity $c = \sqrt{gH}$. During this phase, the kinetic energy of the fluid increases, particularly around plunging jet. During this energy transformation process, an increase in kinetic energy is accompanied by an in increase in turbulent kinetic average $\widetilde{k}_h$ given by equation (4.17), as shown in figure 8.16. However, as soon as the turbulent kinetic energy is produced, it is quickly dissipated. Figure (8.17) shows the turbulent dissipation rate, computed from

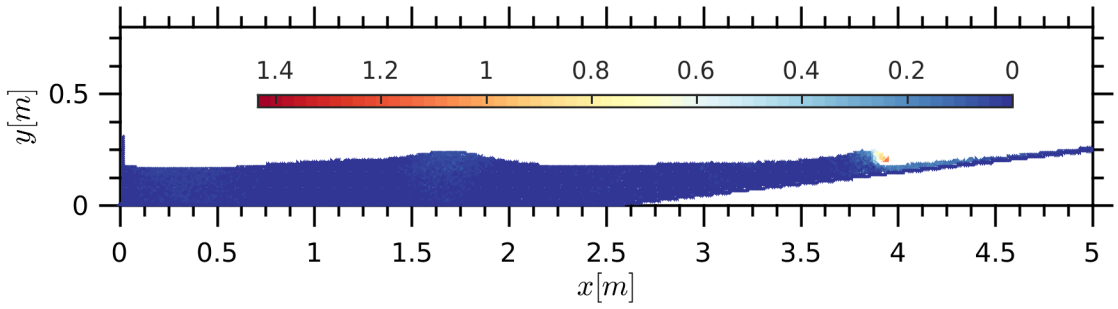

Figure 8.15: Kinetic energy of breaking waves. Color: Specific kinetic energy of each particle $\frac{1}{2}||\mathbf{u}_i||^2 \overset{\mathrm{D}}{\sim} \mathrm{m}^2\mathrm{s}^{-2}$ at time $t = 5.68\mathrm{s}$.

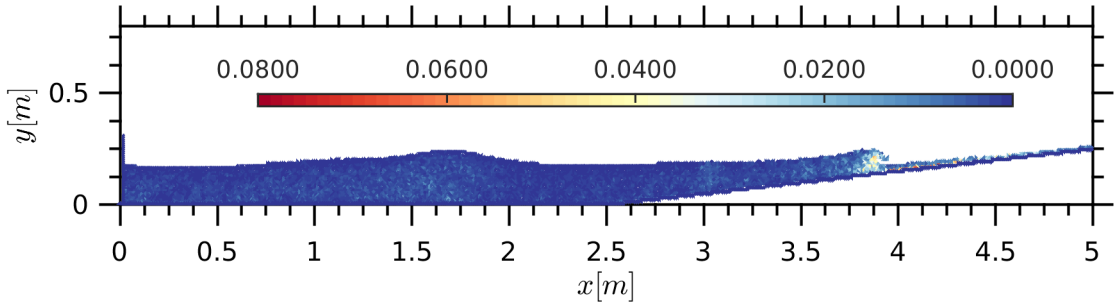

Figure 8.16: Turbulent kinetic energy production of breaking waves. Color: density weighted turbulent kinetic energy $\widetilde{k_h} \overset{\mathrm{D}}{\sim} \mathrm{m}^2\mathrm{s}^{-2}$ at time $t = 5.68\mathrm{s}$.

equation (4.18). As the wave approaches the breaking point, some of the wave energy is transformed into turbulent kinetic energy.

8.3.2 Viscous dissipation of breaking waves

Another important dissipation mechanism for a shallow water breaking wave is viscous dissipation. Figure 8.18 shows the time history of the power due to enstrophy $\mathcal{P}_\omega$ and is associated to the vorticity. Until time $t = 2.8\mathrm{s}$, the power $\mathcal{P}_\omega$ is negligible. At the plunging jet closure $t = 5.8\mathrm{s}$, as the intensity of the vorticity field increases, the power term $\mathcal{P}_\omega$ is no longer negligible. The power term $\mathcal{P}_\omega$ attains its maximum value at the instant the plunging

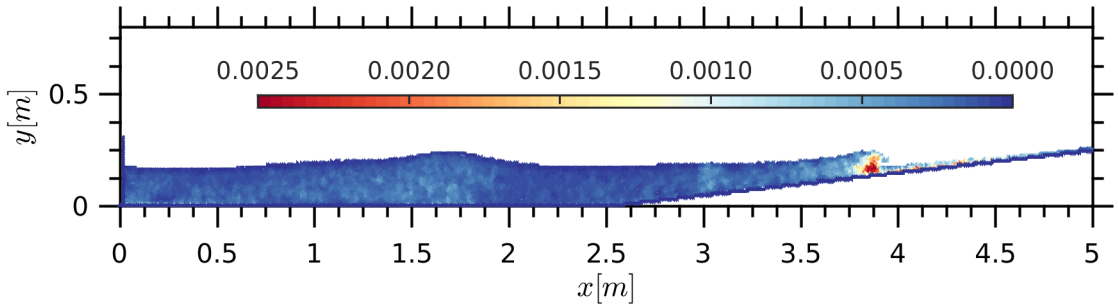

Figure 8.17: Turbulent dissipation dissipation of breaking waves. Color: density weighted local turbulent dissipation rate average $\widetilde{\varepsilon_h} \overset{\mathrm{D}}{\sim} \mathrm{m}^2\mathrm{s}^{-1}$ at time $t = 5.68\mathrm{s}$.

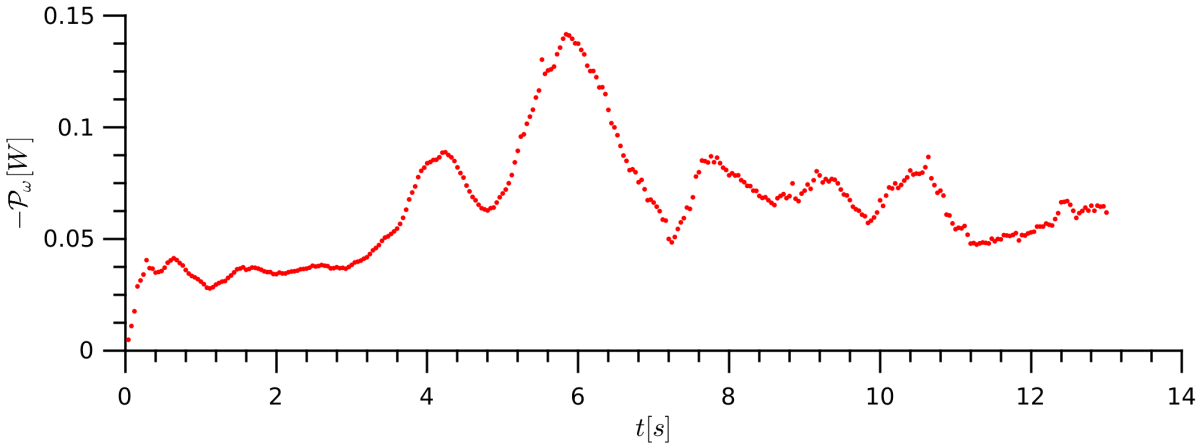

Figure 8.18: Viscous dissipation of shallow breaking waves. Time history of the power $\mathcal{P}_\omega$.

impinges on the free surface, as the cavity collapses. The effect of air entrapment in these cavities would have an effect on the intensity of the power dissipation and thus a two phase model must be considered for higher fidelity of the numerical solution.

8.3.3 Mechanical power delivered to the surf zone

In order to develop suitable engineering device for harnessing energy from breaking waves, it is important to study and quantify the amount of power available. For applications in shallow water, wave energy can be extracted from breaking waves in the surf zone. Figure 8.19a shows a schematic diagram of the numerical wave flume for case 1. A much lower resolution of $dx = dy = 0.01$m was used as the initial particle spacing of fluid particles on a rectangular grid. In the figure, Ω is the fluid domain whereas Ω_b is a control volume in the surf zone. The goal is to compute the instantaneous power $\mathcal{P}(\Omega)$ and $\mathcal{P}(\Omega_b)$ delivered to the fluid body and the control volume, respectively. Figure 8.19b shows a snapshot of the wave prior to breaking. To compute the power transfer to the control volume, a particle identifier ψ was defined: if a fluid particles enters Ω_b then it attains a marker value $\psi = 1$ otherwise it will retain the initial value of $\psi = 0$. In figure 8.19b the fluid particles are colored using the marker ψ.

Figure 8.20 shows a plot of the instantaneous power terms $\mathcal{P}(\Omega)$ and $\mathcal{P}(\Omega_b)$ delivered to the fluid body Ω and the control volume Ω_b, respectively. Since the waves are generated at a wave period of $T = 1.8$s, the power $\mathcal{P}(\Omega)$ will be also be delivered to the fluid body Ω at this same period. Furthermore, power pulses will be registered in the control volume Ω_b whenever a wave is incident on Ω_b. Hence, the control volume power pulse $\mathcal{P}(\Omega_b)$ will also have a period of $T = 1.8$s as can be seen in figure 8.20.

Prior to breaking, dissipative mechanisms do not significantly dissipate wave power. However, during and after the breaking process much of the wave power will be dissipated via several mechanisms. Similarly, the pulses of the mechanical energy are registered is the control volume Ω_b at the same period as the incoming waves $T = 1.8$s. As the waves approach the break point, kinetic energy increases and there is a fast forward current around the plunging jet. Therefore, by placing a suitable wave energy converter (WEC) under a breaking wave, the wave power $\mathcal{P}(\Omega_b)$ can be harnessed into electrical energy; directly in

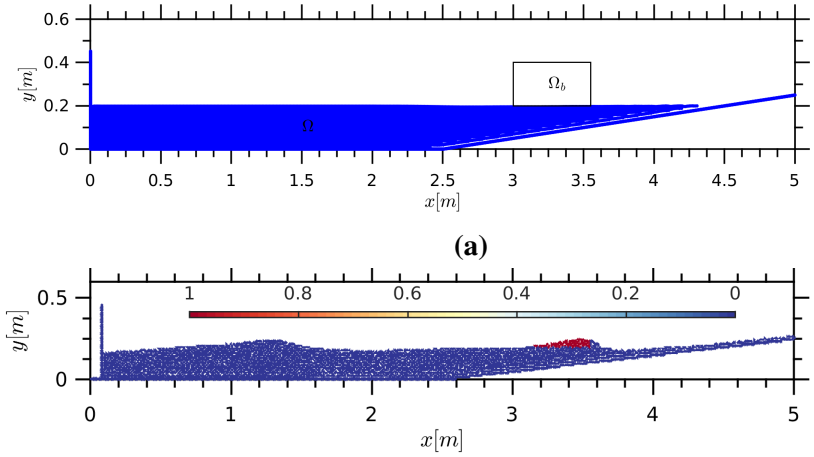

Figure 8.19: (8.19a):Numerical simulation set up for case 1 with fluid domain Ω and surf zone control volume Ω_b. (8.9b):shows the breaking wave at time $t = 4.88$s. Particles are colored using a tag $\psi = 1$ if a fluid particle is in Ω_b and a tag of $\psi = 0$ otherwise.

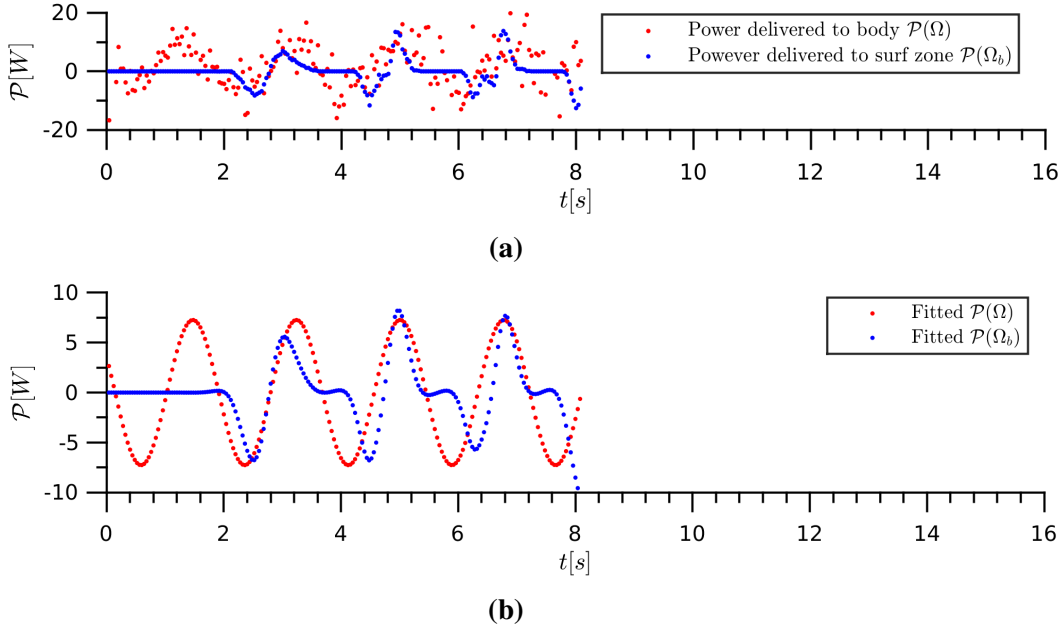

Figure 8.20: Instantaneous power for the breaking wave of case 1 at time $t = 4.88$s where 8.20a is SPH$-i$ instantaneous power and 8.20b is the model fit using Matlab's fitting tools.

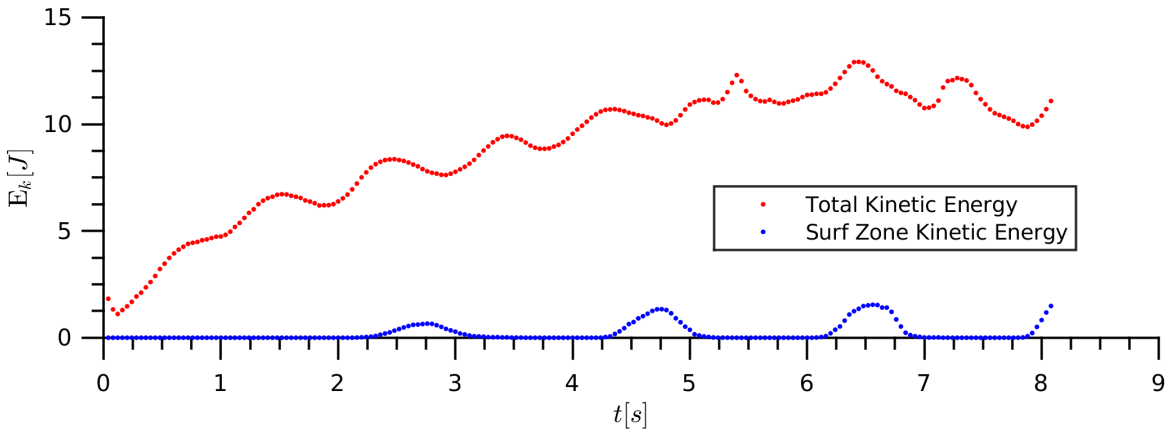

Figure 8.21: Time history of the total kinetic energy $E(\Omega)$ and the kinetic energy $E(\Omega_b)$ of waves in the control volume Ω_b.

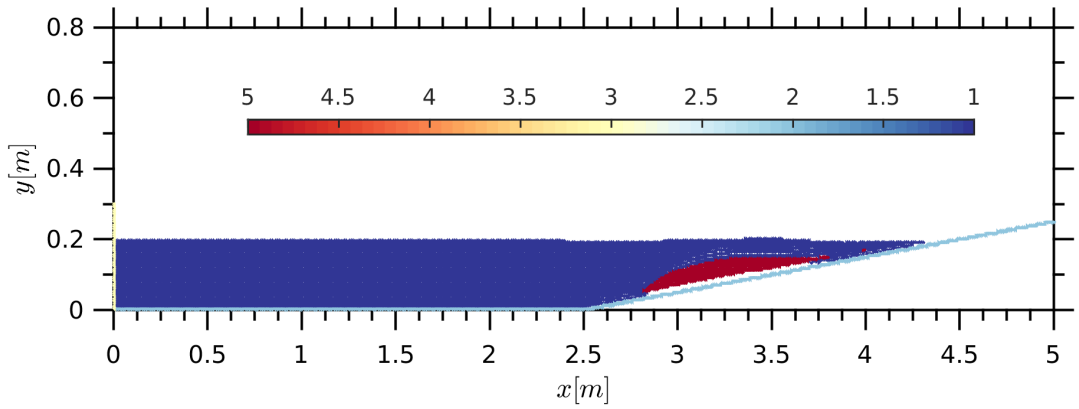

Figure 8.22: Simulation of case 1 with a smooth artificial breaker inserted in the topography. Particle color based on particle type: 1 for fluid particle, 2 for fixed boundary particle, 3 for moving boundary particle, 4 for ghost particle and 5 for solid particles.

the case a WEC based on high efficiency blade technology.

8.3.4 Effect of artificial wave breaker

Figure 8.22 shows the breaking wave test case 1 with a smooth breaker inserted in the topography as shown. The effect of the breaker on the wave breaking process is depicted in figure 8.23. Compared to the case with no breaker in the topography (see figures 8.16, 8.17 and 8.18) the waves feel the effect of the bottom topography at a much earlier time. Thus, the breaker tends to shift the breaking point away from the shore, as would be expected. The size of the breaker obviously matters.

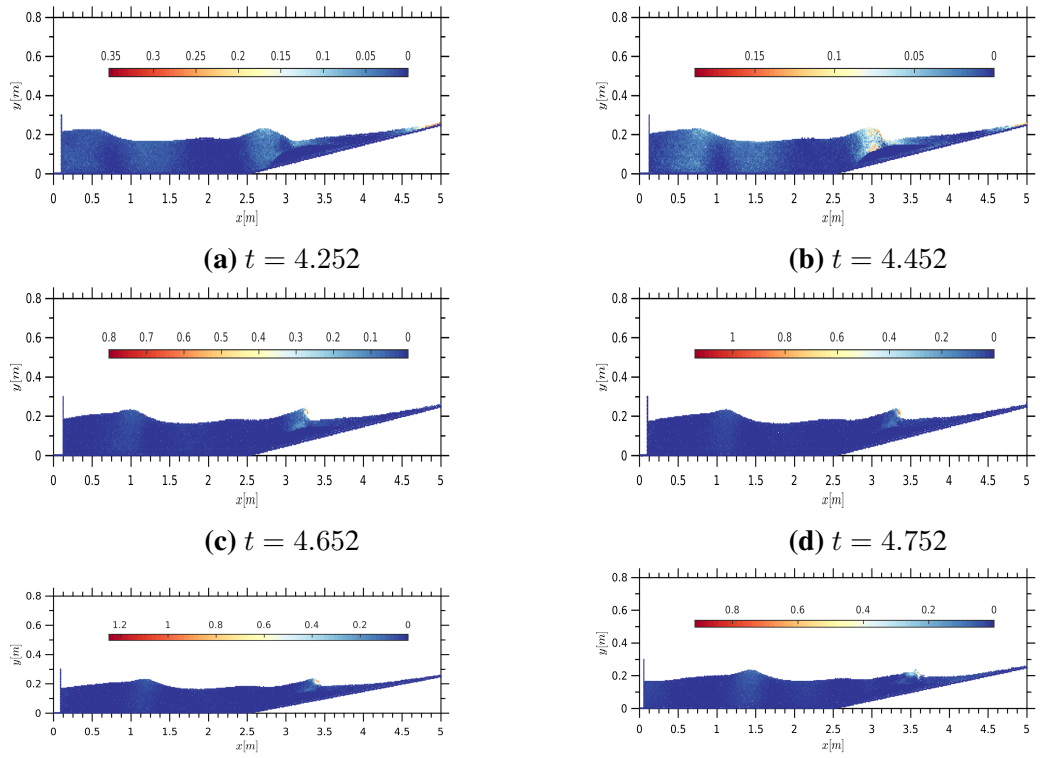

(a) $t = 4.252$ **(b)** $t = 4.452$

(c) $t = 4.652$ **(d)** $t = 4.752$

(e) $t = 4.802$ **(f)** $t = 5.02$

Figure 8.23: Effect of an artificial smooth breaker. Color: kinetic energy density at six time instants for case 1.

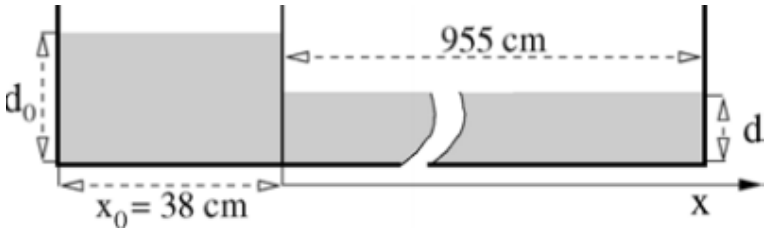

Figure 8.24: Schematic diagram of the experimental setup in [1]

8.4 Mixing process in near-field dam-break flows

The next validation test case to be considered is the dissipation for a shallow water breaking wave due to a dam break process. This free surface flow problem is a standard benchmark test for numerical methods in CFD. It has significant impact on ecosystems downstream and may cause serious environmental damage due to the associated production of (energetic) breaking waves and flooding [1]. The goal of this section is to study the mixing process set up by the collapse of a dam onto a wet bed downstream. The proposed SPH$-i$ model is applied with special attention paid to the mixing process during the onset of a breaking wave.

Janosi [1] et.al. (2004) conducted experiments to study the interaction between two fluid bodies in a dam-break process. The experimental setup comprises a long wave flume with a dam upstream and a wet bed downstream as shown in figure 8.24. They also demonstrated that the flow is essentially two-dimensional and hence the effects of the side walls are negligibly small.

To simulate this problem the above setup would be computationally expensive as the number of fluid particles would be very large. As the maximum recorded time during the actual experiment was 0.6s, it was suggested in [66] to use a shorter downstream channel of 2.5m and this would not have any adverse effects on the simulation results.

The SPH particles were placed on a rectangular grid with initial particle spacing $\Delta r = 0.002$m and initial density $\rho_0 = 1000\text{Kgm}^{-3}$ so that the mass of each fluid particle was $m_0 = 2\text{Kgm}^{-1}$. The average number of near neighbors was fixed at 91; chosen so as to minimize numerical dissipation attributable to filtering/de-filtering processes. Following the discussion in section 3.7, the compact support radius in units of h is then $\xi = \sqrt{N_n/4\pi} = 2.69$. The smoothing length is thus $h = \xi\Delta x = 0.00538$m. The thermal time step dominated the choice of time step and was set at $\Delta t = 2.0 \times 10^{-6}$s to guarantee stability of the numerical solution. The pressure and velocity were all initialized to zero at the start of the simulation.

The gate separating the two water bodies was modeled by a set of boundary particles using the viscously damped boundary force model proposed in chapter 6. The stiffness and damping coefficients were respectively set as $k^s = 0.000589\text{Nm}^{-1}$ and $k^d = 0.002\text{Nsm}^{-1}$ for each particle. The gate was moved at a constant speed to mimic the removal procedure employed in the physical experiment. Furthermore, the fluid bodies were distinguished by a assigning a flag of -1 to the downstream particles and $+1$ for the upstream particles. This enables a clear detection of the mixing interface which manifests as the separation between the flagged particles.

In the first experiment the wet bed height is set at $d = 0.015$m. Figure 8.25 shows that the proposed SPH$-i$ model is able to successfully reproduce the mixing patterns observed

in the breaking wave propagation as the gate was gradually moved up. As the gate starts to gradually move up, due to the higher hydrostatic pressure at the bottom, the upstream fluid particles in the bottom are ejected towards the downstream. On the other hand the downstream fluid is still at rest, hence blocking the approaching upstream fluid. Collision of the moving front with the resting fluid in the ambient layer creates an upthrust in the form of a breaking wave, with free surface breaking occurring in both the forward and reverse directions. The formation and evolution of the plunging jet is captured with reasonable accuracy when compared with snapshots from the experiment. At $t = 0.1962$s the mixing interface is relatively vertical but it slowly tilts towards the downstream direction as the breaking wave propagates downstream. The formation of the plunging jet was first reported by Stansby et.al. [67].

effect of ambient layer: the presence of a shallow ambient layer of fluid in the downstream channel has an important influence on the flow behavior, even for a very small ambient depth d. The next experiment investigates the effect of the wet bed downstream on the flow properties with five ambient depths of $d = 0.005$m, 0.015m, 0.058m and 0.070m. Figure 8.26 shows a qualitative comparison of the experimental and numerical predictions at time $t = 0.3$s.

For very small ambient depths, the potential energy of the wet bed fluid is much less than that of the fluid upstream. Therefore, as the moving front of the upstream fluid collides with ambient fluid upon release of the gate, due to high kinetic energy, a strong upthrust is recorded. This effect leads to the quick formation of a propagating bore for depths $d = 0.005$m, 0.015m. For these three depths, it can be further observed that the plunging wave column consists mainly of the upstream fluid, with a comparatively smaller ambient fluid layer. Furthermore, due to the energetic collision between the moving front and the stationary ambient fluid, the mixing interface tilts towards the downstream direction. In contrast, for larger ambient depths $d = 0.058$m and 0.070m, due to the small difference in potential energy between the upstream and ambient fluid downstream, the moving front collides with the ambient fluid with low kinetic energy. For this case, it takes longer for the waves to fully develop and the free surface breaking phenomena may not occur. Due to the less energetic collision, the mixing interface for larger depths largely remains vertical as the waveform gains height. Clearly, the SPH$-i$ model shows a satisfactory agreement with the experimental results at time $t = 0.3$s.

As the generated turbulent bore propagates further downstream, breaking phenomena occurs, depending on the wet bed depth. This phenomena is captured in figure 8.27 at $t = 0.6$s. Again, for low ambient depths $d = 0.005$m, 0.015m the mixing keeps tilting towards the downstream direction whereas for the larger depths $d = 0.058$m and 0.070m the mixing interface remains largely vertical as in the early mixing stages. It can also be observed that the two fluid bodies are quite well mixed by the time.

Besides experimental studies by Janosi et.al. [1], the mixing process in dam break flows with upstream and downstream fluid bodies has recently been studied using various corrected versions of SPH and MPS models [68][66].

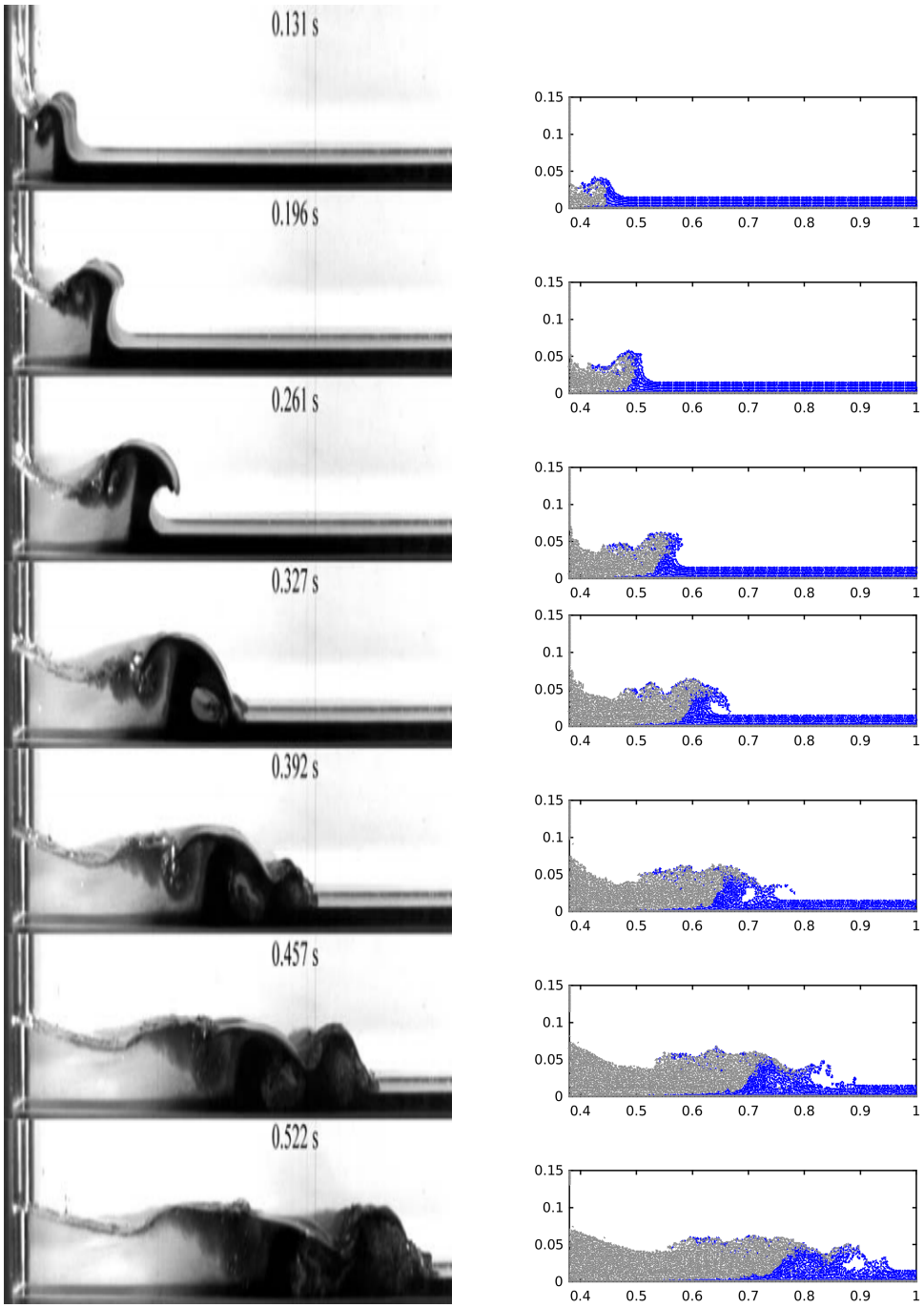

Figure 8.25: Comparison of laboratory photographs(left, Janosi et.al. [1]) with simulated mixing patterns obtained using the proposed SPH$-i$ model at times $t = 0.1962\text{s}, 0.2616\text{s}, 0.3270\text{s}$ and 0.3920s.

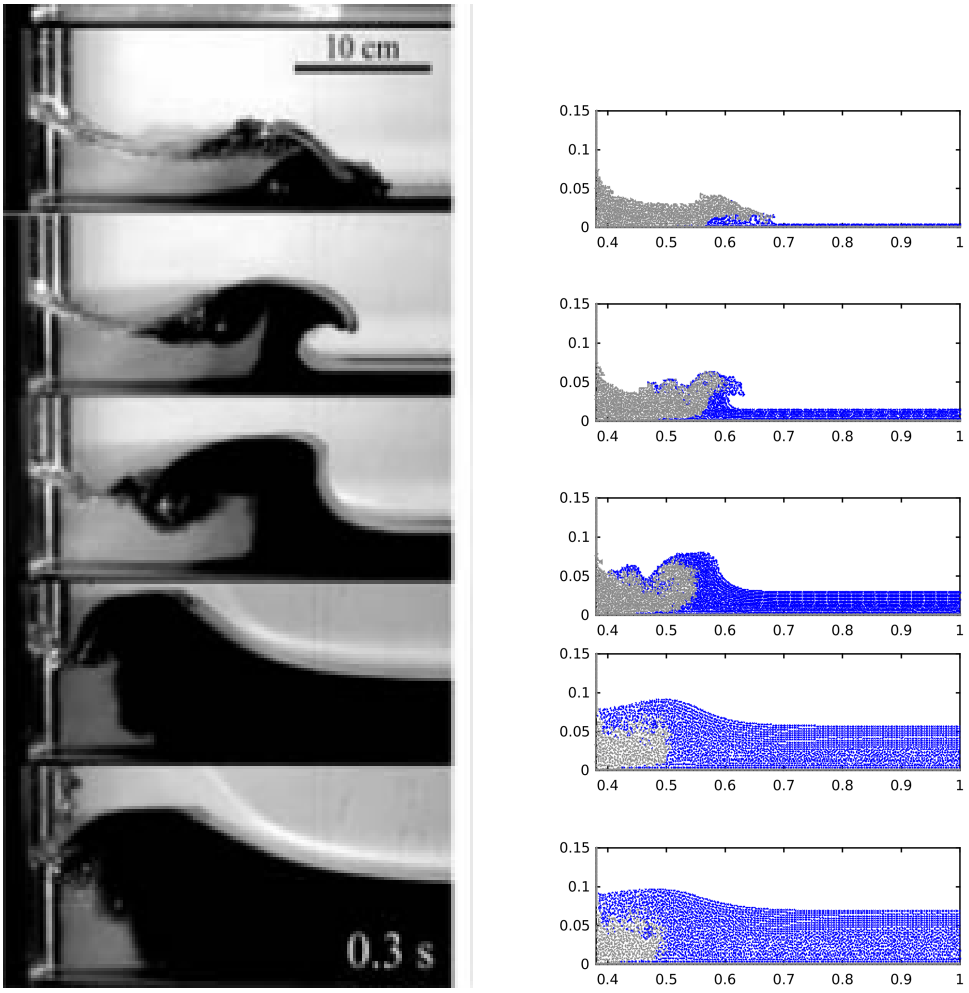

Figure 8.26: Mixing patterns generated by the release of a dam-break front into a wet bed of increasing depth d (from top to bottom) 0.005m, 0.015m, 0.058m and 0.070m at time $t = 0.3$s(left panel, Janosi et.al. [1]) with simulations performed using the proposed SPH$-i$ model (right panel).

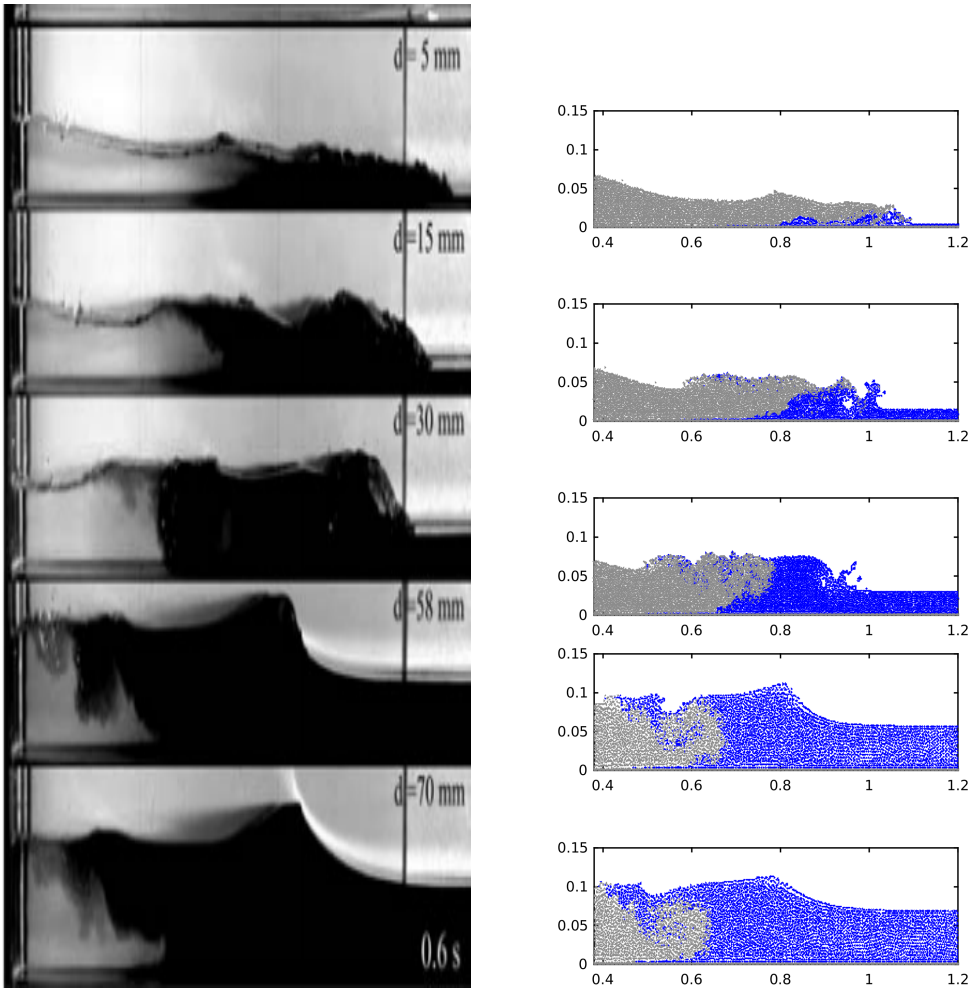

Figure 8.27: Mixing patterns generated by the release of a dam-break front into a wet bed of increasing depth d (from top to bottom) 0.005m, 0.015m, 0.058m and 0.070m at time $t = 0.6$s(left panel, Janosi et.al. [1]) with simulations performed using the proposed SPH$-i$ model (right panel).

Conclusion

A smoothed particle hydrodynamics SPH$-i$ solver that implicitly models turbulence has been developed. The major distinction between the proposed model and standard SPH models is that while standard SPH evolves the smoothed field $\{\langle\rho_h\rangle, \langle p_h\rangle, \langle\rho_h\rangle\widetilde{\mathbf{u}}_h\}$ the SPH$-i$ model evolves the underlying disordered field $\{\rho, p, \rho\mathbf{u}\}$. It is due to this fundamental difference that standard SPH would require explicit turbulence modeling. Moreover, the SPH$-i$ is a high order model whereas standard SPH models can be formally defined as a zeroth order deconvolution models. This model further introduces an equation for pressure that has inherent smoothing terms that smooth out spurious numerical noise in the pressure field. Furthermore, this way of computing the pressure guaranteed long term stability as is evidenced by the stable solution obtained for the hydrostatic problem.

The proposed SPH$-i$ uses two filters; a convolution filter and a deconvolution filter. A rigorous procedure for constructing these filters in 2D has been presented and extension of the approach to 3D is a trivial exercise. Using the filters introduces two competing effects; numerical dissipation and numerical instability. If the order of the deconvolution filter is increased, numerical dissipation decreases and thus higher accuracy is attained. On the other hand with decreased numerical dissipation, numerical instability is enhanced. One can never have both numerical stability and zero numerical dissipation; in particular, even though exact deconvolution introduces zero numerical dissipation, it is numerically unstable. Therefore, this demands a compromise such that some amount of numerical dissipation is allowed so as to have low numerical instability. It is this numerical dissipation that smoothes out numerical instabilities introduced by filtering and de-filtering processes. To ascertain the suitable range of order of the deconvolution filter, quantifying both numerical dissipation and instability is critical. While numerical dissipation can be estimated from Kolmogorov energy spectrum, it is difficult to quantify numerical instability. However, a crude approximation is made under the assumption that the numerical error is caused by spectral truncation. A much reliable criteria for quantifying numerical instability must therefore be developed.

In this work a clear procedure for deriving the filtered equations consistent with explicit LES has been presented. This was achieved by introducing an integral transform called FIT and defining a proper rule for moving the fluid particles. An integral representation of the SGS tensor is obtained and the ADM presented in this thesis can be further applied to explicitly model turbulence. However, by de-filtering the filtered equations using the inverse transform called DIT, the SGS tensor is de-filtered and thus resulting in a model in which turbulence effects are implicitly captured.

While the SPH$-i$ model generated simulation results that are generally in agreement with experimental data, the influence of air in free surface flows should be considered. In the case of breaking waves, it possible that a significant portion of the wave energy is transfered to the

air phase. If the energy transfered to the air is significant enough, energy harvesting devices can be designed specifically for this purpose. Furthermore, a reliable way of quantifying energy error due to numerical instability is crucial in estimating the optimal range of values for the deconvolution filter since an exact deconvolution filter is practically useless.

To avoid numerical instabilities that may arise due to the use of nonlinear boundary force models such as the Lennard-Jones potential, a linear model has been adopted in this thesis. However, two coefficients; the stiffness and damping coefficients must be calibrated. Proper choice of these coefficients was determined by trial and error by noting that the boundary forces must not cause any significant damping of the system energy.

A discussion on the power delivered to a fluid body has been discussed. For flows with large deformation of the free surface, dissipation of mechanical energy was observed. Some of the loss mechanisms include turbulent dissipation and viscous dissipation. The viscous power dissipation term $\mathcal{P}_\omega$ was found to be non-negligible during the wave breaking process.

The SPH$-i$ model was applied to a number of free surface flow benchmark problems. Long-time stable hydrostatic pressure profiles where obtained for the hydrostatic tank problem. Two types of dam-break problems were investigated; First, the dam break on a dry bed problem agreed comparatively well with experimental data. Second, the dam break on a wet bed was also investigated. The mixing process involved in both early and later stages showed that the SPH$-i$ model is capable of simulating mixing dynamics with satisfactory accuracy for both shallow and deep wet beds.

For future work, the use of rational kernels must be investigated as they tend to be more stable when used in the SPH$-i$ model. Furthermore, a refined model for quantifying numerical instability must be sought. As it is well known, a free surface model does not accurately capture all the details associated with flows undergoing deformation and therefore, two phase models must be developed. It is also worth investigating the effect of placing waveguides onshore with respect to enhancement of the wave energy density. For stability reasons associated with two phase flows and the need to have a simpler SPH$-i$ model, a different definition a the volume element might be preferable compared to the one adopted in this thesis. Finally and most importantly, qualitative tests for turbulence and accuracy of the SPH-i model compared with standard SPH must be carried. This would be very important in establishing SPH-i as a high order model that has the capability to simulate turbulent flows with high fidelity.

Appendix A

Fourier transforms

A.1 Fourier Transform of radially symmetric function

The Fourier transform of the convolution and deconvolution filters forms part of the analysis in this work. As these filters are radially symmetric, it is important to define the Fourier transform in polar coordinates.

$$\int_{\mathbb{R}^2} e^{-2\pi i \boldsymbol{\xi}\cdot\mathbf{r}} f(\mathbf{r}) d^2\mathbf{r} = \int_{-\infty}^{\infty}\int_{-\infty}^{\infty} e^{-i2\pi(\xi_1 x_1 + \xi_2 x_2)} f(x_1, x_2) dx_1 dx_2 \tag{A.1}$$

By identifying $(x_1, x_2) \to (r, \theta)$ to be varying in the plane (x_1, x_2)-plane and put $(\xi_1, \xi_2) \to (\rho, \phi)$ (fixed in the integral) then the Fourier transform becomes

$$\int_{\mathbb{R}^2} e^{-2\pi i \boldsymbol{\xi}\cdot\mathbf{r}} f(\mathbf{r}) d^2\mathbf{r} = \int_{0}^{\infty}\int_{0}^{2\pi} e^{-i2\pi r\rho\cos(\theta-\phi)} f(r) r dr d\theta \tag{A.2}$$

Due to periodicity in θ, we have the following property

$$\int_{0}^{2\pi} e^{-i2\pi r\rho\cos(\theta-\phi)} d\theta = \int_{0}^{2\pi} e^{-i2\pi r\rho\cos\theta} d\theta \tag{A.3}$$

As is always the case with problems involving circular symmetry, we introduce Bessel functions

$$J_0(2\pi r\rho) = \frac{1}{2\pi}\int_{0}^{2\pi} e^{-i2\pi r\rho\cos\theta} d\theta \tag{A.4}$$

where J_0 is the zeroth order Bessel function. Therefore, the Fourier transform of $f(r)$ is

$$\mathcal{F}\{f(r)\} = 2\pi\int_{0}^{\infty} J_0(2\pi r\rho) f(r) r dr \tag{A.5}$$

which turns out be radially symmetric as well and is sometimes called the Hankel transform of $f(r)$.

Appendix B

Appendices and Supplementary Data

B.1 Convolution Operator for Approximate Gaussian Filter

In particle methods it is desirable that the convolution filter is compact for computational efficiency. It is due to this that the Gaussian filter, despite having high accuracy and stability, is not practically used. To this end, we propose a class of filters that are approximate Gaussian filters. With brevity, we present the result below.

Proposition B.1.1 (Approximate Gaussian Filter)**.** *Consider $C_c^\infty(\mathbb{R}^\kappa)$ (a space of compactly supported continuous functions) dense in $L^2(\mathbb{R}^\kappa)$. For a two-parameter function $G_{h,p} \in L^2(\mathbb{R}^\kappa)$ and $\varepsilon > 0$, there is a two-parameter function $w_{h,p} \in C_c^\infty(\mathbb{R}^\kappa)$ such that*

$$\left(\int_\alpha^\beta |G_{h,p}(\mathbf{r}) - w_{h,p}(\mathbf{r})|^2 d^\nu \mathbf{r} \right)^{\frac{1}{2}} \leq \varepsilon \tag{B.1}$$

The compactly supported approximate Gaussian problem can be stated as: Given a smooth and continuous function $G_{h,p} \in L^2(\mathbb{R}^\kappa)$,

$$G_{h,p} = \alpha_p h^{-\nu} \exp\left(-\pi \sqrt[\nu]{\alpha_p^2} \frac{||\mathbf{r} - \mathbf{r}'||^2}{h^2} \right) \tag{B.2}$$

how can we construct a function $w_{h,p}$ to be continuous and compactly supported such that it is a good approximant of the Gaussian function $G_{h,p}$ so that (B.1) is satisfied. To this end, without delving into detailed derivations, we propose the following piecewise continuous function

$$w_{h,p} = \begin{cases} \alpha_p h^{-\nu} \left(\frac{1 - \frac{1}{4h^2}||\mathbf{r}-\mathbf{r}'||^2}{1 + \frac{1}{4h^2}||\mathbf{r}-\mathbf{r}'||^2} \right)^p & ||\mathbf{r} - \mathbf{r}'|| \leq 2h \\ 0 & \text{otherwise} \end{cases} \tag{B.3}$$

where the compact space is $V_h : [0, 2h] \times [0, 2h] \times [0, 2h]$. Not all values of $p \in \mathbb{N}$ are admissible. Indeed if we inspect the Fourier transform of $w_{h,p}$ for $p = 2m$, $m = 1, 2, 3, ...$ it is indefinite i.e. we find that $\mathcal{F}\{w_{h,p}\}(hk) > 0$ for some wavenumbers k and $\mathcal{F}\{w_{h,p}(hk)\} < 0$ for some k. On the other hand for $p = 2m+1$, $m = 1, 2, 3, ...$ the Fourier transform of $w_{h,p}$ is positive definite i.e. $\mathcal{F}\{w_{h,p}\}(hk) > 0$ for all wavenumbers k. Since $w_{h,p}$ is a Gaussian

approximant and we know the Gaussian filter has a positive definite Fourier transform, we conclude that the admissible class of Gaussian approximants are those with odd powers of p, i.e. $p = 2m + 1$, $m = 1, 2, 3, ...$; these are the stable and consistent Gaussian approximants, a property that is fundamental to the stability of numerical simulations.

$$w_{h,2p+1} = \begin{cases} \alpha_{2p+1} h^{-\nu} \left(\frac{1 - \frac{1}{4h^2}||\mathbf{r}-\mathbf{r}'||^2}{1 + \frac{1}{4h^2}||\mathbf{r}-\mathbf{r}'||^2} \right)^{2p+1} & ||\mathbf{r} - \mathbf{r}'|| \leq 2h \\ 0 & \text{otherwise} \end{cases} \tag{B.4}$$

It is easy to show that the following $w_{h,p}$ is a good Gaussian approximant such that

$$w_{h,p} \simeq G_{h,p}, \quad \frac{1}{2\sigma_p^2} := 4\pi\alpha_p = p + \delta p \tag{B.5}$$

With this compactly supported approximate Gaussian filter, we then have the associated convolution operator similar to (3.68) and is given by

$$\langle w_p - G_p, \hat{T} \rangle \simeq 0 \Leftrightarrow \langle w_p, \hat{T} \rangle \simeq \langle G_p, \hat{T} \rangle = \exp\left(\frac{1}{4\pi\alpha_p} h^2 \nabla^2 \right) \tag{B.6}$$

In series form, approximate convolution and deconvolution operators

$$\langle w_p, \hat{T} \rangle \simeq e^{+\hat{1}\frac{h^2}{4\pi\alpha_p}\nabla^2} = \hat{1} + \sum_{n=1}^{\infty} \frac{h^{2n}\hat{1}}{(4\pi\alpha_p)^n \, n!} \nabla^{2n} \tag{B.7}$$

$$\text{Inv}[\langle w_p, \hat{T} \rangle] \simeq e^{-\hat{1}\frac{h^2}{4\pi\alpha_p}\nabla^2} = \hat{1} + \sum_{n=1}^{\infty} (-1)^n \frac{h^{2n}\hat{1}}{(4\pi\alpha_p)^n \, n!} \nabla^{2n} \tag{B.8}$$

where $\hat{1}$ is the identity operator in infinite dimensional space. Both operators (B.7) and (B.8) are inverse to each other and contain two adjustable parameters: h and p. These two parameters can be exploited to accelerate convergence of the series.

The goal is to determine the deconvolution filter associated with the approximate Gaussian filter.

$$\begin{aligned} \varphi_{h,p}(\mathbf{r}'' - \mathbf{r}) &= \widetilde{l}_d^2(\mathbf{r}, h) w_{h,p}(\mathbf{r}'' - \mathbf{r}) \\ &= \sum_{k=0}^{\infty} (-1)^k \frac{h^{2k}}{(2\pi\alpha_p)^k \, k!} \nabla^{2k} w_{h,p} \end{aligned} \tag{B.9}$$

There is a fundamental limitation, however, that we/computers can only deal with finite collection of numbers. In practice, the infinite sum in (B.9) is replaced by a finite sum. Therefore the method is called Approximate Deconvolution Method (ADM). For a 2D problem, we have

$$\varphi_{h,p,n}(\mathbf{r} - \mathbf{r}') = \sum_{k=0}^{n} (-1)^k \frac{h^{2k}}{(2\pi\alpha_p)^k \, k!} \nabla^{2k} w_{h,p}(\mathbf{r} - \mathbf{r}') \tag{B.10}$$

which forms a sequence in n containing two adjustable parameters h and p. Furthermore, since $\pi \sqrt[\nu]{\alpha_p^2} := p + \delta p$ and the filter width is defined through $2\sigma_p^2 = 1/(p + \delta p)$, it means that

if $p \to \infty$ then $\alpha_p \to \infty$ and $\sigma_p \to 0$. In this case, both the convolution and deconvolution filters approach Dirac's delta function. Moreover, the filter cut-off length $h < 1$ as it is chosen as the initial particle spacing (or equivalently mesh size). More specifically, since $h < 1$ and $\alpha_p > 1$, as $k \to \infty$, $h^{2k} \to 0$ and $\alpha_p^{-k} \to 0$ fast. Therefore the series (B.10) is convergent and higher order terms can be neglected. Figure B.1 shows a plot of the two filters for $p = 6$ and $n = 2$.

; ; ;

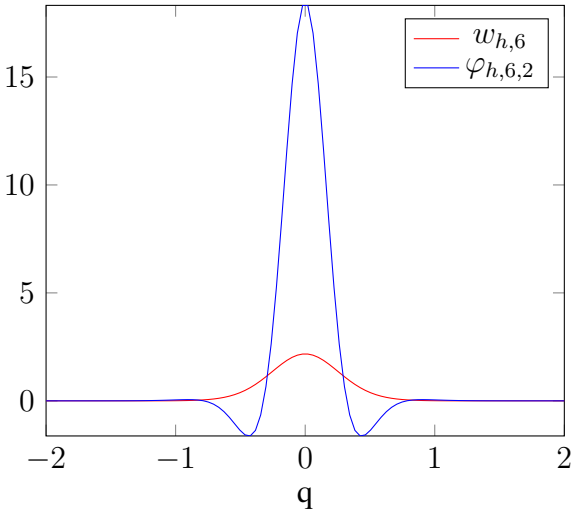

Figure B.1: A plot of the convolution filter $w_{h,p}$ for p=6 (red) and the corresponding deconvolution filter $\varphi_{h,p,n}$ (blue) obtained by truncating the infinite sum at $n = 2$. The filter cut-off length h has been set to unity.

Bibliography

[1] I. M. Jánosi, D. Jan, K. G. Szabó, and T. Tél, Experiments in Fluids **37**, 219–229 (2004).

[2] D. Henry, Nonlinear Mathematical Physics **15**, 87–95 (2008).

[3] L. H. Holthuijsen. *Linear wave theory (coastal waters)*. In *Waves in Oceanic and Coastal Waters*, pages 197–243. Cambridge University Press, (2007). Cambridge Books Online.

[4] W. Y. Gotoh H., Okayasu A. *Computational Wave Dynamics*. In Y. A., editor, *Computational Fluid Dynamics*, pages 137–180. World Scientific, (2013).

[5] A. V. Babanin, *Breaking and dissipation of ocean surface waves / Alexander Babanin*, Cambridge University Press Cambridge (2011).

[6] Z. Chen, Z. Zong, M. B. Liu, and H. T. Li, International Journal for Numerical Methods in Fluids **73**, 813–829.

[7] A. Colagrossi and M. Landrini, Journal of Computational Physics **191**, 448 – 475 (2003).

[8] M. Liu, W. Xie, and G. Liu, Applied Mathematical Modelling **29**, 1252 – 1270 (2005).

[9] M. Liu and G. Liu, Applied Numerical Mathematics **56**, 19 – 36 (2006).

[10] G. A. Dilts, International Journal for Numerical Methods in Engineering **48**, 1503–1524.

[11] G. A. Dilts, International Journal for Numerical Methods in Engineering **44**, 1115–1155.

[12] M. Antuono, A. Colagrossi, S. Marrone, and D. Molteni, Computer Physics Communications **181**, 532 – 549 (2010).

[13] D. Molteni and A. Colagrossi, Computer Physics Communications **180**, 861 – 872 (2009).

[14] J. R. Clausen, Phys. Rev. E **87**, 013309 (2013).

[15] A. J. Chorin, Journal of Computational Physics **2**, 12 – 26 (1967).

[16] J. J. Monaghan, Annual Rev. of Astron and Astrophys **30**, 543–574 (1992).

[17] S. Shao and E. Y. Lo, Advances in Water Resources **26**, 787 – 800 (2003).

[18] M. B. Liu and G. R. Liu, *Particle Methods for Multi-Scale and Multi-Physics*, World Scientific Publishing Co (2016).

[19] P. Sun, A. Colagrossi, S. Marrone, and A. Zhang, Computer Methods in Applied Mechanics and Engineering **315**, 25 – 49 (2017).

[20] J. Clausen. *Developing highly scalable fluid solvers for enabling multiphysics simulation.* Technical report, Sandia National Laboratories (SNL-NM), Albuquerque, NM (United States), (2013).

[21] T. A. Zang, R. B. Dahlburg, and J. P. Dahlburg, Physics of Fluids A: Fluid Dynamics **4**, 127–140 (1992).

[22] J. Monaghan, Journal of Computational Physics **110**, 399 – 406 (1994).

[23] M. Müller, D. Charypar, and M. Gross. *Particle-based Fluid Simulation for Interactive Applications*. In *Proceedings of the 2003 ACM SIGGRAPH/Eurographics Symposium on Computer Animation*, SCA '03, pages 154–159, Aire-la-Ville, Switzerland, Switzerland, (2003). Eurographics Association.

[24] T. B. Anderson and R. Jackson, Industrial & Engineering Chemistry Fundamentals **6**, 527–539 (1967).

[25] N. C. Admal and E. B. Tadmor, Journal of Elasticity **100**, 63–143 (2010).

[26] M. Germano, The Physics of Fluids **29**, 1755–1757 (1986).

[27] C. Konstantopoulos, L. Mittag, G. Sandri, and R. Beland, Journal of Applied Physics **68**, 1415–1420 (1990).

[28] M. Elias and R. J. A., Canadian Journal of Statistics **20**, 9–21.

[29] D. J. Price, Journal of Computational Physics **231**, 759 – 794 (2012).

[30] J. J. Monaghan, Reports on Progress in Physics **68**, 1703 (2005).

[31] J. J. Monaghan and J. C. Lattanzio, aap **149**, 135–143 (1985).

[32] H. Wendland, Advances in Computational Mathematics **4**, 389–396 (1995).

[33] W. Dehnen and H. Aly, Monthly Notices of the Royal Astronomical Society **425**, 1068–1082.

[34] L. Fang, J. C. Marongiu, J. Leduc, A. Amicarelli, and J. Caro, Chinese Journal of Aeronautics **30**, 1 – 14 (2017).

[35] O. San, A. E. Staples, Z. Wang, and T. Iliescu, Ocean Modelling **40**, 120 – 132 (2011).

[36] C. Konstantopoulos, L. Mittag, G. Sandri, and R. Beland, Journal of Applied Physics **68**, 1415–1420 (1990).

[37] P. Domingo and L. Vervisch, Proceedings of the Combustion Institute **35**, 1349 – 1357 (2015).

[38] M. Germano, Physics of Fluids **21**, 045107 (2009).

[39] W. Ulmer, Inverse Problems **26**, 085002 (2010).

[40] B. J. Geurts, Physics of Fluids **9**, 3585–3587 (1997).

[41] Q. Wang and M. Ihme, Combustion and Flame **176**, 125 – 142 (2017).

[42] L. C. Berselli and R. Lewandowski, Annales de l'Institut Henri Poincare (C) Non Linear Analysis **29**, 171 – 198 (2012).

[43] S. Li and W. K. Liu, *Meshfree Particle Methods*, Springer Publishing Company, Incorporated (2007).

[44] S. Marrone. *Enhanced SPH modeling of free-surface flows with large deformations*. PhD thesis, Department of Mechanical and Aerospace Engineering, Sapienza University of Rome, Rome, Italy, (2011). An optional note.

[45] N. J. Quinlan, M. Basa, and M. Lastiwka, International Journal for Numerical Methods in Engineering **66**, 2064–2085 (2006).

[46] J. J. Monaghan, Monthly Notices of the Royal Astronomical Society **335**, 843–852 (2002).

[47] J. Monaghan, European Journal of Mechanics - B/Fluids **30**, 360 – 370 (2011).

[48] X. Hu and N. Adams, Procedia IUTAM **18**, 66 – 75 (2015).

[49] J. Fang, A. Parriaux, M. Rentschler, and C. Ancey, Applied Numerical Mathematics **59**, 251 – 271 (2009).

[50] J. Monaghan, Journal of Computational Physics **82**, 1 – 15 (1989).

[51] H. Gotoh, T. Shibahara, and T. Sakai, Advanced Methods for Computational Fluid Dynamics **9-4**, 339–347 (2001).

[52] J. R. Shao, H. Q. Li, G. R. Liu, and M. B. Liu, Comput. Struct. **100-101**, 18–26 (2012).

[53] J. Monaghan and J. Kajtar, Computer Physics Communications **180**, 1811 – 1820 (2009).

[54] L. Landau and E. Lifshitz, *Mechanics*, Elsevier Science (1982).

[55] G. Oger, M. Doring, B. Alessandrini, and P. Ferrant, Journal of Computational Physics **225**, 1472 – 1492 (2007).

[56] T.-H. Lee, Z. Zhou, and Y. Cao, Journal of Fluids Engineering **124**, 215–226 (2002).

[57] A. Colagrossi, B. Bouscasse, and S. Marrone, Phys. Rev. E **92**, 053003 (2015).

[58] *A nonlinear 3D approach to simulate green water dynamics on deck*, (1999).

[59] E. Y. Lo and S. Shao, Applied Ocean Research **24**, 275 – 286 (2002).

[60] R. Dalrymple and B. Rogers, Coastal Engineering **53**, 141 – 147 (2006).

[61] B. Rogers and R. Dalrymple. *SPH Modeling of Breaking Waves*, pages 415–427. (2005).

[62] V. D. and I. R., International Journal for Numerical Methods in Fluids **53**, 277–304.

[63] S. Songdong and J. Changming, International Journal for Numerical Methods in Fluids **51**, 913–936.

[64] A. Mahmoudi, H. Hakimzadeh, M. J. Ketabdari, A. Etemadshahidi, N. Cartwright, and H. a. Abyn, International Journal of Maritime Technology **5** (2016).

[65] J. Fenton and W. McKee, Coastal Engineering **14**, 499 – 513 (1990).

[66] W. Jian, D. Liang, S. Shao, R. Chen, and X. Liu, Natural Hazards **78**, 531–553 (2015).

[67] P. K. STANSBY, A. CHEGINI, and T. C. D. BARNES, Journal of Fluid Mechanics **374**, 407–424 (1998).

[68] A. Khayyer and H. Gotoh, Journal of Hydraulic Research **48**, 238–249 (2010).